Control and Analysis of Air, Water, and Thermal Systems for a Polymer Electrolyte Membrane Fuel Cell

by

Jong-Woo Ahn

A dissertation submitted to the Graduate Faculty of
Auburn University
in partial fulfillment of the
requirements for the Degree of
Doctor of Philosophy

Auburn, Alabama
August 6, 2011

Keywords: PEM fuel cell, air, water, thermal management.

Approved by

Song-Yul Choe, Chair, Associate Professor of Mechanical Engineering
David Beale, Professor of Mechanical Engineering
Jay Khodadadi, Alumni Professor of Mechanical Engineering

Abstract

The polymer electrolyte membrane (PEM) fuel cell is a power source that can potentially replace the internal combustion engine in vehicles of the future. When hydrogen stored in a tank and oxygen from the air chemically react in a PEM fuel cell, electricity is generated and water and heat are produced as by-products. The management of fuel, water, and heat are crucial issues in order to ensure reliable operation and to maintain high efficiency with continuously changing loads.

During the operation of a fuel cell, oxygen from the air is supplied to the cathode side of the fuel cell. Insufficient oxygen supply during dynamic loads causes oxygen starvation, which forces protons transported through the membrane to reduce the amount of hydrogen on the cathode catalysts. Reduced hydrogen could chemically generate heat on the platinum particles and result in local hot spots in the membrane electrode assembly (MEA), which could lead to failure of the fuel cells. Conversely, an excessive oxygen supply increases the parasitic power dissipated by an air supplier such as a blower, which leads to low efficiency of the overall system. Therefore, an optimal supply of oxygen is one of challenging issues addressed by researchers.

When a chemical reaction takes places, water is produced in the cathode catalyst. A fraction of the water moves from the catalyst though the membrane and to the anode. In contrast, protons crossing the membrane take up water from the anode to the cathode. The water content in

membranes directly affects proton conductivity. Insufficient water causes dehydration that decreases proton conductivity and increases voltage loss, which leads to a reduction in output power. However, the water produced by chemical reactions causes flooding in gas flow channels, gas diffusion layers, and catalyst layers, which blocks oxygen transport to the catalysts and reduces the catalyst activation areas. As a result, the degradation of components is accelerated. Therefore, excessive water in the cell should be removed to prevent flooding, and at the same time the membrane should be kept fully humidified.

When operating, heat produced in the stack continuously changes as the load current varies. Consequently, the temperature inside the cells also varies. Variation of the temperature directly affects rates of chemical reaction and the phase change of water, and finally the water transport. Improper rejection of the heat might produce local hotspots and degrade the thin layers of the cell. Low temperatures decrease the rate of the chemical reaction and reduce efficiency. Conversely, elevated temperatures increase the reaction rate, ease the removal of water, and increase the mobility of water vapor in the membrane, which alleviates over-potential losses. In addition, parasitic power necessary for operating a coolant pump should be reduced in conjunction with the heat rejection strategy, which contributes to an increase in system efficiency. Therefore, thermal management is another challenging issue for reliable and efficient operation.

The research conducted for my doctoral program focused on the development of fuel cell models for air, water, and thermal systems, and on the related components. The control-oriented models were used in the design of control strategies and in the analysis of integrated systems. The air and water supply systems consist of a blower, a humidifier, and inlet and outlet manifolds. The thermal management system is composed of a bypass valve, a liquid-to-liquid

heat exchanger, a radiator with a fan, reservoirs, and pumps. The objectives of the proposed control strategies are to prevent oxygen starvation, maintain a proper water balance in the cells, reject excessive heat in the stack, and at the same time the parasitic powers are minimized. Considering the aforementioned system configurations and objectives, state feedbacks with integral controls were designed and optimized. The entire system was simulated and analyzed, and the resulting static and dynamic behavior obtained by experiments is described.

Acknowledgements

I would like to thank Dr. Song-Yul Choe for his constructive advice and considerable support during this research. Thanks are given to my parents, Hong-Kyu Ahn and Ok-Jae You, for their support. In particular, I would like to thank Jinglin He for his advice and discussion, and other faculty and graduate students who have supported this research.

Table of Contents

List of Tables

List of Figures

Nomenclature

Alphabet:		*Units*
a	Water activity	
A	Area	cm^2
b	Membrane expansion coefficient	
C	Mass concentration	$kg\ m^{-3}$
Cp	Specific heat	$W\ m^{-2}\ {}^{o}C^{-1}$
D	Diffusion coefficient	$m^2\ s^{-1}$
F	Faraday number	
FM	Flow meter	
i or I	Current density	$A\ cm^{-2}$
HS	Humidity sensor	
h	Heat transfer coefficient	$kW\ m^{-2}\ {}^{o}C^{-1}$
J	Rotational inertia	$kg\ m^2$
K	Permeability	m^2
m	Mass	kg
M	Molar mass	$kg\ mol^{-1}$
n	Number of cells	
N	Molar flux	$mol\ m^{-2}$
p	(Partial) pressure	Pa
Q	Heat	J
R	Universal gas constant or resistance	(-) or Ω

s	Entropy or liquid water saturation ratio	J mol^{-1} K^{-1} or (-)
T	Temperature	K
TC	Thermocouple	
t	Thickness	m
W	Mass flow rate	kg s^{-1}
z	Ratio of the species molar flux	

Greek:

γ	Volumetric condensation coefficient	s^{-1}
ε	Porosity	
η	Efficiency	
λ	Water content or ratio	
ρ	Density	kg m^{-3}
μ	Viscosity	kg m^{-1} s^{-1}
σ	Membrane conductivity	S m
τ	Torque	N m
φ	Relative humidity or flux linkage	(-) or V s rad^{-1}
ω	Angular velocity	rad s^{-1}

Superscripts, subscripts:

amb	Ambient
an	Anode
bl	Blower
c	Coolant
ca	Cathode

catl	Catalyst layer
cond	Conduction
conv	Convection
cv	Control volume
diff	Diffusion
elec	Electro-
evap	Evaporation
fc	Fuel cell
g	Gas
i	Index
im	Immobile
m	Motor
memb	Membrane
pl	Plumbing
rad	Radiator
res	Reservoir
s	Stator
sou	Source
st	Stack

Chapter 1 Introduction

1.1. Fuel cell technology

We require energy for electricity, heating, cooling, and fueling vehicles. Figure 1-1 shows a diagram representing the sources of energy and energy demand in the U.S. According to the survey [1], the transportation sector is heavily dependent upon fossil fuels: 97% of our energy is from petroleum and natural gas, while only 3% is from renewable energy sources. Our dependence on fossil fuel results in two challenging issues. First, an imbalance between supply and demand, and depletion in near future causes fluctuations in oil prices and makes the global economy vulnerable. Second, emissions due to combustion processes include chemicals that adversely affect health. In particular, the carbon dioxides have been identified as chemicals that cause global warming. Many universities, industries, and governments are seeking solutions to replace fossil fuels with renewable, sustainable, and economical fuels and related devices that convert the new fuels into electric, thermal, or mechanical energy.

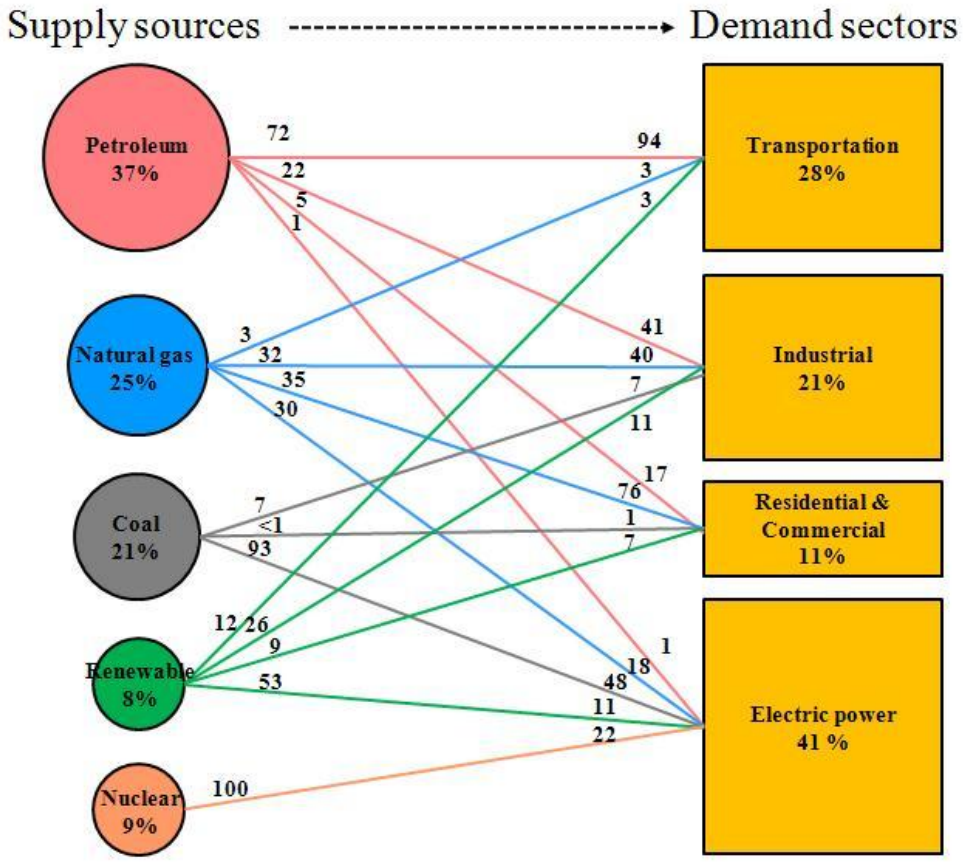

Figure 1-1. U.S. primary energy flow by source and demand sectors, 2009 [1].

A fuel cell is an electrochemical device that converts chemical energy into electrical energy. Fuel cell technology is considered to be a power source that can potentially replace traditional internal combustion engines (ICEs) due to its high efficiency, high power density, and low emissions. Fuel cell technology can be categorized by the type of electrolyte, fuel, and operating temperature as follows: polymer electrolyte membrane fuel cells (PEMFCs), direct methanol fuel cells (DMFCs), phosphoric acid fuel cells (PAFCs), molten carbonate fuel cells (MCFCs), and solid oxide fuel cells (SOFCs) [2]. These technologies have been demonstrated in a variety of applications as shown in Figure 1-2.

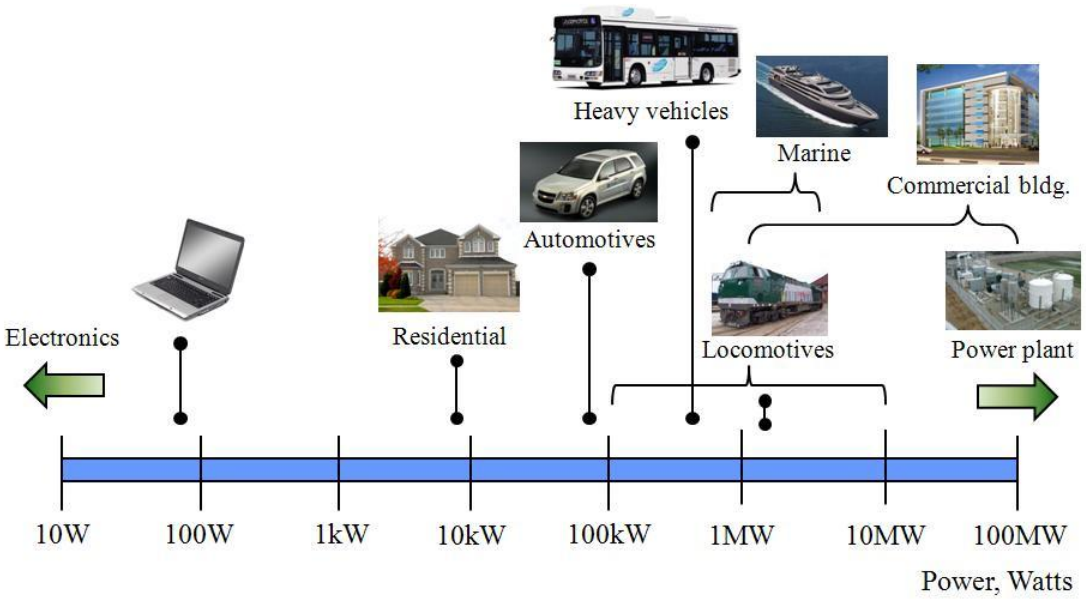

Figure 1-2. Applications of fuel cells.

Among these fuel cell technologies, PEM fuel cells have attracted attention for transportation applications because of their eco-friendliness, quite operation, low operating temperature, and high efficiency [2], [3]. For example, PEM fuel cells are very advantageous for electric vehicles because the driving range can be extended. As a result, the size of the required rechargeable batteries can be minimized [4]. In order to commercialize fuel cell technology for automotive applications, technical barriers must be overcome, and infrastructure such as refueling gas stations must be developed. The two barriers are durability and price. The lifespan of a fuel cell should be at least 5000 hrs, and the price must be comparable to that of ICEs (in the range of $30/kW) [5].

1.2. The PEM fuel cell system

A PEM fuel cell generates electricity and produces heat and water though an electrochemical reaction between oxygen and hydrogen. Since the electrical energy generated in a single fuel cell is very insufficient to power a vehicle, multiple cells are assembled into a stack. A PEM fuel cell system consists of a fuel cell stack and a balance-of-plant (BOP). The BOP manages reactant gases and removes byproducts such as heat and water. The subsystems of the BOP include air and hydrogen supply systems, thermal systems, and water management systems; these strongly affect the performance and durability of the fuel cell system. In particular, these subsystems play a significant role in ensuring highly efficient and reliable operations by maintaining proper operating conditions.

1.2.1. A PEM fuel cell

A typical PEM fuel cell structure, shown in Figure 1-3, is constructed of various components. These include gas flow channels (GFCs) that provide pathways for hydrogen and oxygen to gas diffusion layers (GDLs); gas diffusion layers that distribute the reactants evenly to catalyst layers (CLs) where electricity and water are generated on the cathode side; and a membrane located in the middle of the fuel cell that separates the anode and cathode while conducting hydrogen protons and blocking electrons.

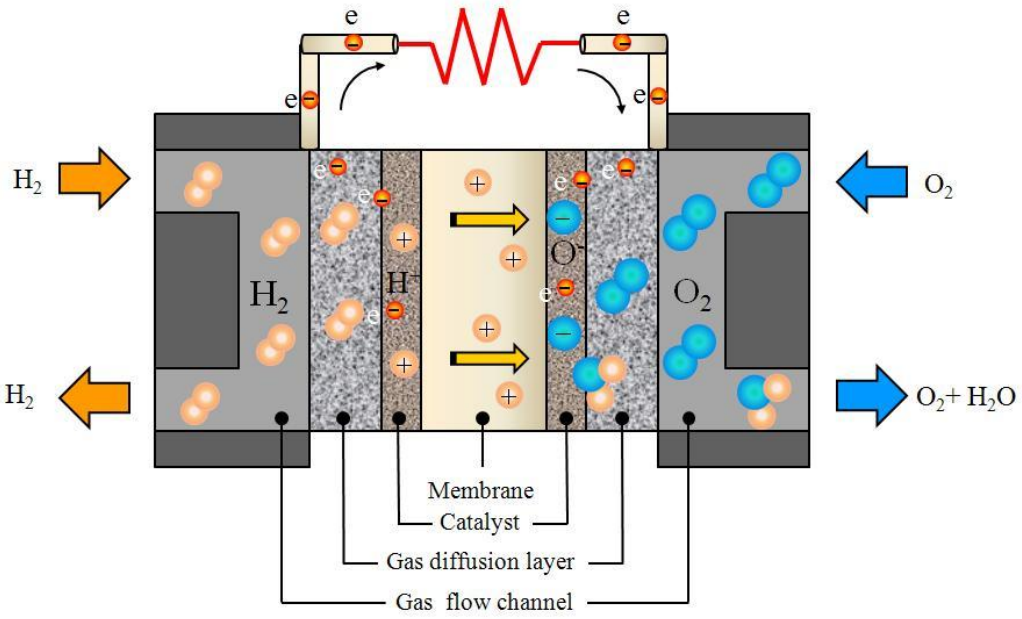

Figure 1-3. Schematic diagram of a PEM fuel cell.

During fuel cell operation, oxygen or air, and pure hydrogen from hydrogen storage, are supplied as reactant gases into the gas flow channels. Parts of the reactants diffuse into the gas diffusion layers. When hydrogen reaches the catalyst layer on the anode side, the hydrogen becomes ionized, releasing electrons and creating protons. This reaction occurring at the anode is called a hydrogen oxidation reaction (HOR). Electrons released by the HOR travel along an external circuit to the cathode side while the protons travel though membranes and arrive at the catalyst of the cathode side. Here, oxygen molecules react with protons permeating though the membrane, and with electrons arriving though the external circuit, thereby producing water molecules and heat. This reaction occurring in the cathode is called an oxygen reduction reaction (ORR), which can be written as follows:

$$2H_2 \Rightarrow 4H^+ + 4e^-$$
$$O_2 + 4H^+ + 4e^- \Rightarrow 2H_2O \qquad (1\text{-}1)$$

Water and heat are generated as byproducts of the electrochemical reactions. Water generated at the catalyst layer is transported though the gas diffusion layer and gas flow channel at the cathode side, and though the membrane to the gas diffusion layer and gas flow channel on the anode side.

Since protons take up water, there is a water concentration gradient in the membrane from the anode to the cathode. On the other hand, a difference in water concentration between the cathode and anode causes back diffusions. Therefore, the overall balance in the membrane is determined by these two phenomena. Depending upon operating conditions, the membrane could be dehydrated and thus require proper humidification. As the membrane is drying, the ohmic resistance for protons increases and potential losses increase. As a result, fuel cell performance decreases. On the other hand, when the water removal rate is lower than the water generation rate at the cathode, excessive water vapor in the GDL and CL can condense into liquid water. The accumulated liquid water blocks the pores, providing pathways for oxygen transport in the GDL and covers up the active sites in the CL. This results in degradation of the fuel cell's performance [6].

Therefore, water management in fuel cells is a challenging issue. The membrane should be properly humidified for all operating conditions, and at the same time water flooding at the cathode should be prevented to ensure pathways for the reactants. However, it has to be noted that the use of the highly pressurized air flow supplied to the fuel cell to remove water can increase the parasitic power of the air supply system.

The other byproduct resulting from electrochemical reactions is heat. Generated heat determines the temperature profiles inside the fuel cells, which directly influence the rates of chemical reaction and water transport. For example, increased temperature can ease the removal of water produced in the catalysts and increase the mobility of water in the membrane, thereby alleviating over-potentials. Conversely, a low operating temperature (less than 60 ^{o}C) could increase the rates of water condensation and flooding in the electrodes, which subsequently increases over-potentials because of increased flow resistance for reactant mass transport. In addition, a low operating temperature results in a low electrochemical reaction rate [6]. Therefore, thermal management is another challenging issue. However, improper rejection of heat might locally produce hotspots and destroy thin layers of cells

A fuel cell stack consists of multiple cells with end plates as shown in Figure 1-4. A unit cell is constructed with five components: a membrane electrode assembly (MEA), two GDLs, and two bipolar plates (BPs) at the cathode and anode sides. The MEA is referred to as the heart of the PEM fuel cell, and is usually made of a polymer electrolyte membrane sandwiched between two catalyst-coated carbon papers. The gas diffusion layer is made of porous media such as carbon fiber/cloth, and is used uniformly to diffuse reactant gases reaching the catalyst layer for chemical reaction. The bipolar plate located between cells performs as a current conductor between cells and provides flow channels for reactant gases and coolant. The current collector plate is made of highly conductive materials and is connected to an external circuit. The end plate of the fuel cell stack functions as the supporting structure for the fuel cells.

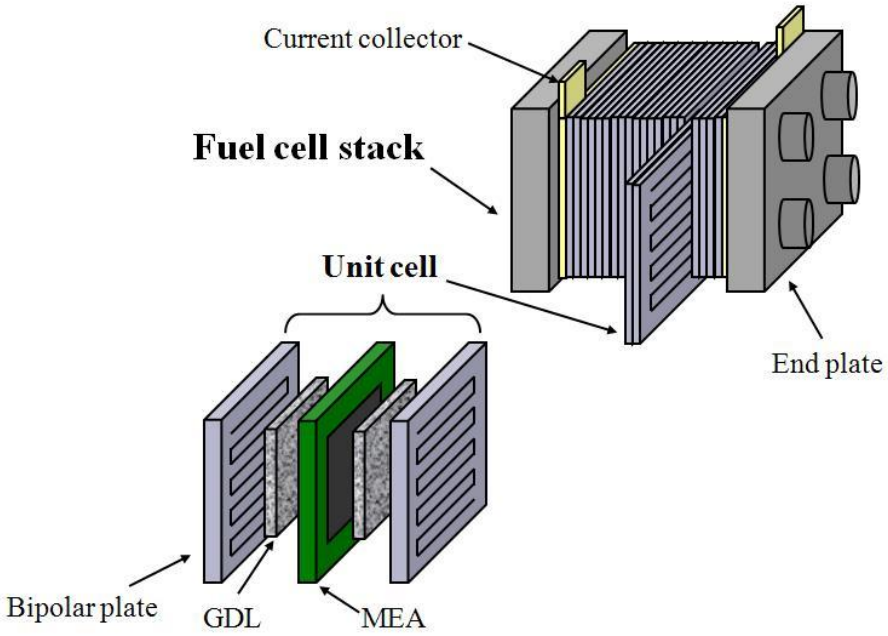

Figure 1-4. Construction of a fuel cell stack.

1.2.2. Balance-of-plant

A typical configuration of a PEM fuel cell system, including a fuel cell stack and the BOP, is shown in Figure 1-5. The BOP system consists of an air and water management system (blue line), a thermal management system (green line), and a hydrogen delivery system (red line).

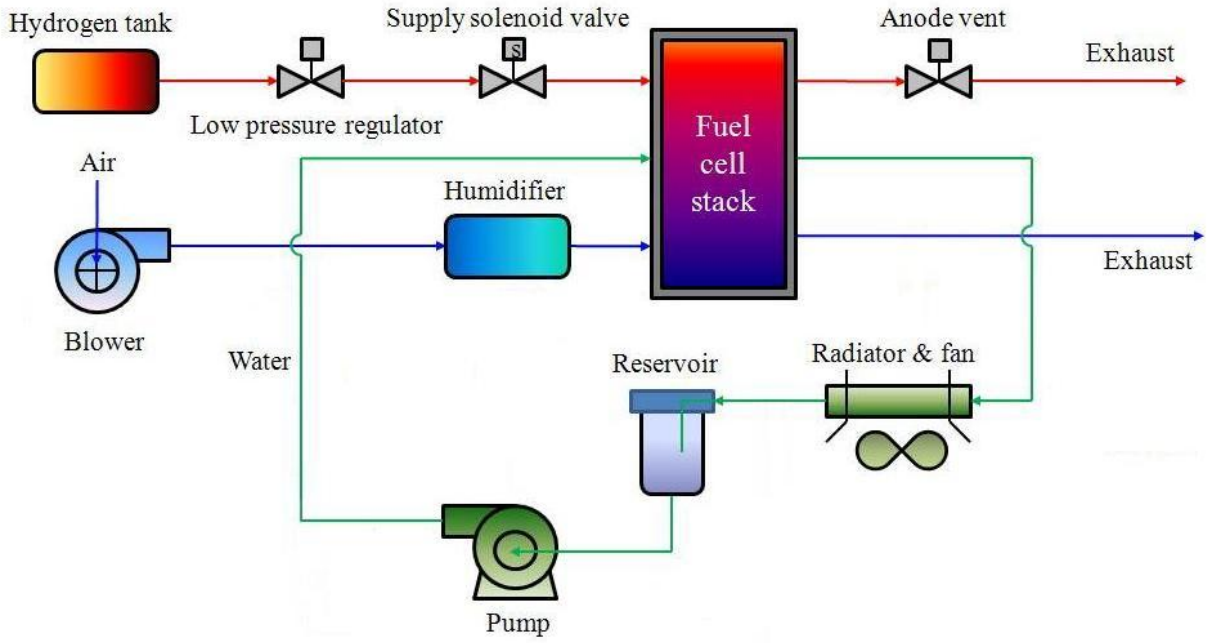

Figure 1-5. Schematic diagram of a PFM fuel cell system.

The main components of the air and water management system are a blower and a humidifier. Air supplied to the fuel cell stack by the blower is humidified by a humidifier. The thermal circuit includes a radiator to exchange heat with the ambient media, a fan to increase the effectiveness of heat convection, and a reservoir to store and thermally insulate the coolants. A coolant pump is used to supply coolant to the heat source.

The fuel delivery system consists of a hydrogen tank to store hydrogen, a low pressure regulator to control pressure, a supply solenoid valve to adjust flow rate, and a purge valve to remove excessive liquid water and impurities on the anodic side.

1.3. Literature review

1.3.1. Air supply system

1.3.1.1. The effects of oxygen starvation on a fuel cell

During operation, a sudden change of the oxygen demand such as start-up and load change, and water flooding can cause oxygen starvation [7]. Taniguchi *et al.* [8] observed that the decrease of the activation area in oxygen starved cell is related with the increase of the size of the catalyst particles, and disappearing of the small particles. A consequence of oxygen starvation is a rapid cell reversal [8]. When cell reversal occurs in the cathode catalyst, the proton and the electron are reduced to the hydrogen. During cell reversal, the heat is generated and results in the local hot spots, which give the damage to the fuel cells.

1.3.1.2. Strategies for air supply system

Currently, the control strategies for air supply system were proposed by many researchers. Rodatz *et al.* [10] proposed a dynamic model for a compressor that accounts the dynamics of the compressor and inlet and outlet manifolds filling processes. Based on the models, a regulator is designed by using the Linear Quadratic Gaussian (LQG) means and compared with a PI controller. The result shows that the use of the LGQ significantly improves the response time of the air supply.

Pukrushpan *et al.* [11] proposed different control strategies for an air supply system that optimally maintain the oxygen excess ratio that refers to a ratio between the oxygen consumed and supplied. A Static Feed-Forward control (sFF) solely based on a map date and a feedback control (sFB) based on observer are employed to increase robustness of the ratio at any load

applied and improve recovery dynamics. The optimization of the advanced controller gains is carried out by using the Linear Quadratic Gaussian (LQG).

Vahidi *et al.* [12] addressed phenomena of oxygen starvation that the air cannot be quickly delivered to the fuel cell at instant change of current because of the air flow rate limited by the dynamics of inlet manifold and operational constraints of compressor. Hybridization with a battery is proposed to minimize the oxygen starvation, which levels a peak load. Optimal balance of the two sources is carried out by the Model Predictive Control (MPC)

Zhang *et al.* [13] proposed an adaptive control algorithm to stabilize the oxygen excess ratio around an optimal level. The adaptive control includes the estimation of time-varying parameters in a stack and the pole assignment of the closed-loop system. Finally, the proposed adaptive control was evaluated on a test bench.

1.3.2. Water management

1.3.2.1. The effects of water management on a fuel cell

A schematic diagram for the mechanism of water transport in a cell is shown in Figure 1-6. During operation, there are two source terms for water transport mechanism, which are ones supplied by humidification of reactant gases and generated internally by the ORR. Water transport in membranes occurs through two forces: an electro-osmotic driving force and back diffusion. The former moves water from the anode to the cathode along with protons. The latter is caused by a concentration gradient of water across the membrane that moves water from the cathode to the anode. In addition, water at the catalyst layer is transported though the gas diffusion layer into the gas flow channels, and is then exhausted at the fuel cell outlet by diffusion and capillary forces combined with pressure in the gas flow channels.

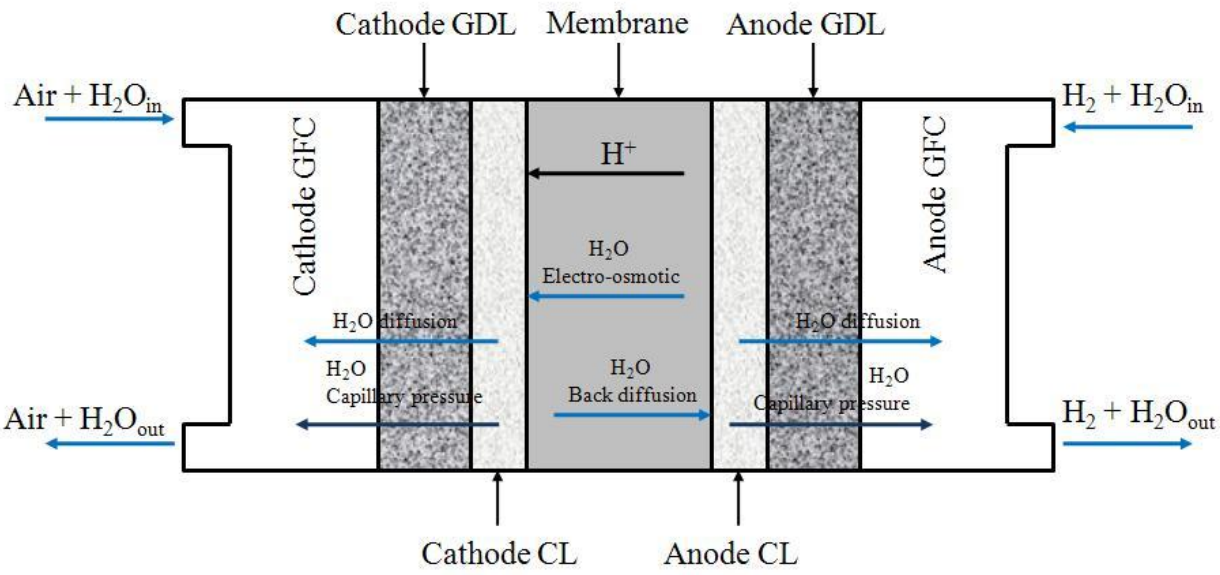

Figure 1-6. Schematic diagram of mechanism of water transport.

If the water removal rate is higher than the water generation rate, the membrane water content decreases, which increases ohmic resistance for proton transport. Consequently, potential losses in the membrane become higher, fuel cell performance is degraded, and the membrane may be permanently damaged under severe drying conditions [6].

Conversely, when the water generation rate by electrochemical reaction exceeds the water removal rate by diffusion of water vapor and capillary transport of liquid water from the GDL and the CL, the water vapor is oversaturated and condensed. Liquid water that has accumulated in the porous gas diffusion and catalyst layers blocks the gas pores used for oxygen transport to the catalyst layer [14], [15], and covers up active areas of the catalyst layer. This leads to fewer oxygen reduction reactions. In addition, excessive water transport leaches impurities within the cell and deposits them on catalysts or the membrane. This results in increasing ohmic and mass transport loss [16]. Flooding occurs under certain operating conditions such as low temperature,

high relative humidity of fuel cell entering gases, and a high current density region where the water vapor inside the fuel cell becomes oversaturated and condensed on the cathode side.

Flooding occurs depending on interaction of the properties of the components and operating conditions. The effects of the catalyst layer on water management have rarely been studied experimentally or numerically, in contrast to numerous studies on the effects of the GDL and GFC on water management. Eikerling and Kornyshev [17] considered the effects of the cathode catalyst layer relating to water handling ability and cell performance. The results show that the cathode catalyst layer is a prime component for the conversion of liquid water to vapor, and regulates the water flux balance between the GDL and the membrane.

The gas diffusion layer plays the most significant role in the water flow that maintains the sensitive balance between membrane hydration and water removal. To help repel water from catalysts, the GDL is often treated with hydrophobic materials (e.g., polytetrafluoroethylene (PTFE)) to change its wetting characteristics. In addition, a micro-porous layer (MPL) is often added between the GDL and the CL, which boosts water removal and assists in the distribution of reactant gas flows to catalyst surfaces.

The water transported from the GDL to the GFC depends on water management along the GFC. Two different and widely used flow patterns are the inter-digitated and serpentine flow fields. The capability of water removal depends on the operating conditions. Therefore, an understanding of the effects of operating conditions on water transport is important.

The key operating conditions for the PEM fuel cell are the flow rates of the reactants with respect to the stoichiometric number and back pressure; the inlet humidity of the reactant gases; and coolant flows for maintaining cell temperature. Generally, the humidified reactant gases supplied to the fuel cell ensure membrane hydration in the low current density region. However,

in the high current density region where more water is generated, highly humidified reactant gases may cause water flooding at the cathode.

Back pressure and stoichiometric numbers affect the pressure drop of two-phase flow, which is directly related to water movement in the GDL and along the flow channels. The operating temperature determines the saturation levels of the reactant gas flows in the GDL and the CL, which in turn are related to evaporation and condensation rates. When the cell temperature increases, more liquid water is evaporated and the water flooding level becomes low [18].

Cell performance strongly depends on the maintenance of membrane hydration and on the prevention of water flooding. To achieve these objectives, considerable research has been conducted in developing design and operating strategies for proper water management. The main strategies developed thus far for humidification of the membrane and/or the mitigation of water flooding are summarized as follows.

1.3.2.2. Strategies for water management

a. Design of the flow field and MEA

An appropriate design of gas flow channels is the most successful approach to the prevention of water flooding. Two typical flow patterns are the inter-digitated and serpentine flow fields, as shown in Figure 1-7. The inter-digitated flow field proposed by Nguyen [19] consists of dead-end inlet and outlet channels. This design provides a higher transport rate of gases than a conventional flow field with straight parallel channels because incoming reactant gases are forced to flow though the GDL to the catalyst layer. As a result, shear force exerted by the gas flow flushes liquid water out of the cathode. Water flooding is reduced, and fuel cell performance is significantly improved. However, forcing reactant gases to flow into the GDL

requires high pressure, which results in significant parasitic power loss. Furthermore, highly enhanced mass transport in the GDL could lead to membrane dehydration at low current density [20].

In contrast, the serpentine flow field is the most widely known and used because it ensures better performance and durability [21]. The gas flows along the main channels in this design, and there are cross-sectional small channels that create a high pressure drop between adjacent main channels. This high pressure drop drives a cross-leakage flow between adjacent main channels and through the gas diffusion layer, which makes water removal easier. However, it requires significant parasitic power loss because of the high pressure drop. Moreover, this design often causes membrane dehydration near the channel inlet while water flooding occurs near the channel outlet because of excessive water removal by the gas stream. For a dry reactant stream or for cases in which operations occur at less than 100% relative humidity, a single serpentine flow field can result in membrane dehydration that leads to degradation of cell performance in the low current density region [22].

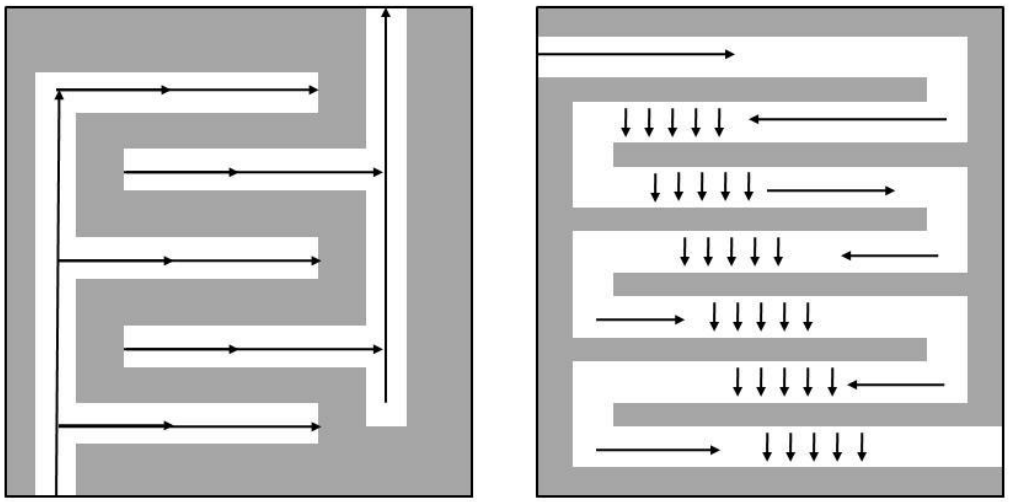

Figure 1-7. Flow field designs: (a) interdigitated and (b) serpentine flow fields.

In addition to a channel design strategy, incorporation of special hydrophilic wicking structures into cathode flow channels can help redistribute liquid water. For example, Ge *et al*. [23] proposed an internally humidified polymer electrolyte fuel cell (PEFC) mounted with two strips of absorbent polyvinyl alcohol sponge. Their results show that the mounted sponge wicks were sufficient to humidify dry air flow entering the fuel cell, and to remove water produced in a cell under correct operating conditions. However, this humidification strategy did not work under abnormal conditions such as high temperature, a high gas stoichiometric ratio, and low pressure.

Ihonen *et al*. [14] proposed treating the GDL with hydrophobic materials such as polytetrafluoroethylene (PTFE); this would allow separate paths for gas and liquid transport. Water removal improves using this approach. Spernjak *et al*. [24] investigated liquid water formation and transport in the PEM fuel cell using untreated carbon cloth, untreated carbon paper, and 5 wt.% PTFE-treated carbon fiber. Experimental results show that water emerged as droplets over the surface of the flow channels for PTFE-treated carbon fiber, whereas the water moved along the sidewall of the flow channels in the form of films and slugs for the untreated carbon cloth and paper. Under the same operating conditions, the gas flow channel with PTFE-treated GDL has a higher quantity of liquid water than that of the untreated GDL, which indicates that the water is efficiently removed from the catalyst layer.

Qi and Kaufman [25] experimentally studied the performance of single cells with and without micro-porous layers (MPLs), which are added to conventional GDLs to improve water removal from the catalyst layer.

Freire and Gonzalez [26] investigated the effects of membrane characteristics and humidification conditions on the impedance response of cells. Their results showed that thinner

membranes shortened the water back-diffusion process, reduced the anode to be humidified, and lowered the ionic resistance or ohmic losses though the membrane. However, thinner membranes often cause poor durability and high gas crossover rates, which limits the practical membrane thickness for fuel cell applications.

The internal humidification systems have advantages such as compact and lightweight structures. However, their performance in a fuel cell system with internal humidification was lower than that of external humidification, and the operating conditions were limited.

b. Operating conditions

Water balance in a cell can be operationally manipulated by removing the water present on the anode side and by using an electro-osmotic pump. Buchi and Srinivasan [27] investigated operation of a PEM fuel cell without external humidification of the reactant gases. The dry reactant gases were humidified by the water produced in a cell. Since back diffusion is the dominant factor for water flow though a membrane in the low current density region, hydrogen on the anode side is internally humidified. However, the operation of fuel cells with an internal humidification system is limited for certain gas flow rates and cell temperatures. The performance of a cell without humidification is 20 to 40% lower than for the case using both humidified gases.

Wilkinson *et al*. [28] proposed a strategy to control cathode water flooding. An appropriately designed stack can draw liquid water accumulated in the cathode by a concentration gradient across the membrane to the anode, and remove it into the fuel stream without additional parasitic power loss. Also, anode water removal can be achieved by high differential gas pressure between

the cathode and the anode, which forces liquid water transport though the membrane from the cathode to the anode [29]. However this strategy requires a relatively high operating pressure that can result in significant parasitic power loss and membrane rupture during operation. On the other hand, Buie *et al*. [30] proposed the use of an electro-osmotic (EO) pump to prevent water flooding. For example, two porous glass EO pumps were placed against the wall of cathode flow channels. During operation, liquid water formed in the GDL was forced out of the GDL and transformed into water droplets. Liquid water droplets were drawn into a hydrophilic porous glass structure of the EO pump. Once the EO pump structure was properly saturated, the EO pump actively drove the water though the porous glass structure into the integrated water reservoirs in the acrylic top plate. It was reported that an EO pump has the capability of preventing cathode flooding as well as enhancing the performance of partially flooded fuel cells using a small fraction of the fuel cell's power.

1.3.3. Thermal management

1.3.3.1. Effects of thermal management on a fuel cell

Proper thermal management has been recognized as a crucial issue that must be resolved for the commercialization of fuel cell vehicles [31], [32]. The PEM fuel cells developed thus far operate in a temperature range of 60 to 80 ^{o}C. This temperature range is determined by the properties of membrane materials such as Nafion®, whose working temperature is commonly limited to 80 ^{o}C. When the working temperature is lower than 60 ^{o}C, water condensation can be accelerated. Subsequently, water flooding occurs, which results in voltage losses due to extra flow resistance of reactant mass transport. In addition, a low operating temperature causes low proton conductivity and electrochemical reaction rates. Therefore, appropriate thermal

management is required to maintain the working temperature of the cells at the desired level. The time dependent temperature profile can be described by an energy equation that includes heat source terms and heat transfer to components and the ambient. During operation, heat in a single cell is generated by entropic changes from chemical reactions, activation over-potential on the anode and cathode, and ohmic over-potentials [31], [33]. Joule heating is caused by ohmic resistances caused by the conduction of both protons and electrons. The percentages of heat generated by these source terms are approximately 55%, 35%, and 10%, respectively [31].

The heat generated in a stack is rejected by the cooling system, or transferred by convection or radiation across the surface of the stack. The heat rejection rate for the stack is determined by the thermal properties of the individual components of the stack. Different heat transfer rates and mechanisms have been observed in different components. The heat transfer mechanism through the membrane is primarily heat conduction, while both conduction and convection have significant heat transfer contributions in the GDL, CL, and GFC.

Insufficient heat rejection induces various thermal stresses on components that can cause loss of catalysts, membrane dehydration, and cathode flooding. For example, Bi and Fuller [34] analyzed the effects of temperature on cathode Pt/C catalyst durability. High temperature accelerates Pt/C degradation, loss of Pt catalyst active area, and deposition of Pt in the membrane, which results in a decrease of cell potential with operating time.

On the other hand, high operating temperature increases water removal from both the cathode and anode, and increases the mobility of water in the membrane. As a result, the membrane may be exposed to dehydration that causes the high ohmic resistance of the membrane, which leads to low conductivity of protons. Moreover, according to Maggio *et al.* [35], the cathode flooding

phenomenon, which is dominated by condensation/evaporation processes in the cathode, is heavily affected by the temperature distribution.

1.3.3.2. Strategies for thermal management

He *et al.* [36] proposed a temperature fuzzy control strategy. The PEMFC temperature and circulating coolant inlet temperature are controlled by regulating the coolant flux and bypass valve opening factor, respectively. The simulation results showed that the fuzzy controller with integrator effectively controlled the PEMFC temperature and the inlet coolant temperature within the desired working temperature ranges. Moreover, the author claimed that the proposed control system can be easily applied in various power classes of PEMFC temperature control in real-time due to its concise modeling and control process.

Wen *et al.* [37] proposed combined passive and active cooling system for PEM fuel cell. While six thermally conductive Pyrolytic Graphite Sheets (PGSs) inserted to six central cathode gas channel plates are used for passive cooling as heat spreaders and fins, two small cooling fans are used for forced convection. In addition, three other cooling configurations with differently sized fans are tested and compared.

Yu and Jung [38] proposed a thermal management strategy of a PEMFC system with a large active area for transportation applications, which is based on the investigation and the numerical experiments with a thermal management system. The cell temperature was effectively regulated by the coolant pump and cooling fan based on feedback control.

As previously discussed, thermal, air, and water management strongly affects the performance and reliability of cells, and further research and development of novel designs and operating strategies is required.

1.4. Objectives of this dissertation

The PEM fuel cell system is a candidate to replace the internal combustion engine. To ensure high performance, reliability, and durability, humidified air should be properly supplied and the heat produced should be rejected. Therefore, the objectives of this dissertation are to research and develop control strategies for the air, water, and temperature. To accomplish these objectives, dynamic models of components were developed and associated controls were designed in combination with new system configurations that work more effectively and efficiently than current systems. Simulations were conducted to analyze the static and dynamic performance of the system configurations with controls, and the subsequent effects on behavior. Finally, experiments were performed to validate and evaluate the performance of the controls.

The objectives of this dissertation are summarized as follows:

1. Improvement of dynamic response at an abrupt change of loads.
2. Maintenance of the optimal oxygen excess ratio.
3. Prevention of membrane dehydration and water flooding.
4. Optimal heat transfer by increased cooling effectiveness.
5. Maximizing the net power by reducing parasitic power sources.

Chapter 2 Model Development of PEM Fuel Cell

Most of the internal variables in an operating stack are hard to measure because the cells, composed of thin layers, are fully sealed and inaccessible. Moreover, the relationship between variables in operating cells (as well as in stacks) makes it difficult for design engineers to understand the interrelated mechanisms of the operating variables, and to design the stack. Therefore, dynamic models were developed and simulations were conducted to study the phenomena and behavior of PEM fuel cells.

Many researchers have proposed models for a single cell and stack. Amphlett *et al*. [39] proposed empirical equations representing the current-voltage (I-V) characteristics of a cell at different operating temperatures. However, their model is based on empirical equations and is not able to represent the dynamics of gases and water inside the fuel cell, or the varying load. Pukrushpan *et al.* [40] proposed a fuel cell stack model that considers the dependence of proton conductivity on water concentration and temperature. However, the water concentration of the membrane was obtained from the relative humidity (RH) of the membrane that was assumed to be the average of the anode and the cathode RH values. The water content in the membrane was greater than that of the cathode and the anode sides. Their developed model assumed no temperature gradient in the stack, and the behavior of the stack was obtained from the product of the number of cells multiplied by the single cell outputs. A one-dimensional (1-D) thermal model developed by Khandelwal *et al*. [41] was used to predict the temperature distribution for a cold

start. However, the model did not provide a transient analysis of the temperature for a varying load. The effects of a varying load on the dynamics of temperature were investigated by Shan and Choe [42]. However, all of the aforementioned models assumed that the water in a stack exists as vapor, or ignored phase changes. McKay *et al*. [43] developed a simple two-phase model for a gas diffusion layer, and used it to represent the effects of liquid water and vapor on the performance of the cells. The proposed model did not consider the variation of temperature, and its effects on the performance of a stack and the water balance in the membrane.

In this chapter, several developed fuel cell stack models are described for conditions such as isothermal, non-isothermal, and two-phase effects.

2.1. Dynamic fuel cell model

2.1.1. Model setup

A schematic diagram of the stack model is shown in Figure 2-1. The stack model consists of sub-models that include a stack terminal voltage, an anode, a cathode, and a membrane model. Pressure, temperature, reactant gas partial pressures, and membrane humidity are the main variables that affect stack voltage.

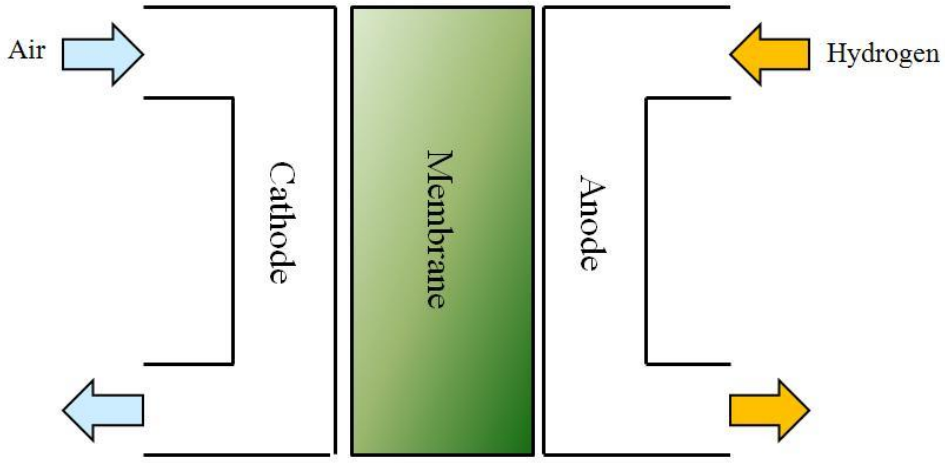

Figure 2-1. Schematic diagram of a fuel cell.

The main assumptions made for the fuel cell stack model are as follows:

1. All gases obey the ideal gas law.
2. The temperature of the flow inside the cathode flow channel is equal to the stack temperature of 80 ℃.
3. When the relative humidity of the gas exceeds 100%, vapor condenses into liquid form. This liquid water does not leave the stack, and either evaporates in the cathode gas if the humidity drops below 100%, or accumulates in the cathode.
4. The flow channel and cathode backing layer are lumped into one volume.

Based on these assumptions, four sub-models were developed as shown in Figure 2-2. The stack voltage, cathode flow, anode flow, and membrane model are described in the following sections.

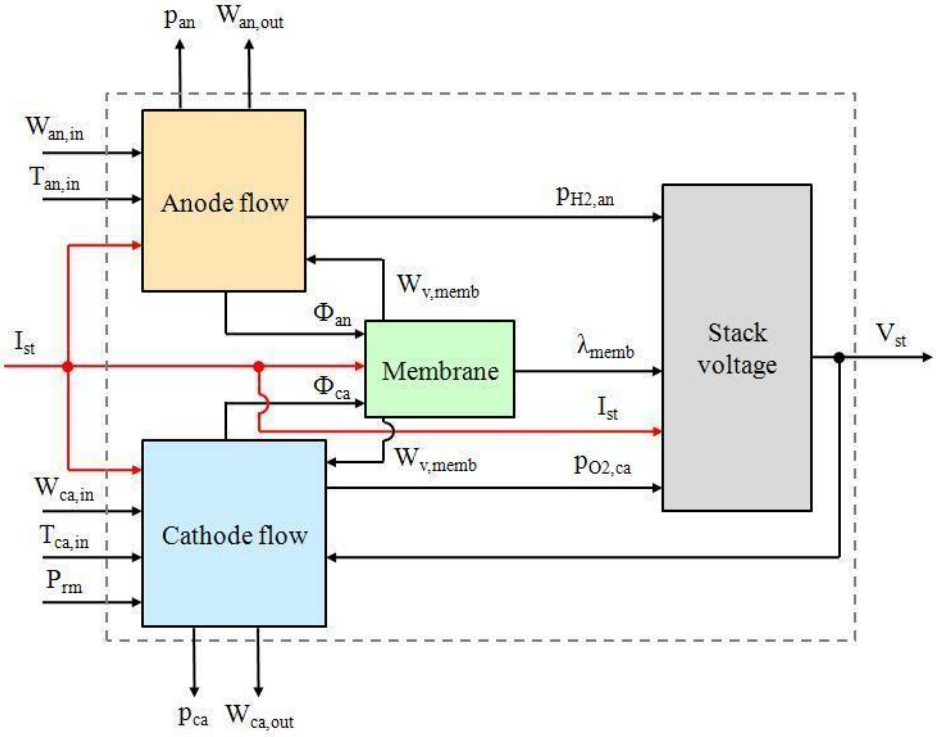

Figure 2-2. Block diagram for a fuel cell stack at constant temperature.

2.1.2. Governing equations

a. Stack voltage

The current-voltage (I-V) characteristic is the difference between the open circuit voltage and over-potentials that include the ohmic over-potential in the membrane, the activation over-potential in the catalyst on the cathode side, and the concentration over-potential. The relationship for a single cell may be written as a function of physical parameters such as the reactant partial pressure, temperature, current, and membrane water content [39], as shown in Figure 2-2. The output terminal characteristic of a stack is assumed to be a multiple of a single cell characteristic, and is given as follows:

$$v_{cell} = E(p,\ T) - v_{act}(p,\ T,\ i) - v_{ohm}(T,\ i,\ \lambda_{memb}) - v_{conc}(p,\ T,\ i)$$
$$v_{stack} = n \times v_{cell} \tag{2- 1}$$

where E is the open circuit voltage (V) given by converting chemical energy into electrical energy; v_{act} is the activation over-potential (V) necessary for electron transfer as well as dissolving and forming chemical bonds of electrons at the catalysts; v_{ohm} is the ohmic over-potential (V) that occurs because of the resistance of the membrane to the transfer of protons and the resistance of the electrode and collector plate to the transfer of electrons; and v_{conc} presents a concentration over-potential (V) resulting from the changes in concentration of the reactants as they are consumed in the reaction.

The open circuit voltage E is expressed using an energy balance between chemical energy and electrical energy [39]:

$$E = 1.23 - 0.85 \times 10^{-3} \cdot (T_{fc} - 298) + 4.31 \times 10^{-3} \cdot T_{fc} \cdot \left[\ln(p_{H_2}) + \frac{1}{2} \cdot \ln(p_{O_2}) \right] \tag{2- 2}$$

The activation over-potential v_{act} is obtained using the Tafel equation [44]:

$$v_{act} = v_0 + v_a \cdot (1 - e^{-c_1 \cdot t}) \tag{2- 3}$$

where v_0 and v_a are functions of cell temperature, cathode pressure, and oxygen partial pressure, and c_1 is equal to 10.

The ohmic over-potential v_{ohm} [45] is calculated from Ohm's law:

$$v_{ohm} = i \cdot R_{ohm} \tag{2- 4}$$

where the ohmic resistance R_{ohm} (Ω) is a function of membrane conductivity σ_{memb} (S m) and membrane thickness t_{memb} (m) as follows:

$$R_{ohm} = \frac{t_{memb}}{\sigma_{memb}} \tag{2- 5}$$

The membrane conductivity at different hydration levels of the membrane can be given in the following form [44]:

$$\sigma_{memb} = \sigma_{30} \cdot \exp\left[1268 \cdot \left(\frac{1}{303} - \frac{1}{T_{fc}}\right)\right] \quad (2\text{-}6)$$

where σ_{30} is a function of the membrane water content. The value of the membrane water content varies between 0 and 14, which can be equivalently related to relative humidity values of 0 and 100% [44].

The concentration over-potential v_{conc} is given by

$$v_{conc} = i \cdot \left(c_2 \cdot \frac{i}{i_{\max}}\right)^{c_3} \quad (2\text{-}7)$$

where c_2 is a fitting constant described in [46], and i_{max} and c_3 are 2.2 and 2.0, respectively.

b. Cathode and anode flows

The dynamics of the air flow on the cathode side is described using mass conservation equations in the control volume, separately considering the mass rates of oxygen, nitrogen, and water on the cathode side:

$$\begin{aligned} \dot{m}_{O_2,ca} &= W_{O_2,ca,in} - W_{O_2,ca,out} - \dot{m}_{O_2,reacted} \\ \dot{m}_{N_2,ca} &= W_{N_2,ca,in} - W_{N_2,ca,out} \\ \dot{m}_{w,ca} &= W_{v,ca,in} - W_{v,ca,out} + \dot{m}_{v,gen} + W_{v,ca-memb} \end{aligned} \quad (2\text{-}8)$$

where $W_{v,ca\text{-}memb}$ is the mass flow rate of water across the membrane.

The mass rates of oxygen reacted and water generated by the chemical reaction are functions of the stack current:

$$W_{O_2,reacted} = M_{O_2} \cdot \frac{n \cdot I_{st}}{4 \cdot F}$$
$$W_{v,gen} = M_v \cdot \frac{n \cdot I_{st}}{2 \cdot F} \quad (2\text{- }9)$$

where M denotes the molar mass (kg mol^{-1}).

Similarly, the mass rate on the anode side can be described as

$$\dot{m}_{H_2,an} = W_{H_2,an,in} - W_{H_2,an,out} - \dot{m}_{H_2,reacted}$$
$$\dot{m}_{w,an} = W_{v,an,in} - W_{v,an,out} - W_{v,an-memb} \quad (2\text{- }10)$$

where the mass rates of hydrogen reacted by the chemical reaction is a function of the stack current:

$$W_{H_2,reacted} = M_{H_2} \cdot \frac{n \cdot I_{st}}{2 \cdot F} \quad (2\text{- }11)$$

c. Membrane

The membrane water content is the factor that determines proton conductivity. The dynamics of the water content are described by two forces: the electro-osmotic driving force exerted by the different electrochemical potentials at the anode and cathode, and diffusion caused by the gradient of the water concentration at the two boundaries. Considering the water mass that flows at the boundaries of the membrane layer, the dynamics of the water concentration in the membrane can be improved compared to the membrane model in [40] as follows [42]:

$$\lambda_{memb} = \frac{C_{H_2O} / M_{H_2O}}{\frac{\rho_{dry,memb}}{M_{memb}} - b \cdot C_{H_2O} / M_{H_2O}} \quad (2\text{- }12)$$

$$\dot{m}_{w,memb} = \frac{d\left(C_{H_2O} \cdot A_{cell} \cdot t_{memb}\right)}{dt} = W_{elec,memb-an} - W_{elec,memb-ca} + W_{diff,memb-an} + W_{diff,memb-ca} \quad (2\text{- }13)$$

where C is the mass concentration (kg m^{-3}), M is the mole mass (kg mol^{-1}), b is the parameter given in [40], ρ is the membrane dry density (kg m^{-3}), and A_{cell} is the fuel cell area (m^2).

The electro-osmotic driving force determines the water mass flows of $W_{elec,memb\text{-}an}$ and $W_{elec,memb\text{-}ca}$ at the boundaries of the membrane layer. In addition, diffusion produces the mass flows of $W_{diff,memb\text{-}an}$ and $W_{diff,memb\text{-}ca}$. These relationships are described as follows, as proposed in [39]:

$$n_d = 0.0029 \cdot \lambda_i^2 + 0.05 \cdot \lambda_i - 3.4 \times 10^{-19} \tag{2- 14}$$

$$W_{elec,memb-i} = M_{H_2O} \cdot A_{cell} \cdot n_{d,i} \cdot \frac{i}{F} \tag{2- 15}$$

$$W_{diff,memb-i} = M_{H_2O} \cdot A_{cell} \cdot D_w \cdot \frac{(C_i - C_{memb})}{F} \tag{2- 16}$$

where the diffusion coefficient D_w is calculated using the following empirical equation:

$$D_w = D_\lambda \cdot \exp\left[2416 \cdot \left(\frac{1}{303} - \frac{1}{T_{fc}}\right)\right] \tag{2- 17}$$

$$D_\lambda = \begin{cases} 10^{-6}, & \lambda_i < 2 \\ 10^{-6} \times (1 + 2 \cdot (\lambda_i - 2)), & 2 \le \lambda_i \le 3 \\ 10^{-6} \times (3 - 1.67 \cdot (\lambda_i - 3)), & 3 < \lambda_i < 4.5 \\ 1.25 \times 10^{-6}, & \lambda_i \ge 4.5 \end{cases} \tag{2- 18}$$

Boundary water content λ_i is a function of water activity a_i, which is calculated from the water vapor partial pressure as follows:

$$\lambda_i = \begin{cases} 0.043 + 17.8 \cdot a_1 - 39.85 \cdot a_i^2 + 36 \cdot a_i^3, & 1 \ge a_i > 0 \\ 14 + 1.4 \cdot (a_i - 1), & 3 \ge a_i > 1 \\ 16.8, & 3 \le a_i \end{cases} \tag{2- 19}$$

$$a_i = \frac{p_{v,i}}{p_{sat,i}(T_i)} \tag{2- 20}$$

2.2. Non-isothermal dynamic fuel cell model

The model described in Section 2.1 ignores the effects of the temperature gradient on the behavior of a real fuel cell. The developed non-isothermal model [42] includes the temperature distribution in the through-plane of a cell, its effects on the characteristics of each component in the fuel cell, and the dynamic water balance in the membrane.

2.2.1. Model setup

The proposed fuel cell model was developed on the basis of layers in a single cell stack that consist of a membrane-electrode-assembly (MEA), two gas diffusion layers, and two gas flow channels sandwiched between coolant channels, as shown in Figure 2-3. The input variables for the model are the load current, mass flow rates, temperature, pressure, relative humidity of the reactants, and the temperature and flow rate of coolants at the inlets.

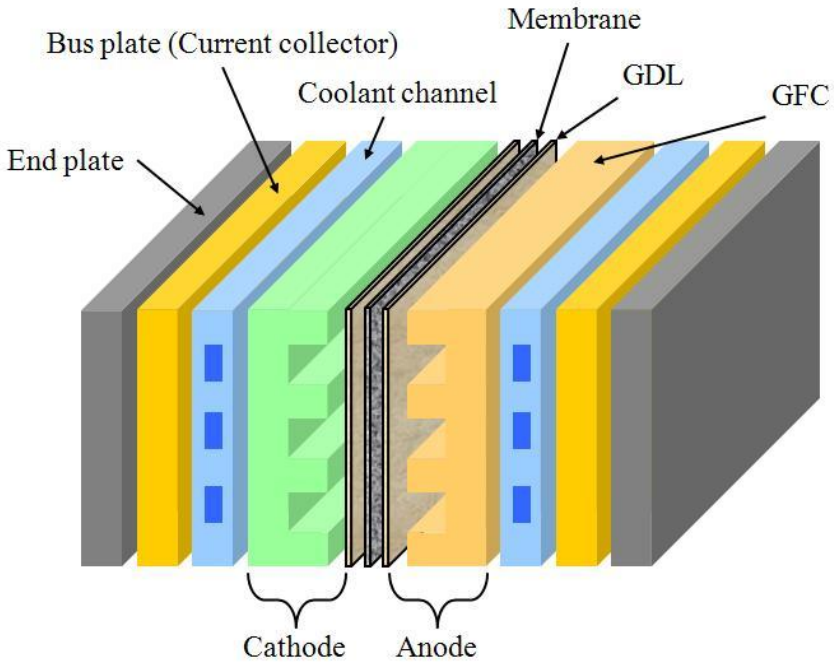

Figure 2-3. Schematic diagram of a single cell stack.

The main assumptions made in the development of the model are as follows:

1. The reactants are ideal gases.
2. No pressure gradient exists between the cathode and the anode (gas is transported only by diffusion).
3. No pressure drop exists along the gas flow channels.
4. The temperature gradient is linear across the layers in the fuel cell.
5. Anodic over-potential is negligible.
6. There is no current density gradient across the cathode catalyst layer.
7. Latent heat is not considered.

Models for the layers in a fuel cell were developed based on these assumptions, and are described in following sections.

2.2.2. Governing equations

a. Stack voltage

The I-V characteristic is given by the difference between the open circuit voltage *E* and the over-potentials that include the activation over-potential in the catalyst on the cathode side v_{act}; the ohmic over-potential in the membrane v_{ohm}; and the concentration over-potential v_{conc}. Thus, we have

$$v_{cell} = E - v_{act} - v_{ohm} - v_{conc} \tag{2- 21}$$

The equations for the open circuit voltage and the ohmic over-potential are the same as those presented in Section 2.1.2. However, the equations for the activation and concentration over-potentials should consider temperature and therefore need to be modified.

The activation over-potential v_{act} can be expressed as a function of working temperature, oxygen concentration, and current [39]:

$$v_{act} = \xi_1 + \xi_2 \cdot T + \xi_3 \cdot T \cdot \ln\left(c_{O_2}\right) + \xi_4 \cdot T \cdot \ln\left(I_{st}\right) \tag{2- 22}$$

where ξ is the constant parametric coefficient, *I* is the load current (A), and *c* is the concentration (kg m^{-3}).

The concentration over-potential v_{conc} is given by the following approximation:

$$v_{conc} = -b \cdot \ln\left(1 - \frac{i}{i_{\max}}\right) \tag{2- 23}$$

where *b* is a parametric coefficient (V) that was derived from the single cell characteristic and is assumed to be identical throughout all of the cells in the stack, and *i* and i_{max} denote the actual and the maximum current density (A cm^{-2}), respectively.

Finally, the stack voltage is the product of the number of cells and the terminal voltage of the single cell voltage:

$$v_{st} = n \cdot v_{cell} \tag{2- 24}$$

Electrochemical parameters used for the stack model were obtained by curve-fitting method based on experimental data [47].

b. Energy balance

Consider a cell that is assembled with cubical layers in which the thermo-physical properties are isotropic and constant. Then, according to the energy conservation equation, the total energy changes in a controlled volume are equal to the sum of the energy exchange at the boundaries and the internal energy resources. The energy exchanges at boundaries occur due to two factors: conduction across the cell, and convection occurring between bipolar plates with the coolant, reactants, and water. The thermal behavior can thus be described by the following energy conservation equation [42]:

$$\sum_i m_i \cdot Cp_i \cdot \frac{dT_{cv}}{dt} = \underbrace{\sum W_{in} \cdot Cp_j \cdot \left(T_{in} - T_{cv}\right)}_{\text{Mass flow in}} + \underbrace{\dot{Q}_{conv}}_{\text{Convetin heat transfer}} + \underbrace{\dot{Q}_{cond}}_{\text{Conduction heat transfer}} + \underbrace{\dot{Q}_{sou}}_{\text{Sources}} \tag{2- 25}$$

The internal energy source is composed of the entropy losses and the chemical energy required for protons to overcome the barrier of the over-potentials in both catalyst layers. In addition, there are ohmic losses caused by transport of electrons and protons in the cell [48]. Thus,

$$\dot{Q}_{sou} = i \cdot A_{cell} \cdot \left(-\frac{T \cdot \Delta s}{4 \cdot F} + v_{act} + i \cdot A_{cell} \cdot R_{memb} \right) \quad (2\text{-}26)$$

where the entropy change Δs is equal to -163.0 (J mol^{-1} K^{-1}) [49], v_{act} is given in [39], and R_{memb} is the membrane resistance Ω. We note that the anodic entropy change becomes zero under the assumption that the anode is a standard electrode.

A block diagram between two control volumes for the energy balance is shown in Figure 2-4.

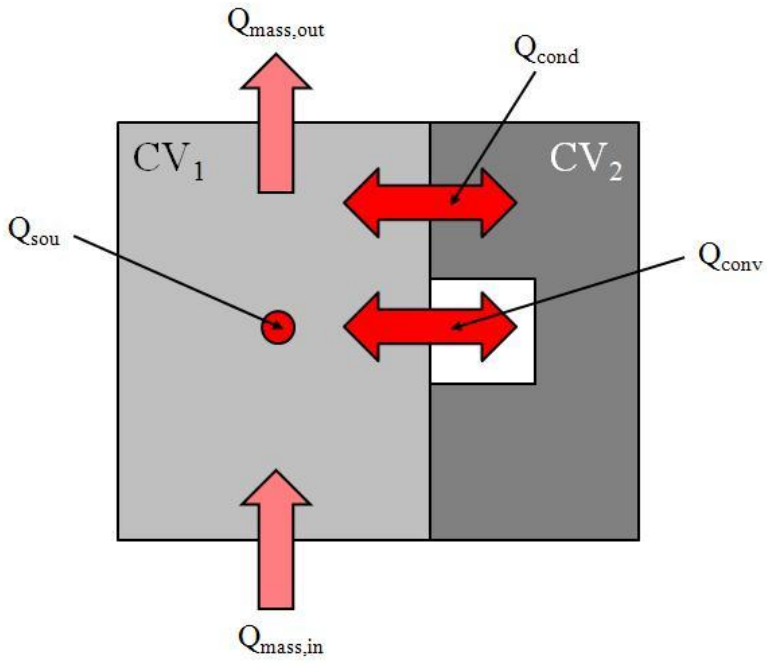

Figure 2-4. Energy balance model.

2.3. Non-isothermal and two-phase dynamic fuel cell model

The proposed model has the following major improvements over models in section 2.2: a) the addition of the temperature distribution though the cell and its effects on components of the fuel cell; b) inclusion of two-phase effects in the GDL and GFC; and c) a coupled 20-cell stack.

The developed model was used to study two-phase effects, the start-up behavior of a 20-cell stack, and transient behavior at a step load.

2.3.1. Two-phase model for GDL

The phase of water in the gas diffusion layer plays a significant role in the transport of water and reactants. The proposed model for the GDL considers mass transport in two-phase flow, and the phase transition between liquid water and water vapor in which the diffusion reflects by introducing an effective diffusivity that describes the diffusion behavior of vapor and liquid water in a capillary [43], [50]. The effective diffusivity $<D_m>$ (m^2 s^{-1}) is a function of the diffusion coefficient at a single phase D_m (m^2 s^{-1}), the porosity of the diffusion layer ε, and the liquid water saturation ratio s between the volume of liquid water and the pores (m^3). Thus,

$$< D_m >= D_m \cdot \varepsilon \cdot \left(\frac{\varepsilon - 0.11}{1 - 0.11} \right)^{0.785} \cdot (1 - s(k))^2 \qquad (2\text{-}27)$$

where k is number of each domain in the GDL.

A setup of one-half of a cell for the GDL on the cathode side is shown in Figure 2-5. To calculate gradients of the species, the GDL was divided into three sub-domains. Points 0 and 4 are the boundary conditions, and points 1, 2, and 3 are the middle points of the sub-domains.

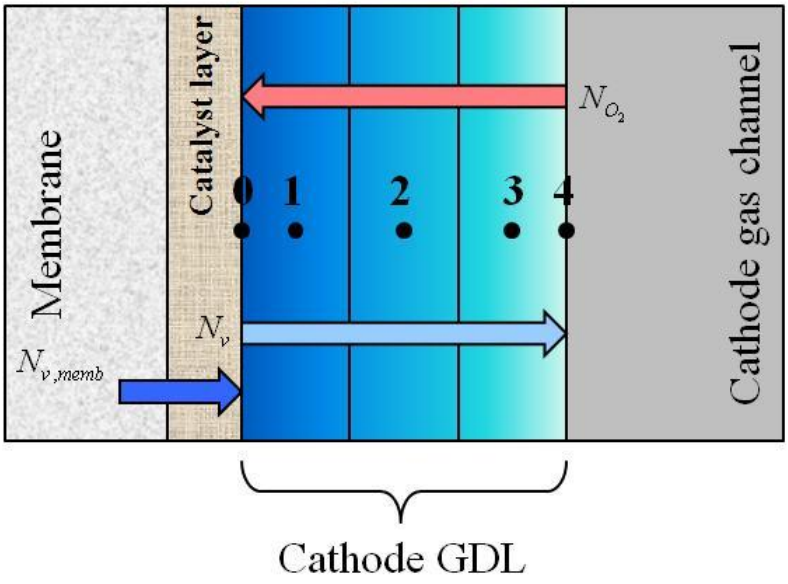

Figure 2-5 Schematic diagram for two-phase GDL.

The water vapor produced $N_{v,0}$ and the oxygen consumed $N_{O2,0}$ are expressed as a function of current. The total flux of water vapor at the boundary is given as follows:

$$N_{v,0} = \frac{I}{2 \cdot F}; \quad N_{O_2,0} = \frac{I}{4 \cdot F} \tag{2- 28}$$

$$N_{v,catl-gdl} = N_{v,0} + N_{v,memb} \tag{2- 29}$$

where $N_{v,memb}$ is the molar flux of water vapor from the membrane to the cathode catalyst.

The molar flux is expressed as a function of the effective diffusivity, the gas concentration gradient, and the ratio of the species molar flux z_{ca}(k):

$$N_{O_2}(k) = \frac{-\langle D_{O_2}(k) \rangle}{1 - x_{O_2}(k) \cdot (1 + z_{ca}(k))} \cdot \frac{c_{O_2}(k+1) - c_{O_2}(k)}{y \cdot t_{gdl}};$$
$$N_v(k) = \frac{-\langle D_v(k) \rangle}{1 - x_v(k) \cdot \left(1 + 1 / z_{ca}(k)\right)} \cdot \frac{c_v(k+1) - c_v(k)}{y \cdot t_{gdl}} \tag{2- 30}$$

where x is the molar ratio of the species and y is a coefficient that depends on the number of the sub-domain. The ratio of species molar flux z_{ca} (k) is given by

$$z_{ca}(k)=\begin{cases}\dfrac{N_{v,0}}{N_{O_2,0}}, & \text{for } k=1\\ \dfrac{N_v(k-1)}{N_{O_2}(k-1)}, & \text{for } k=2 \text{ and } 3\end{cases} \tag{2- 31}$$

The time derivatives of the gas concentrations are a function of the ratio of species molar flux [43]:

$$\begin{aligned}\frac{dc_{O_2}}{dt}(k)&=-\frac{N_{O_2}(k)-N_{O_2}(k-1)}{y\cdot t_{gdl}}\\ \frac{dc_{O_2}}{dt}(k)&=-\frac{N_v(k)-N_v(k-1)}{y\cdot t_{gdl}}+R_{evap}(k)\end{aligned} \tag{2- 32}$$

where R_{evap} is the evaporation rate determined by the difference between the saturation and vapor pressure [43], [50], and is given by

$$R_{evap}(k)=\gamma\cdot\frac{p_{sat}(T(k))-p_v(k)}{R\cdot T(k)} \tag{2- 33}$$

where γ is the volumetric condensation coefficient (s^{-1}), p is pressure (Pa), and R is the ideal gas constant (J mol^{-1} K^{-1}).

Using a mass balance, the rate of the liquid water volume at each of the points was obtained as follows:

$$\frac{dV_{liquid}(k)}{dt}=\begin{cases}-\dfrac{M_v\cdot\varepsilon\cdot V_{GDL}\cdot R_{evap}(k)-W_{liquid}(k)}{\rho_{liquid}} & \text{for } k=1\\ -\dfrac{M_v\cdot\varepsilon\cdot V_{GDL}\cdot R_{evap}(k)+W_{liquid}(k-1)-W_{liquid}(k)}{\rho_{liquid}} & \text{for } k=2 \text{ and } 3\end{cases} \tag{2- 34}$$

where ρ is the density of the liquid water (kg m^{-3}).

The mass flow of the liquid water, W_{liquid}, was derived from the pressure gradient-driven flow in a capillary [43], [50]:

$$W_{liquid}(k) = -\frac{A \cdot \rho_{liquid} \cdot K \cdot K_{rl}}{\mu_{liquid}} \cdot \left|\frac{dp_c}{dS}\right| \cdot \frac{Ss(k+1) - S(k)}{y \cdot t_{GDL}} \quad (2\text{-}35)$$

where K is the absolute permeability (m^2), K_{rl} is the relative permeability of liquid water that is assumed to be equal to S^3, μ is the viscosity of water (kg m^{-1} s^{-1}), $|dp_c/dS|$ is the slope of the capillary pressure (Pa), S is the reduced liquid water saturation, and s_{im} is the immobile saturation.

A summary of the parameters for the GDL model is listed in [47].

2.4. Model for a stack and experimental validation

Multi-cell stack models were developed to analyze cooling effects on the temperature and gas dynamics inside the fuel cell stack, as shown in Figure 2-7.

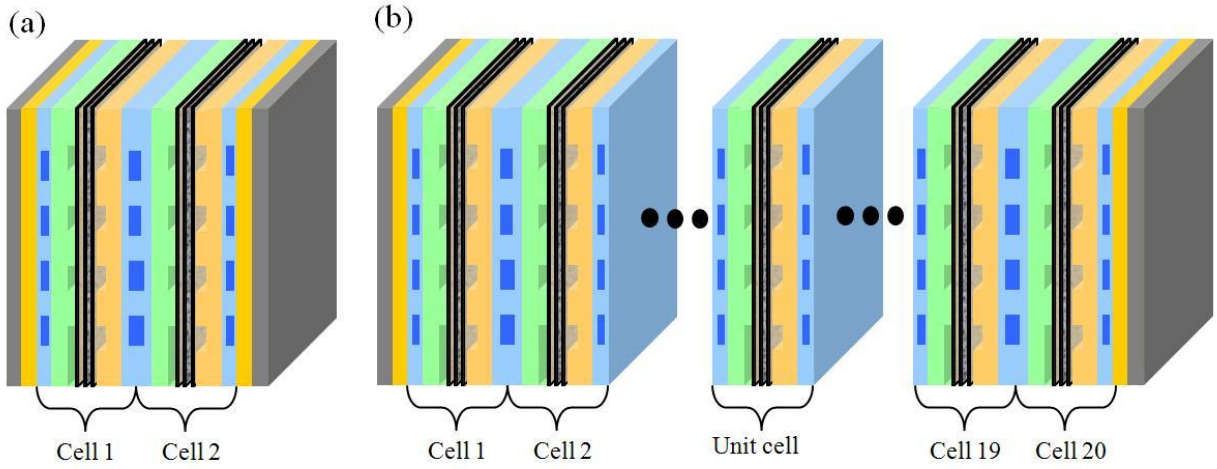

Figure 2-6. Schematic diagrams of (a) 2-cell stack, and (b) 20-cell stack.

An experiment using a 2-cell stack and a 20-cell stack was conducted to validate the developed multi-cell stack model [47]. The experimental apparatus used for validation of the stack model is shown in Figure 2-7. The test setup consists of a two-cell stack and the BOP, which includes an air supply, a humidifier, a hydrogen delivery system, a coolant circuit, controls, and an electronic load. The stack was designed such that two cells were separated by a thermally conductive plate to minimize the potential influence of the coolants on the working temperature. LabVIEW software (ver. 7.1.1., National Instruments Corporation, TX) was used to control valves and actuators for flows and coolants, and to simultaneously collect the process data.

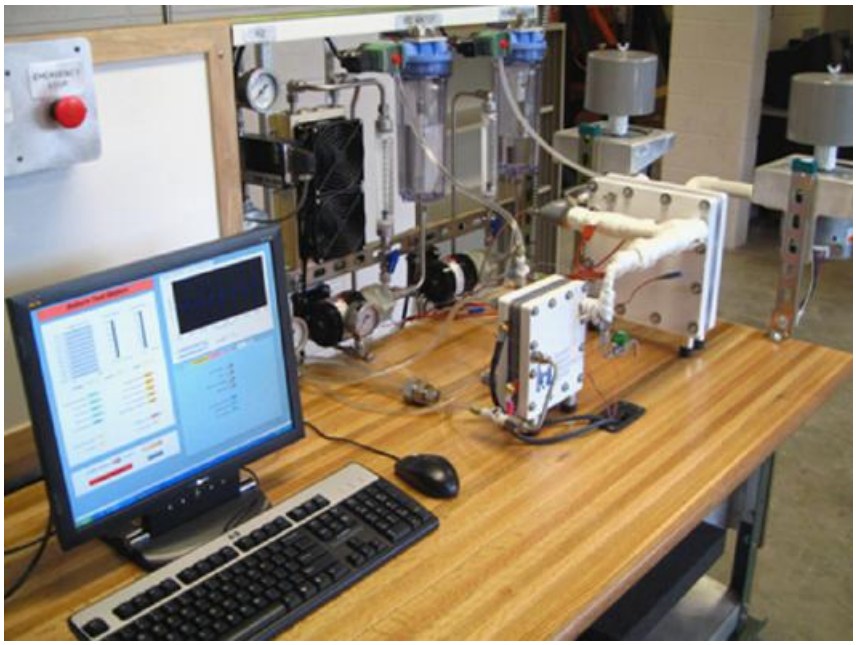

Figure 2-7. Experimental apparatus.

A two-cell stack model was simulated using the developed model. The I-V characteristics calculated for the stack and the individual cells were compared to experimental data collected at the installed test station. The operating conditions were as follows. The stoichiometric ratio was

1.2 for the anode and 3.0 for the cathode. The gas pressure and supply gas temperature on both sides were 1.0 bar and 333.15 K, respectively. The relative humidity for the anode gas was 0% and 100% for the cathode gas. The average temperature of the coolants at the exits of cells 1 and 2 was maintained at 333.15 K by controlling the coolant temperature.

The simulated and experimental stack voltage results were in good agreement, but the deviation of the two cell voltages obtained from the simulation is not as large as that measured experimentally. The reference [47] compared a single-phase and a two-phase model for a 2-cell stack and represented that the differences in the two cells could have been caused by non-uniform characteristics of the individual cells such as reactant distributions, and by the properties of the GDL and the membrane.

2.5. Summary

Several stack models were developed to describe the phenomenon or behavior in the stack. An isothermal and single-phase stack model is used to develop the control for the air supply system. However, Isothermal model does not represent temperature peak in the catalysts and membranes that is usually several degree higher than the average temperature. Therefore, the heat generated cannot optimally rejected by control strategies. Single-phase does not represent losses of potentials caused by mass transports of reactants and water. Thus, static and dynamic characteristics are different than that of two-phase. The model cannot be used for analyzing effects of humidity on the cell performances and associated controls designed in this dissertation. Therefore 1D PEM fuel cell stack model was proposed, used to design the controls for air, water, and thermal management, and validated by experiments.

Chapter 3 Air and Water Management

When a fuel cell operates, oxygen contained in the air is supplied to the fuel cell. Insufficient oxygen supply at abrupt change of loads causes oxygen starvation, which results in cell reversal in the cathode. Reduced hydrogen in the cathode generates heat on the catalysts and results in local hot spots in the membrane electrode assembly (MEA), which could give permanent damage to the fuel cells. On the other hand, an excessive oxygen supply increases the parasitic power dissipated by a blower, which leads to low efficiency of the overall system. Therefore, an oxygen supply should be optimized.

During the operation of the fuel cell, water is produced in the cathode catalyst. Insufficient water in the membrane causes dehydration that decreases proton conductivity and increases voltage loss, which leads to a reduction in output power. However, the water produced by chemical reactions causes flooding in the cathode, which blocks oxygen transport to the catalysts and reduces the catalyst activation areas. As a result, the degradation of components is accelerated. Therefore, water management is required to remove excessive water in the cell, and at the same time to fully humidify the membrane.

3.1. System configurations

The air supply system mainly supplies oxygen by air to the fuel cell stack. A typical configuration of the air supply system [40] consists of a compressor and a blower to produce

pressurized air, inlet and outlet manifolds, and a humidifier that humidifies the entering air, as shown in Figure 3-1.

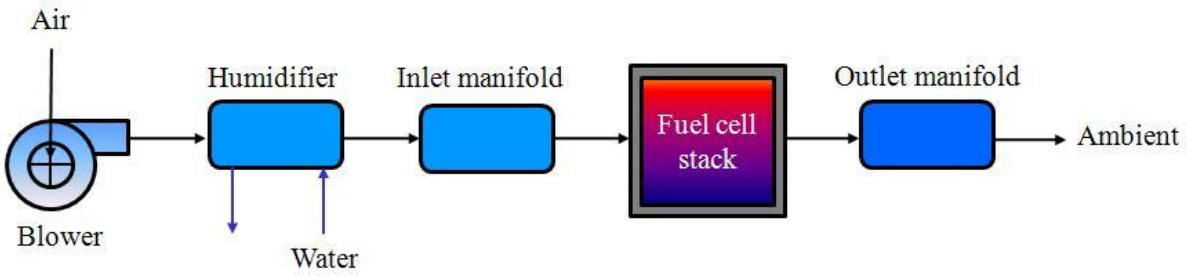

Figure 3-1. Air supply system with humidifier [51].

Since the exhaust gas exiting from the fuel cell stack contains water, a gas-to-gas humidifier is preferred (which does not need an additional water supply system), as shown in Figure 3-2(a). One of the drawbacks of the system is that water flooding may occur in the high current density region because all exhaust gas is fully humidified and flows though the humidifier. In addition, the humidity of the inlet gases cannot be actively manipulated. Thus, a new configuration is proposed that employs an extra three-way bypass valve. This valve diverts the flow of the exhaust gas in the humidifier or free air, as shown in Figure 3-2(b).

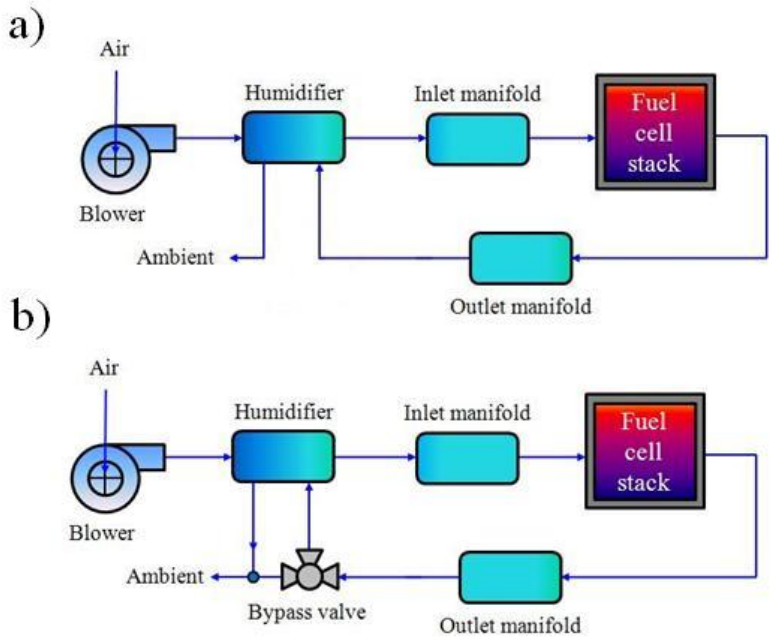

Figure 3-2. Air supply system with gas-to-gas humidifier and three-way valves.

3.2. BOP models

3.2.1. Model for air supplier

A compressor or blower can be used as an air supplier. A blower is generally preferred because of its higher air flow rate compared to that of a compressor. In addition, the parasitic power of a blower is significantly less than that of a compressor in the high net power region [52]. Different types of blowers can be used for this application. One such blower is the axial flow blower, which has blades that force air to move parallel to a shaft with rotating blades

A centrifugal blower uses the centrifugal force generated by a rotating disk with blades mounted at right angles to the disk, as shown in Figure 3-3. It consists of an impeller wheel contained within a blower housing. A centrifugal blower is capable of delivering highly pressurized air in a very small size with good overall efficiency.

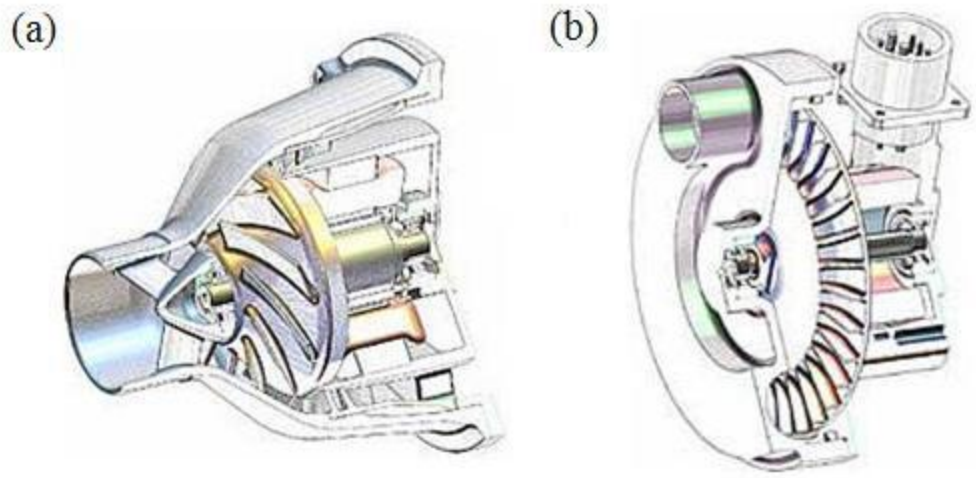

Figure 3-3 Structures of (a) centrifugal blower and (b) regenerative blower [53].

A regenerative blower allows some air passing over a blade of the impeller to slip past it. The air is moved forward by another blade. The structure of the blower is relatively simple, consisting of an impeller with blades. Regenerative blowers operate with high efficiency and are usually relatively compact in size for the large amount of air they move. They produce lower amounts of acoustical noise and vibration than many other types of blowers.

3.2.1.1. Modeling a blower

A blower is operated by a direct current (DC) brushless motor. The dynamic characteristics of the blower system can be described by the sum of all moments of inertia of the motor and the impeller, and the torque produced by the motor. Hence, the torque produced by the motor $\tau_{bl,m}$ (J), is a function of stator resistance $R_{s,bl,m}$ (Ω), flux linkage $\Phi_{bl,m}$ (V s rad^{-1}), the number of poles $n_{bl,m,pl}$, and the stator voltage $V_{bl,m}$ (V):

$$\frac{d\omega_{bl}}{dt} = \frac{1}{J_{bl}}\left(\tau_{bl,m} - \frac{W_{bl}\Delta P_{bl}\eta_{bl,m}}{\eta_{bl}\rho_{amb}\omega_{bl}}\right)$$
$$\tau_{bl,m} = \eta_{bl,m}\frac{3}{2}\left(\frac{n_{bl,m,pl}}{2}\right)\left(\frac{\Phi_{bl,m}}{R_{s,bl,m}}\right)\left[V_{bl,m} - \left(\frac{N_{bl,m,pl}}{2}\right)\Phi_{bl,m}\omega_{bl}\right] \quad (3\text{-}1)$$

where ω is the angular velocity (rad·s^{-1}), J is the rotational inertia (kg·m^2), η is the efficiency, p is the pressure (Pa), and ρ is the air density (kg·m^{-3}). The air blower flow rate is a function of angular velocity and pressure, and the efficiency is a function of flow rate and angular velocity [54]:

$$W_{bl} = \begin{cases} \omega_{bl}\cdot\left(-20.581\cdot\left(p^*\right)^2 - 1.4415\times10^{-3}\cdot p^* + 4.1333\times10^{-5}\right) & for\ p^* \le 9\times10^{-4} \\ \omega_{bl}\cdot\left(-1.7973\cdot p^* + 1.6409\times10^{-3}\right) & for\ p^* > 9\times10^{-4} \end{cases} \quad (3\text{-}2)$$

$$\eta_{bl} = -2.8831\times10^{13}\cdot\left(\frac{W_{bl}}{\omega_{bl}}\right)^3 + 9.5115\times10^{8}\cdot\left(\frac{W_{bl}}{\omega_{bl}}\right)^2 + 1.3087\times10^{4}\cdot\left(\frac{W_{bl}}{\omega_{bl}}\right) + 0.17945 \quad (3\text{-}3)$$

where p^* (Pa s^2 rad^{-2}) is $\left(\frac{p_{tube} - p_{amb}}{\omega_{bl}^2}\right)$.

The parameters for the blower were derived using characteristic data and specifications provided by Phoenix Analysis & Design Technologies (PADT) [53], and include both the flow parameter and the overall efficiency versus head parameter. A block diagram of the blower model is shown in Figure 3-4.

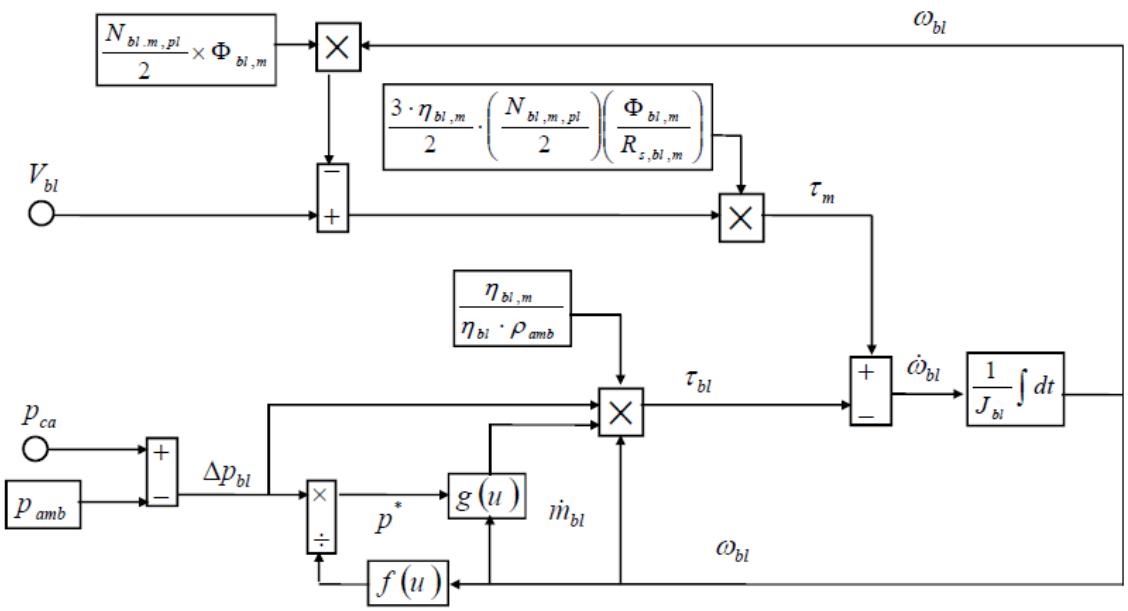

Figure 3-4. Block diagram of the blower model.

3.2.2. Model for humidifier

Different types of humidifiers can be used for this application. One is the bubble-type humidifier [55]. A bubble-type humidifier consists of air that is bubbled into a container of water and becomes saturated when it leaves the container. Although a very high dew point can be achieved at low flow rates, the effectiveness of humidification rapidly decreases at higher flow rates. In addition, the humidity cannot be controlled, and a water reservoir is needed.

The enthalpy wheel is another choice. An enthalpy wheel seeks to absorb moisture from the air exiting the fuel cell and transfer it to the relatively dry air entering the fuel cell [56]. As shown in Figure 3-5(a), the device employs an electric motor to turn the housing of a desiccant capable of absorbing and distributing humidity in the presence of vapor gradients. This device has good operation and a compact design. The reactant gases should be preheated, and a motor is required to turn the wheel to exchange vapor and heat.

A membrane humidifier can be classified into three types: a plate-type humidifier, a liquid-to-gas membrane humidifier, and a gas-to-gas humidifier. The plate-type humidifier consists of sandwiched membranes that contain flow channels for humid and dry air streams. This type of humidifier contains sliding plates that can be used to control the heat and humidity flowing into the fuel cell. The sliding plates block one of the flow channels and transfers heat and water from one channel to another channel, as shown in Figure 3-5(b). This device has the advantage of no moving parts (except the sliding plates), and no associated energy.

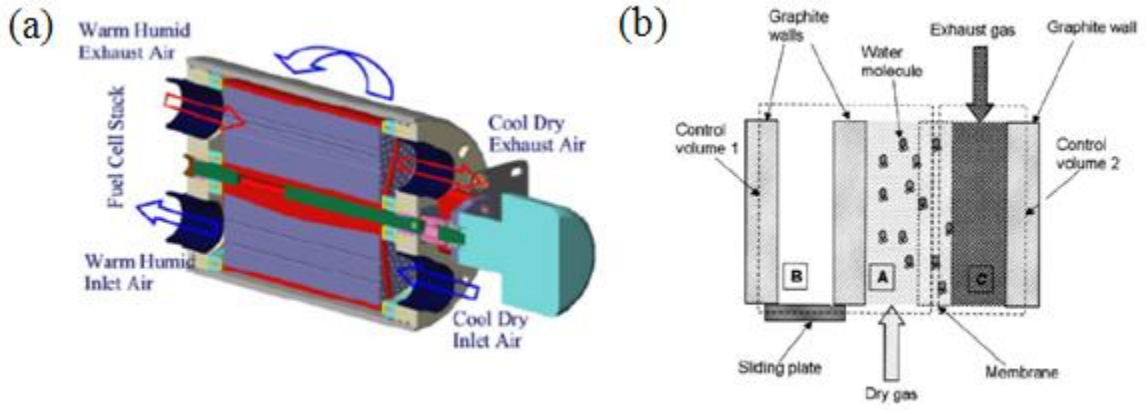

Figure 3-5. Diagram of (a) an enthalpy wheel [56], and (b) a plate-type humidifier [57].

A liquid-to-gas humidifier contains a membrane that separates the flow of liquid and gas. The liquid water humidifies the dry gas that enters the fuel cell. This type of humidifier is capable of humidifying dry gas to near saturation at high flow rates. However, the humidifier needs a reservoir and a pump to circulate water on one side of the membrane; therefore, the device is heavy. In addition, it is difficult to prevent leakage in this type of humidifier.

A gas-to-gas humidifier does not have the drawbacks of the liquid-to-gas humidifier. The advantages of the gas-to-gas humidifier are no moving parts and no additional energy input.

When the reaction starts in the fuel cell, the generated heat is contained in the exhaust gases entering the shell side of the humidifier. Then, the dry air flowing into the fuel cell is heated and humidified though the tube side of the humidifier. This gas-to-gas humidifier is considered to be the most efficient way to humidify a fuel cell. In addition, this type of humidifier can provide heat for the fuel cell stack at subzero conditions.

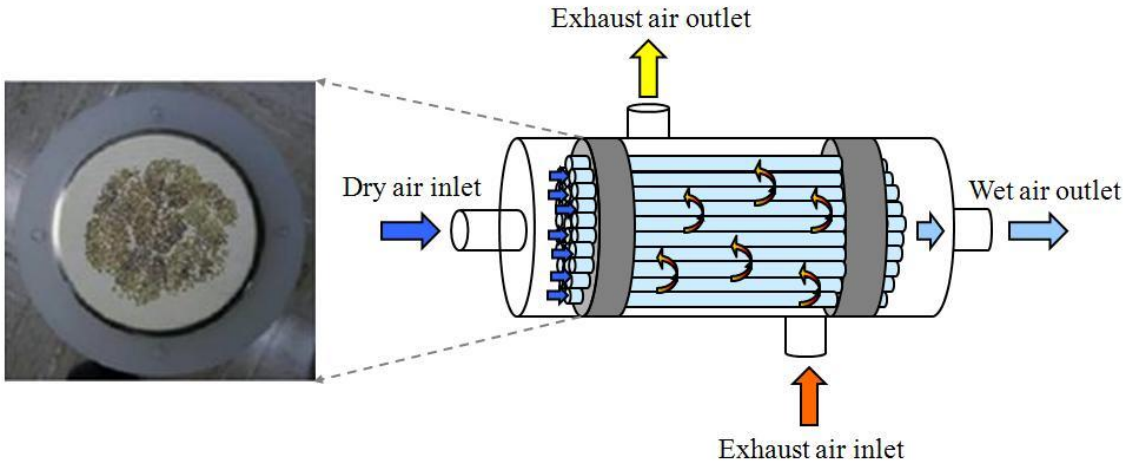

Figure 3-6. Structure of a gas-to-gas humidifier [58].

3.2.2.1. Humidifier model

The principle of a gas-to-gas humidifier is shown in Figure 3-7.

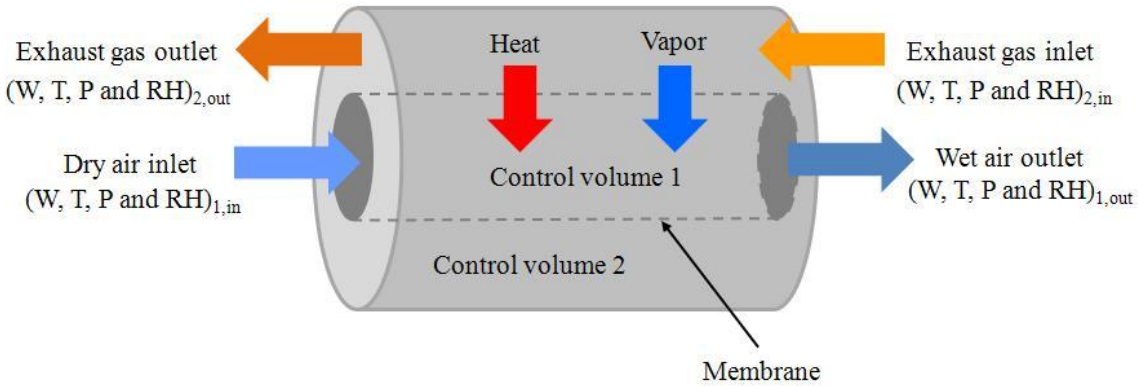

Figure 3-7. Principle of a gas-to-gas humidifier

Since a shell-and-tube humidifier is used to transport water from exhaust gases on the shell side to dry gases on the tube side, there is no mass change of oxygen or nitrogen through the tube and the shell. Therefore, the dynamic equations representing the humidifier are

$$\begin{aligned} \frac{dp_{i,air}}{dt} &= \frac{R_{air} \cdot T_i}{V_i} \cdot \left(W_{air,i,in} - W_{air,i,out} \right) \\ \frac{da_{w,i}}{dt} &= \frac{1}{p_{sat}(T_i)} \cdot \frac{R_{H_2O} \cdot T_i}{V_i} \cdot \left(W_{w,i,in} - W_{w,i,in} + W_{w,trans} \right) \end{aligned} \tag{3- 4}$$

where *i* denotes a tube or a shell.

Vapor transfer within the humidifier is a result of concentration gradients within the membrane material. Therefore, the amount of vapor transfer exhibited under a specific flow condition is dependent on the humidity difference between the tube side and the relatively humid shell side. The amount of vapor mass transferred during the operation from the annulus to the tube is given by

$$W_{w,trans} = D_w \cdot \left(\frac{C_{shell} - C_{tube}}{t_{mem}} \right) \cdot m_v \cdot A \tag{3- 5}$$

where *C* denotes the water mass concentrations in each channel, and *t* is the thickness of the membrane under the proposed single tube representation.

Heat transfer behavior is governed by an energy equation with coefficients representing tubular geometry. The heat transfer rate across the membrane is given as

$$\frac{dQ_i}{dt} = U \cdot A \cdot \Delta T \tag{3- 6}$$

where *i* denotes a tube or a shell, *U* is the overall heat transfer coefficient (W m^{-2} K^{-1}), which is a function of the convective heat transfer coefficients of the air, *h.* We have

$$\frac{1}{U \cdot A} = \frac{1}{h_{tube} \cdot A_{inner}} + \frac{\ln\left(D_{outer} / D_{inner}\right)}{2\pi \cdot L \cdot k_{memb}} + \frac{1}{h_{shell} \cdot A_{outer}} \tag{3- 7}$$

where h is a function of thermal conductivity k and the Nusselt number Nu, and Nu is an empirical function depending on the direction of the flow:

$$h_i = Nu_i \frac{k_i}{D_i}, (i = \text{tubeside, shellside}) \tag{3- 8}$$

3.2.3. Model for inlet and outlet manifolds

Since no heat changes in the manifolds are assumed, the dynamic characteristics of the inlet and outlet manifold pressures can be described using the ideal gas law and the mass conservation equation:

$$\frac{dp_i}{dt} = \frac{R_a \cdot T_i}{V_i} \cdot \left(W_{i,in} - W_{i,out}\right) \tag{3- 9}$$

where i denotes the inlet or outlet manifolds.

3.2.4. Model for a bypass valve

The bypass valve allows exhaust gas to flow from the stack to the bypass, or to flow into a humidifier. When the opening of a bypass valve can be assumed to be linear with a factor k, the exhaust gas flow entering the shell side of the humidifier is the product of the exhaust gas flow at stack outlet $W_{st,ex,out}$ (kg s^{-1}) and the opening factor of a bypass valve k:

$$\begin{aligned} W_{st,ex,out} &= W_{shell,ex,in} + W_{ex,bypass} \\ W_{shell,ex,in} &= k \cdot W_{st,ex,out} \end{aligned} \tag{3- 10}$$

3.3. Control strategies

3.3.1. Air

When a load current is suddenly applied, the oxygen consumption increases. Thus, the oxygen partial pressure will drop, which causes a depletion of the oxygen on the cathode side and potentially damages the catalyst on the cathode side [7]. Therefore, the air supply system must continuously replenish oxygen by supplying air to the cathode, which allows the stack to follow the current command as quickly as possible. For better judgment of the dynamic oxygen supply, an oxygen excessive ratio is introduced as a new variable that defines the ratio of the oxygen supplied and consumed. The air supplied by the blower is controlled to keep the oxygen excess ratio λ_{O2} at the desired level.

A block diagram of an air supply system using a blower is shown in Figure 3-8.

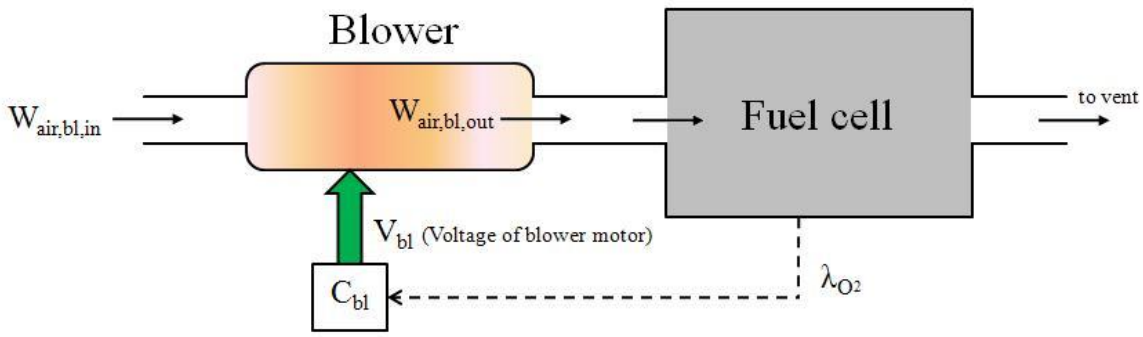

Figure 3-8. Air supply system using a blower.

The control objectives of the air supply system are to maintain the desired oxygen ratio and to prevent oxygen starvation that might occur during abrupt changes in the load current. To

design the controls, we first assumed that operating temperature is 343 K and the air supplied to the fuel cell is fully humidified.

Figure 3-9 shows two control configurations for the air supply system: a static feed-forward controller (sFF), and a feedback controller with a state feedback controller and a static feed-forward controller (sFB). The current is the reference input for the system.

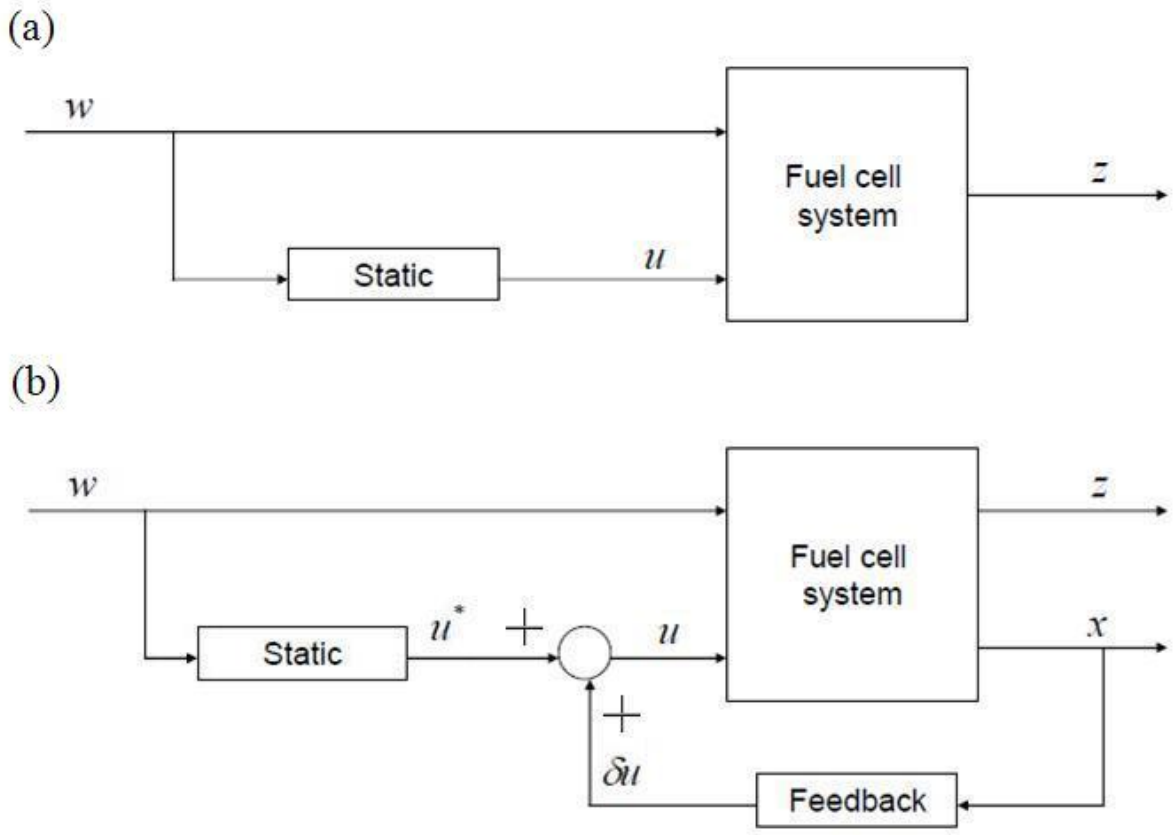

Figure 3-9. Control configurations of (a) a sFF, and (b) a sFB with a sFF.

The sFF control uses the reference current to calculate the flow rate of the fuels, which represents open loop control. An optimal blower motor voltage is calculated based on a given reference current, which maintains the desired oxygen excess ratio at 2.0. The set point of 2.0

was determined to avoid oxygen starvation and minimize the parasitic power of the blower during operation. This relationship is shown in Figure 3-10.

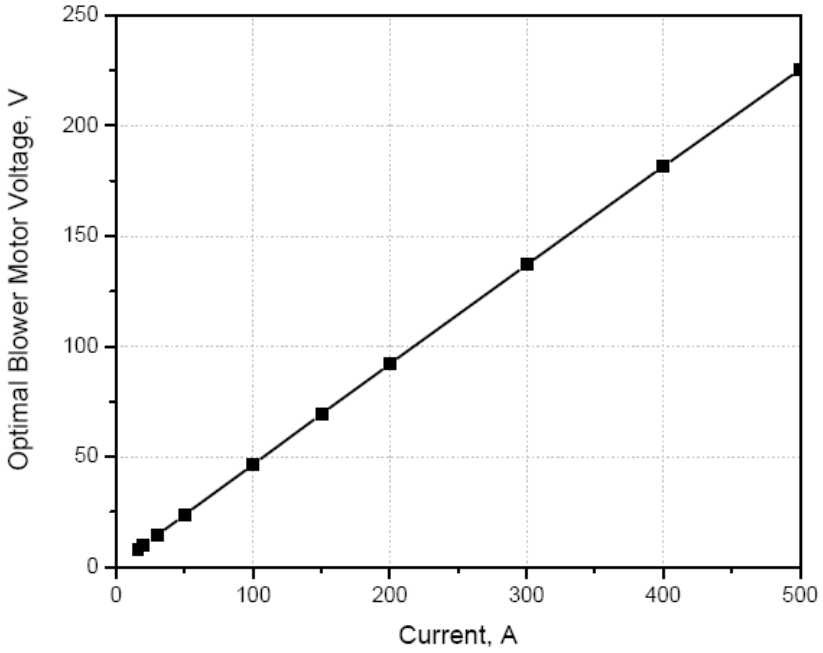

Figure 3-10. Optimal blower motor voltage for static feed-forward controller.

Even though the sFF shows an excellent dynamic response in rejection of the disturbance, the sFF has a steady state error. Conversely, state feedback (sFB) control with an integral control employs a closed loop control that removes the error completely. Figure 3-11 shows a block diagram of sFB. When the stack current as the disturbance w applies to the fuel cell system, the controlled input u is determined by the sFF that is a function of the stack current I_{st}. In addition, the errors of the reference values for the air flow rate and the state variables are amplified by a feedback controller, and then added to the blow voltage given by the sFF and the steady state error is removed by the integral controller. The controllers regulate the performance variables z_2: the oxygen excess ratio λ_{O2}.

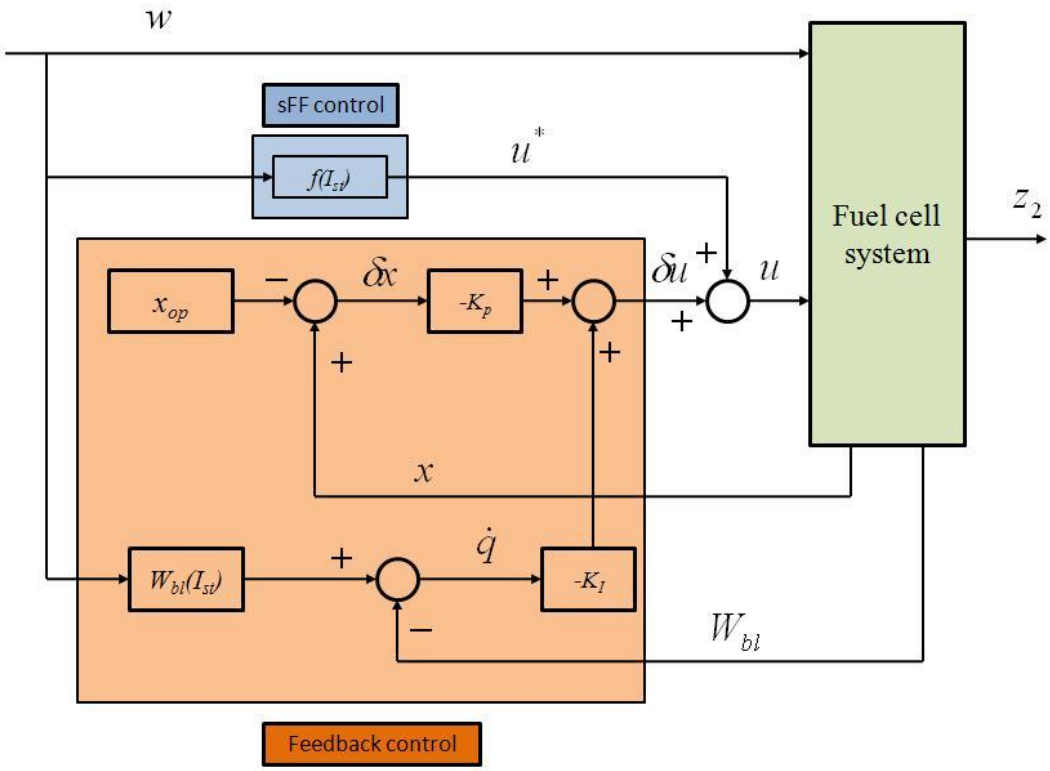

Figure 3-11. Block diagram for feedback control with a feed-forward control.

The design of the sFB is based on the state variable equation. Since the fuel cell system is nonlinear, the system is linearized to obtain the state equation. The operating point is set as follows: a maximal net power, p_{net}^{max} = 68 kW; an oxygen excess ratio, λ_{O2}^{opt} = 2; the stack current, $w^0 = I_{st}$ = 258 A; and the blower motor voltage, $u^0 = V_{bl}^{opt}$ = 118 V.

A general form of the linearized state variable equations can be expressed as

$$\begin{aligned} \delta\dot{x} &= A \cdot \delta x + B_u \cdot \delta u + B_w \cdot \delta w \\ \delta z &= C_z \cdot \delta x + D_{zu} \cdot \delta u + D_{zw} \cdot \delta w \\ \delta y &= C_y \cdot \delta x + D_{yu} \cdot \delta u + D_{yw} \cdot \delta w \end{aligned} \qquad (3\text{-}11)$$

where δ denotes the derivative operator at an operating point, and the variables of the fuel cell system can be defined as follows:

$$x = \left[m_{O_2}, \quad m_{H_2}, \quad m_{N_2}, \quad \omega_{cp}, \quad p_{ca,in}, \quad m_{sm}, \quad m_{w,an}, \quad p_{sm} \right] \qquad \text{(States)}$$

$$u = V_{bl} \qquad \text{(Control variable)}$$

$$w = I_{st} \qquad \text{(Disturbance)}$$

$$y = \left[W_{bl}, \quad P_{im}, \quad V_{st} \right] \qquad \text{(Output)}$$

$$z = \left[P_{net}, \quad \lambda_{O_2} \right] \qquad \text{(Performance variables)}$$

The matrix values of the linearized system, including A, B_u, B_w, C_z, D_{zu}, D_{zw}, C_y, D_{yu}, and D_{yw}, are listed in Appendix A. The units of states and outputs were rescaled for a comparison: mass in grams, pressure in bar, rotational speed in kRPM, mass flow rate in grams per second, power in kilowatts, voltage in volts, and current in amps.

The linear quadratic method (LQR) presented in Appendix B was used to obtain optimal gains for the state feedback controller with an integral controller. The weighting factor Q_I only affects the integrator gain. When Q_I increases, its influence on the cost function increases, which leads to a large value of δz_2. Consequently, the dynamic response of the recovery behavior of the oxygen excess ratio increases and reaches steady state with an overshoot. Figure 3-12 shows the dynamic response of δz_2 for different weighting factors Q_I. In contrast, the weighting factor Q_z hardly improves the transition behavior, which can be seen in Figure 3-13.

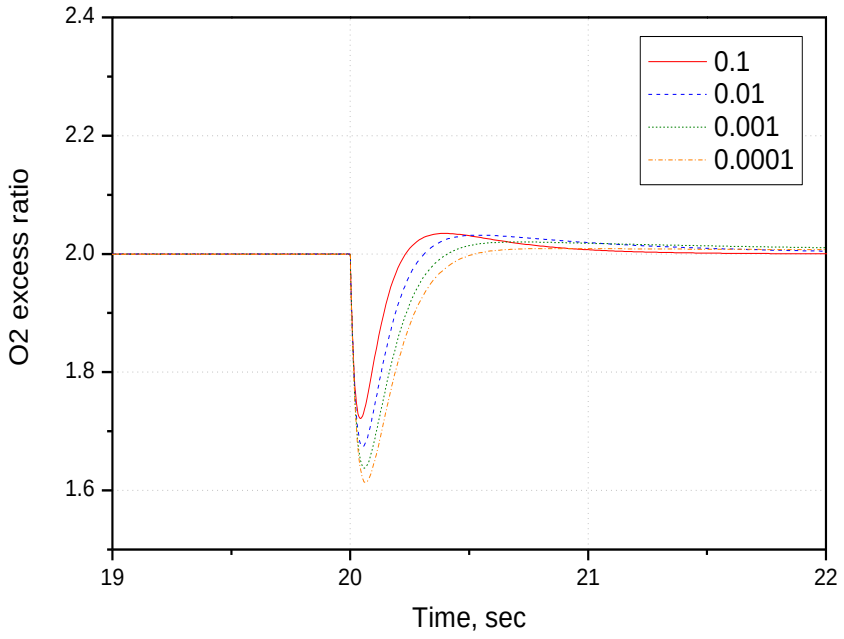

Figure 3-12. Effect of weighting factor Q_I on the recovery behavior of oxygen excess.

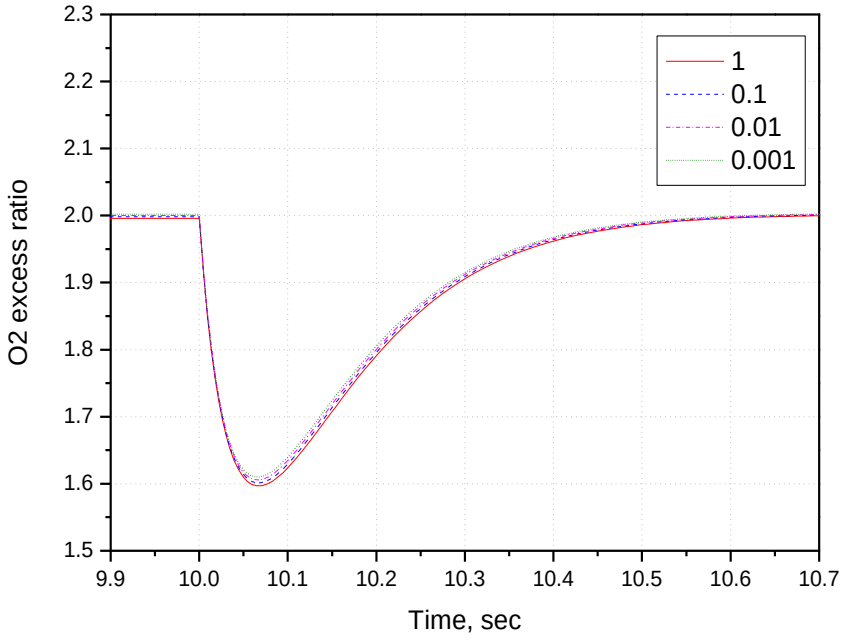

Figure 3-13. Effect of weighting factor Q_z on the oxygen excess ratio.

The optimum values of the determined weighting factors are $Q_z = 1$ and $Q_I = 0.01$. The gains for the PI controller were obtained accordingly, and the second and the seventh state variables are zeros. Both variables are related to the mass of the hydrogen and water on the anode side, which were assumed to have been proportionally delivered.

$$K_p = \begin{bmatrix} -1.1060 \times 10^5 & 0 & -1.2636 \times 10^5 & 20.717 & 2.7681 \times 10^3 & -0.0019 & 0 & 33.5587 \end{bmatrix}$$
$$K_I = -3.1623 \quad \text{(3- 12)}$$

3.3.2. Air and water management (AWM)

As a matter of fact, the air supply system is coupled with the water management. Thus, the control objectives for a blower with a humidifier are to maintain the desired level of membrane water content to prevent membrane dehydration and water flooding in the cathode, in addition to the objectives of the blower given in Section 3.3.1. Three assumptions were made in the design of the controls: the operating temperature is 343 K, dry hydrogen is supplied to the anode, and the exhaust gas temperature is the same as that of the working temperature in the cell.

A block diagram of the air and water management system, including the gas-to-gas humidifier with a state feedback controller, is shown in Figure 3-14. When the load current applies to the fuel cell stack, the blower and the bypass valve operates to control the flow rate and the relative humidity of the air supplied to the stack, respectively. The controlled inputs such as the blower motor voltage V_{bl} and the bypass valve opening factor k_{bp} are determined by the static feed-forward controller that is a function of the load current I_{ref}, and the state feedback controller. The controller regulates the performance variables z: the oxygen excess ratio λ_{O2} and the membrane water content λ_{memb}.

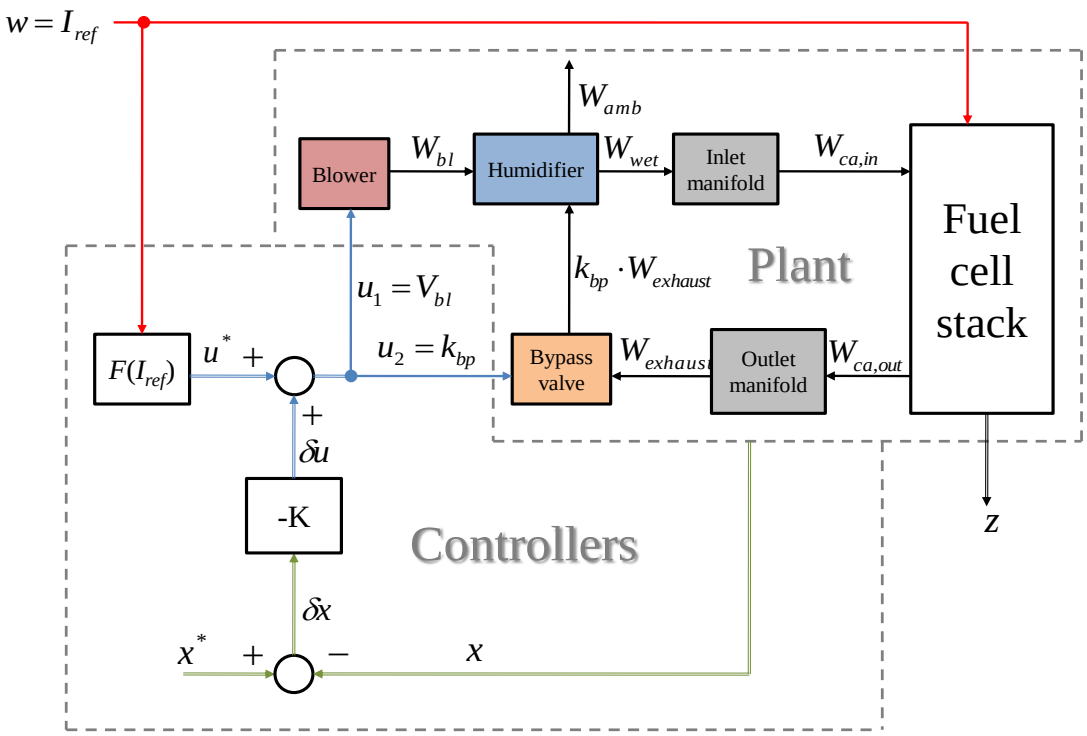

Figure 3-14. Block diagram for control of the air flow rate with a humidifier.

The terminal voltage drops due to the presence of liquid water, particularly when the current increases, and the effects of concentration over-potential increase. Therefore, the design of the controls was approached using two divided regions: a single-phase region and a two-phase region. The design of the controls is shown in Figure 3-15. The operating conditions for the single- and two-phase regions are dependent on current density ranges of 0 to 0.3 (A cm^{-2}) and greater than 0.3 (A cm^{-2}), respectively.

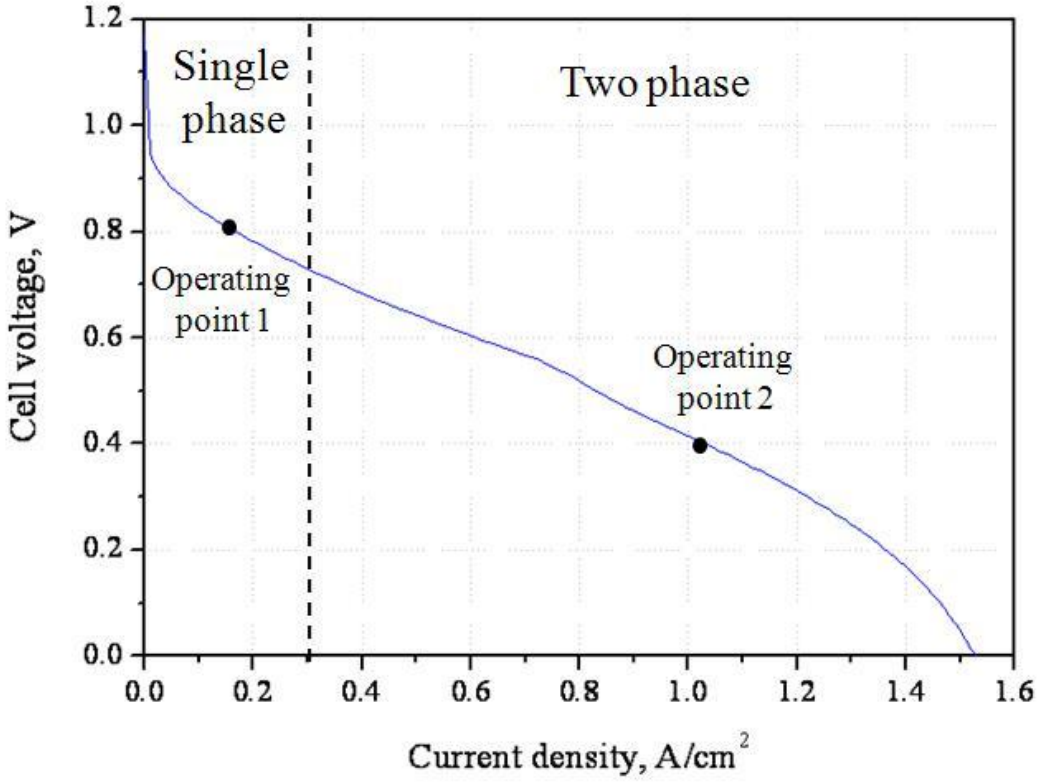

Figure 3-15. Control configuration of air and water management system.

Similar to the design of the air flow rate described in Section 3.3.1, the fuel cell system was linearized using a Taylor expansion at the operating points, i_{st} = 0.1 A cm^{-2} for the single-phase region and 1.0 A cm^{-2} for the two-phase region. For the single-phase region, the integrated system of the AWM with the fuel cell stack can be written as Eq. (3-11). The variables are defined as follows:

$$x = \begin{bmatrix} \omega_{bl} & p_{tube} & a_{w,tube} & p_{im} & p_{ca} & a_{w,ca} & a_{w,an} & p_{om} & p_{shell} & a_{w,shell} \end{bmatrix} \quad \text{(States)}$$

$$u = \begin{bmatrix} V_{bl} & k_{bp} \end{bmatrix} \quad \text{(Control variable)}$$

$$w = I_{st} \quad \text{(Disturbance)}$$

$$y = \begin{bmatrix} \omega_{bl} & p_{tube} & p_{im} & p_{ca} & p_{om} & p_{shell} \end{bmatrix} \quad \text{(Output)}$$

$$z = \begin{bmatrix} \lambda_{O_2} & \lambda_{memb} \end{bmatrix}$$ (Performance variables)

From the simulation results at the operating point, 1.0 A cm^{-2}, the water activities in the cathode and the shell side of the humidifier are 1.0. Thus, the dynamics of water activities in two control volumes can be neglected in the controller design for the two-phase region. The state vector becomes:

$$x = \begin{bmatrix} \omega_{bl} & p_{tube} & a_{w,tube} & p_{im} & p_{ca} & a_{w,an} & p_{om} & p_{shell} \end{bmatrix}$$ (States)

Similar to the air supply system, optimization of the feedback gains was performed using the LQR method. Since an integrator was used to suppress any steady state errors, a new state variable was considered in the cost function:

$$\dot{q} = W_{bl}^{o} - W_{bl} \quad (3\text{- }13)$$

After several iterations with different weighting factors, the optimal control matrices K_p and K_I for the single-phase region were found to be

$$K_{p,s} = \begin{bmatrix} 16.25 & -1.736\times10^{3} & 0 & -9.45\times10^{3} & 7.1854\times10^{3} & 0 & 0 & -1.97\times10^{3} & 5.573\times10^{3} & 0 \\ 2.64 & 6.38\times10^{3} & 2.8 & -8.52\times10^{3} & 1.28\times10^{3} & 1.643 & 0.14 & 8.36\times10^{3} & 5.4\times10^{2} & 14.3 \end{bmatrix} \quad (3\text{- }14)$$

$$K_{I,s} = \begin{bmatrix} -2.418 \\ 0 \end{bmatrix} \quad (3\text{- }15)$$

And the optimal control matrices K_p and K_I for the two-phase region were found to be

$$K_{p,t} = \begin{bmatrix} 25.48 & -4.872\times10^{3} & 0 & -2.85\times10^{4} & 8.152\times10^{3} & 0 & -4.67\times10^{3} & 7.671\times10^{3} \\ 6.284 & 2.876\times10^{3} & 9.234 & -9.167\times10^{3} & 5.252\times10^{3} & 0.31 & 2.865\times10^{3} & 6.326\times10^{-3} \end{bmatrix} \quad (3\text{- }16)$$

$$K_{I,t} = \begin{bmatrix} -1.067 \\ 0 \end{bmatrix} \quad (3\text{- }17)$$

3.4. Simulation and analysis

An integrated system with all components and the fuel cell are shown in Figure 3-16. The whole system has ten state variables. There are two input variables connected to the controller: the voltage of the blower motor V_{bl}, and the bypass opening factor k.

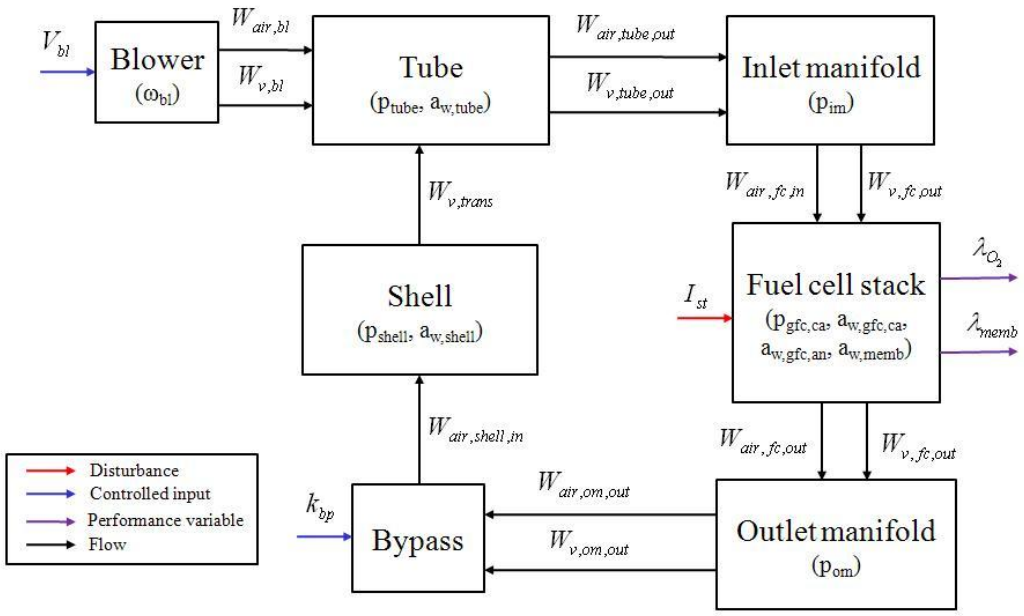

Figure 3-16. Block diagram of the proposed integrated system model.

Simulations were performed to analyze the static and dynamic behavior of the stack along with the air and water management system and their associated controllers. The parameters and reference data for the models chosen are given in Table 3-1.

Fuel Cell			Proton Conducting Model	
n	381		b_{11}	0.5139
A_{fc}	0.025	m^2	b_{12}	0.326
Electrochemical Reation Model			b_2	350
P_0	1.0	bar	n_d	$f(C_{water})$
T_{ref}	353.15	K	D_w	$f(T, C_{water})$
E_{ref}	1.229	V		
$A_{catl,eff}/A_{cell}$	$f(I, T, P_{o2})$			

Geometrical data for layers				
	Thickness	Density	Heat conductivity	Specific heat
	m	$W\ m^{-1}K^{-1}$	$J\ kg^{-1}K^{-1}$	$kg\ m^{-3}$
Coolant Channel	0.001	1400	30	935
Plate	0.001	1400	52	935
Gas Channel	0.001	1400	52	935
Catalyst layer	0.000065	387	0.2	770
Membrane layer	0.000183	1967	0.21	1100

Table 3-1. Parameters of fuel cell model.

3.4.1. Oxygen excess ratio

Two analyses were performed to assess the performance of the designed controllers. The response of the oxygen access ratio at a multi-step current for two different control strategies is shown in Figure 3-17. The sFBI controller can reject the disturbance better than sFF, for which the recovery time for the oxygen excess ratio is short. The recovery time reached 0.37 sec. In addition, the sFBI decreased the oxygen excess ratio drop compared to that of sFF control. The sFBI controller performed more effectively and maintained the optimal oxygen excess ratio more efficiently than the sFF.

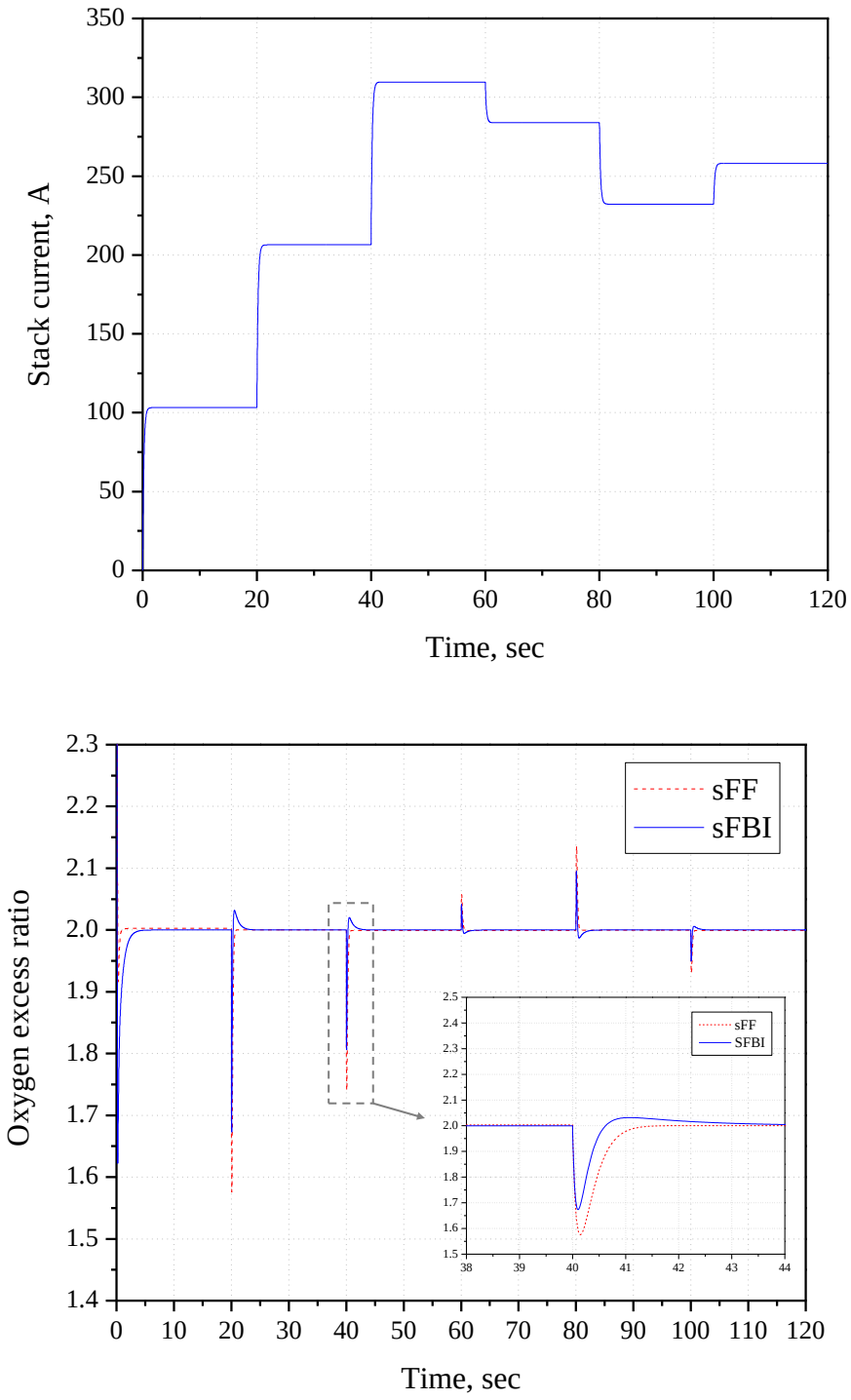

Figure 3-17. Simulated oxygen excess ratio for two different controllers.

3.4.2. Membrane water content and cell voltage

When a constant current of 0.2 A cm^{-2} was applied for 120 sec, membrane water content without humidification kept decreasing as shown in Figure 3-18. This indicates that the amount of water generated in a cell was not sufficient to humidify the membrane without the use of external humidification. On the other hand, controlled humidification maintained the membrane water content at 9.21, which suggests that the membrane was fully humidified at 70 ^{o}C. Decreasing membrane water content leads ohmic over-potential to increase, which results in decreasing cell voltage as shown in Figure 3-18 (b).

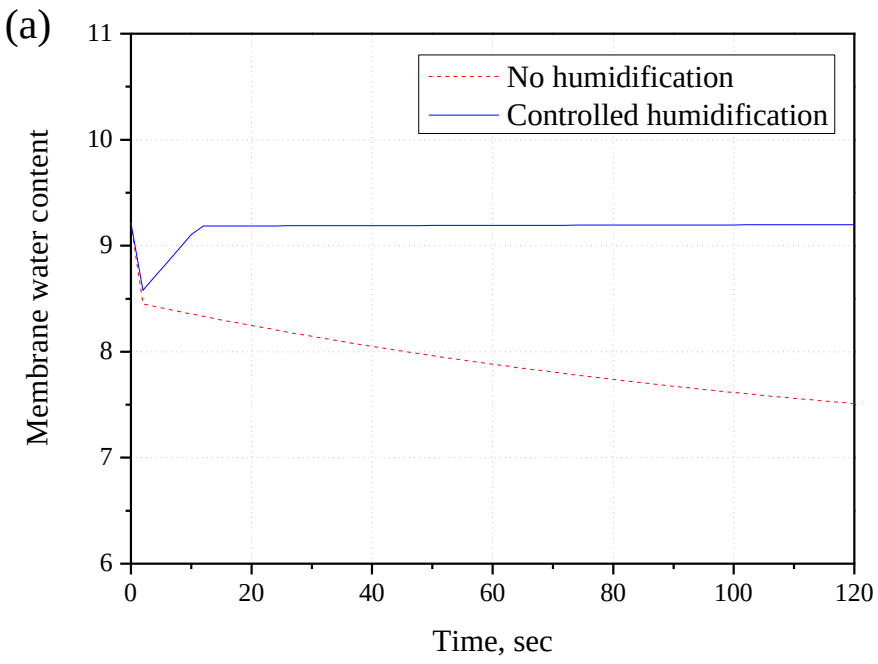

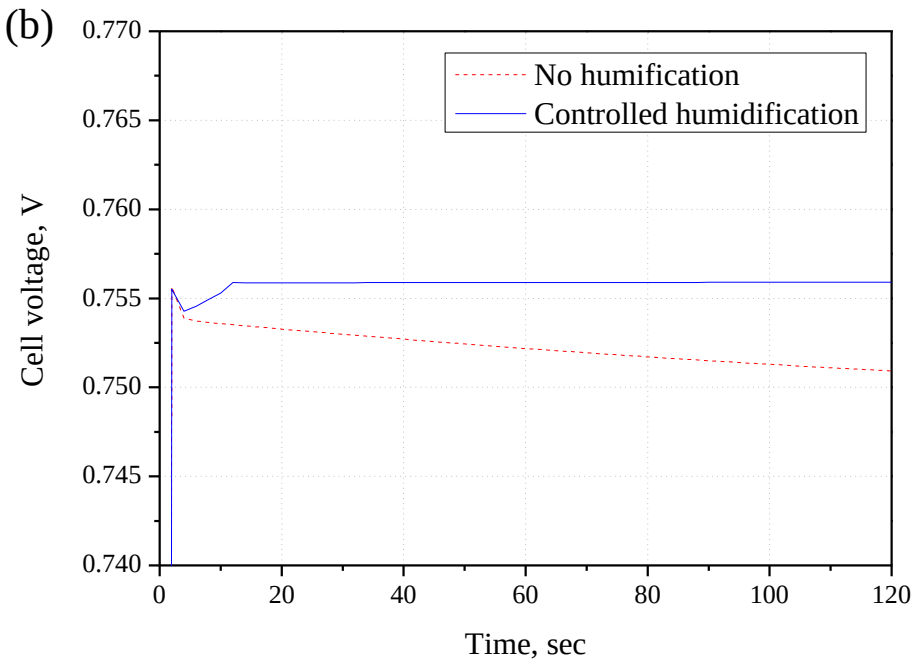

Figure 3-18. Comparison of (a) membrane water content and (b) cell voltages at 0.2 A cm^{-2}.

At a high current density of 1.0 A cm^{-2}, the fuel cell requires external humidification. Therefore, fuel cell systems using uncontrolled and controlled humidification were simulated and compared. While uncontrolled humidification keeps the relative humidity of the stack inlet air at 1.0, controlled humidification regulated the relative humidity of stack inlet air to maintain full humidification of the membrane. As a result, Controlled humidification maintained the level of the membrane water content at 9.21. On the other hand, membrane water content with uncontrolled humidification was higher than the desired level, which indicates that water flooding occurred. As time goes on, water flooding becomes severe, which results in decreasing cell voltage as shown in Figure 3-19 (b).

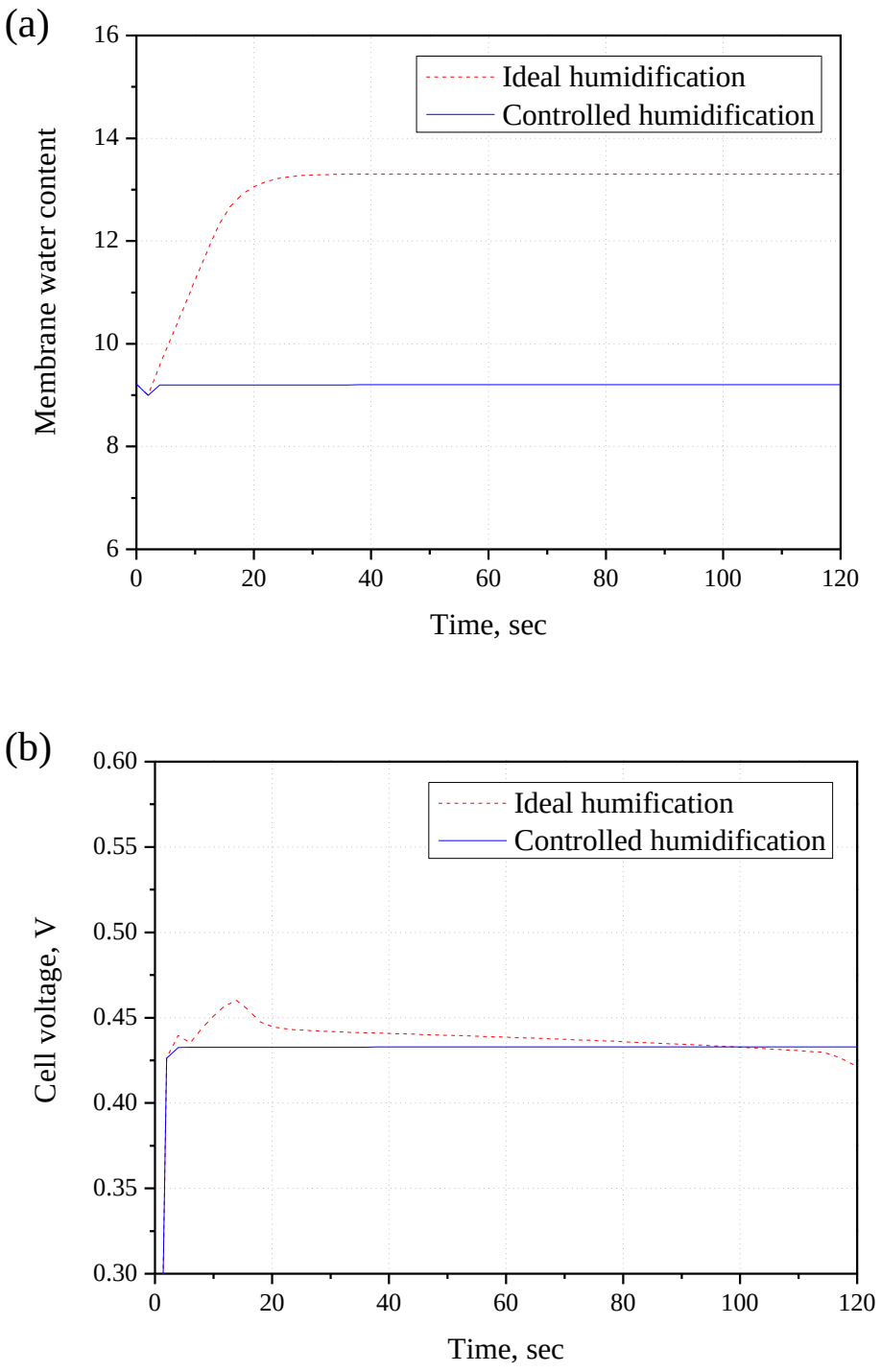

Figure 3-19. Comparison of (a) membrane water content and (b) cell voltages at 1.0 A cm^{-2}.

When the step current profile shown in Figure 3-20 was applied, the uncontrolled humidification did not maintain the membrane water content at 9.21. For 60 sec, the membrane water content increased until it reached at 15.5. The membrane water content at 1.0 A cm^{-1} was less than that at 0.2 A cm^{-1} because the chemical reaction rate at the high current density was reduced due to severe water flooding. This resulted in less water generation. Unlike uncontrolled humidification, controlled humidification regulated the membrane water content at 9.21.

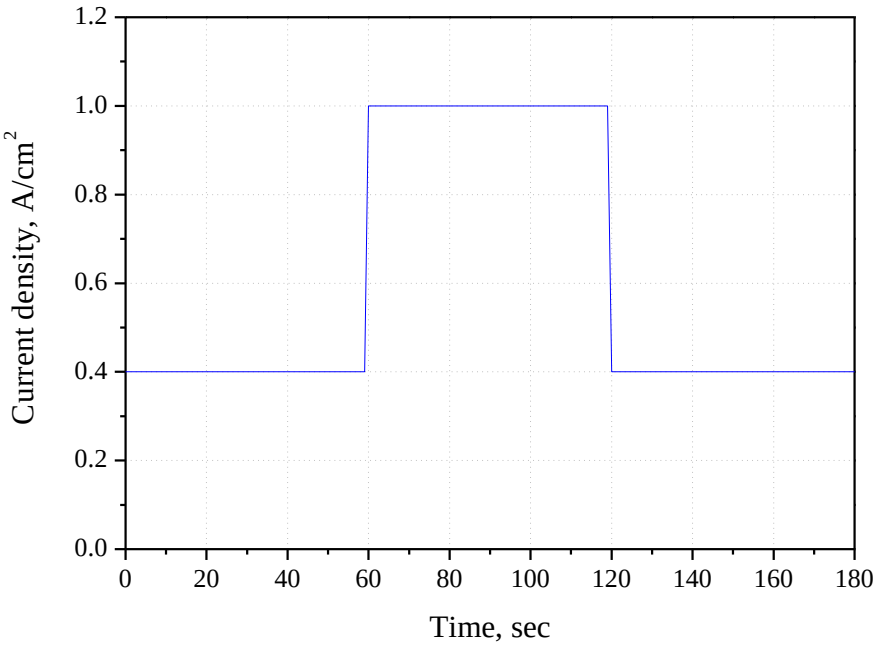

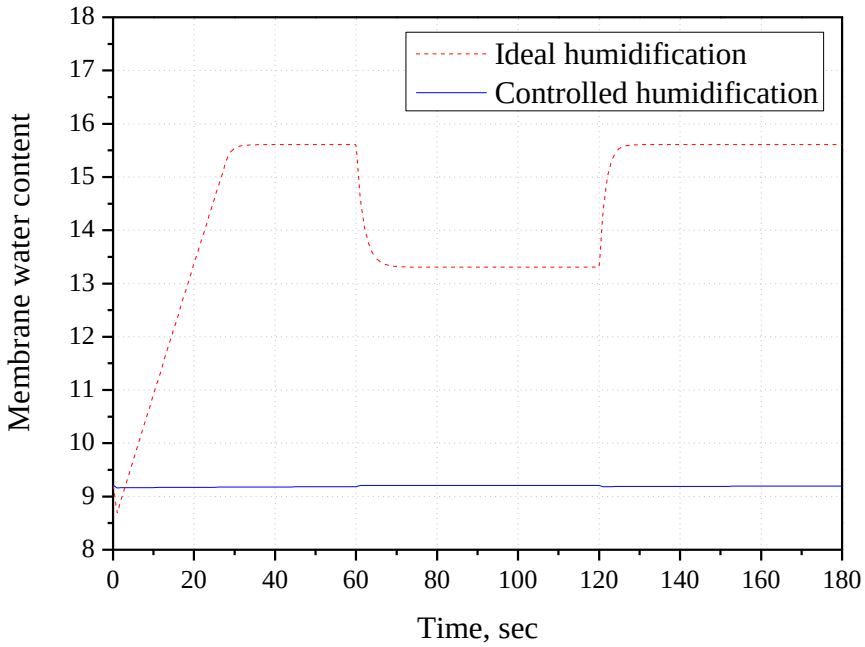

Figure 3-20. Membrane water content change with respect to the step current profile.

3.5. Experimental validation

We designed two test setups: a humidifier, and an air and water management system. Experiments were conducted to validate the model for the gas-to-gas humidifier and to validate the effects of the controls.

3.5.1. Model validation for a gas-to-gas humidifier

3.5.1.1. Experimental setup

As shown in Figure 3-21, the experimental setup for static and dynamic experiments with a humidifier designed by Dunlavy [58] consisted of the humidifier (FC-200-780-10, Perma Pure LLC, NJ [59]), an air flow system, a heating and humidification system, sensors, and DAQ computer.

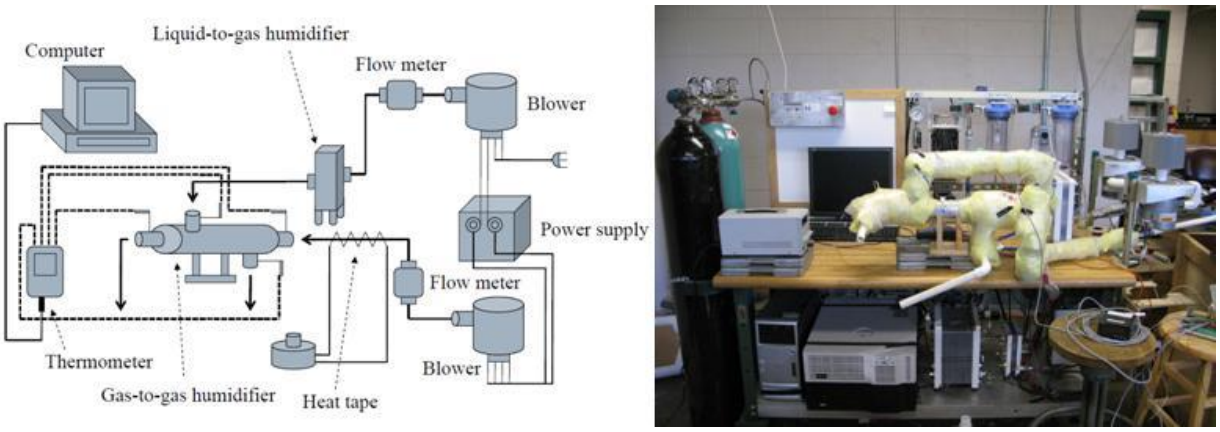

Figure 3-21. Layout of the test station for humidifier experiments [58].

Three blowers and associated power supplies used for blower speed control were located on the right side of the test station. One blower supplied dry air flow to the tube side of the humidifier, and two were used to produce wet air flow entering the shell side in combination with a liquid-to-gas humidifier to overcome the back pressure generated in the liquid-to-gas humidifier. This approach gave the humidifier a counter-flow configuration as a result of the shell-side flow entering from the top left. In-line flow meters were used directly after the blower so that the temperature at each flow meter would be equal, thereby ensuring that the same volumetric flow rate was read by each flow meter. The dry air flow passed through piping that was heated by a heater coil. The wet air flow was heated by heated water passing through the liquid-to-gas humidifier. Thermocouples and humidity sensors were located at the inlets and outlets of the humidifier where the temperature and humidity directly before entering the device could be known, and so that measurement error due to heat loss could be minimized. A humidity sensor was not placed at the exhaust outlet because the humidity condition at this point is not important. Finally, the thermocouples were connected to the thermocouple reader that was connected to the data recording PC.

3.5.1.2. Uncertainty analysis

Since the objective of this experiment is to determine how accurate the humidifier model is, it is essential that the uncertainty of the physical measurements also be known with confidence. In order to do this, an uncertainty analysis of measurements is presented so that the total uncertainty of all components in the system can be known. Typically, the total uncertainty of the measurement devices is the root mean square of the uncertainties of all components given by:

$$F_{total} = \sqrt{\sum_{i=1}^{k} F_i^2} \tag{3- 18}$$

where F is uncertainty and k is number of components in hypothetical case. In this experiment, there are two measurements that are presented as results: the temperature and relative humidity at the humidifier outlet. The uncertainty of the humidifier outlet temperature can be estimated by considering the accuracies of the thermocouples. According to data sheets of thermocouples, each thermocouple has an uncertainty of ± 0.5 ℃ for the temperature range used in the experiments. Thus the total uncertainty of all four thermocouples used in the experiments is given by

$$F_{TC,total} = \sqrt{(0.5)^2 + (0.5)^2 + (0.5)^2 + (0.5)^2} = 1\,^{o}\mathrm{C} \tag{3- 19}$$

whereby the most accurate measurement of the humidifier outlet temperature can be known with confidence to be less than or equal to 1 ℃ above or below the measurement.

Similarly, three relative humidity sensors have accuracies of ± 3 %, ± 1.5 %, and ± 2 %. Therefore, the total uncertainty of the relative humidity at humidifier outlet can be given by

$$F_{HS,total} = \sqrt{(3)^2 + (1.5)^2 + (2)^2} = 3.9\% \tag{3- 20}$$

whereby the best measurement of the relative humidity is less than or equal to approximately 3.9 % above or below the measured value.

With this in mind, it should be noted that the two-phase humidifier model developed [58] is within the uncertainty of the measured values. However the two-phase model for the relative humidity is more often within the uncertainty of the measured values than that for the temperature.

3.5.1.3. Experimental procedure

Experiments were conducted to evaluate the active control strategy that regulated the humidity of the air flow entering the fuel cell stack though the tube side of the humidifier by adjusting the shell side inlet exhaust gas flow rate. This process involved setting flow rates equal to each other, and then keeping the tube-side flow rate constant while incrementally decreasing the exhaust flow rate. The theory is that as the exhaust gas flow rate is decreased, the temperature and the humidity of the tube-side outlet air would decrease as well.

Since the PEM fuel cell is likely to experience a situation similar to a step increase power requirement whenever the vehicle demands extra speed or power, the step input has a practical basis. Thus, a test was performed to examine the system's response to step changes in exhaust gas flow rate. In the test, a pulse pattern was used so that flow rates were stepped up and down at specific time intervals, thereby repeating the process several times.

3.5.1.4. Experimental results and analysis

The static and dynamic behavior of the humidifier was used to validate the model. As shown in Figure 3-22, the simulated results were initially in relatively good agreement with the

experimental results. When the flow rate exceeded 100 slpm, the error became approximately 10% because the exhaust air temperature varied at the different exhaust flow rates.

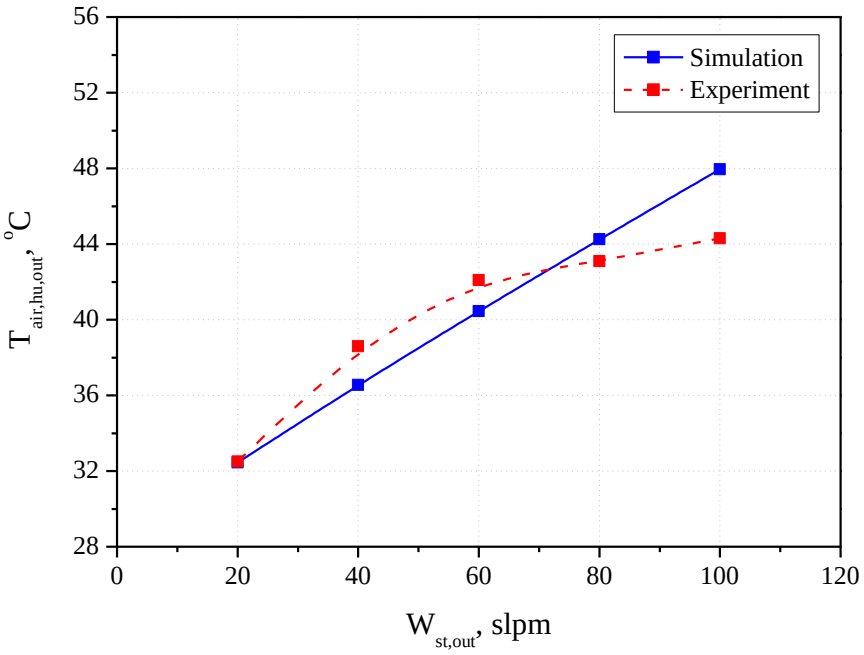

Figure 3-22. Temperatures for variable exhaust flow rates (dry air flow rate = 140 slpm).

As shown in Figure 3-23, both results for the wet outlet humidity match fairly well. The simulated value reached only 99.7% because of the drop in the high exhaust flow rate. When the flow rate dropped below 40 slpm, the relative humidity of the wet air decreased, and the exhaust flow rate increased from 80 to 100 slpm.

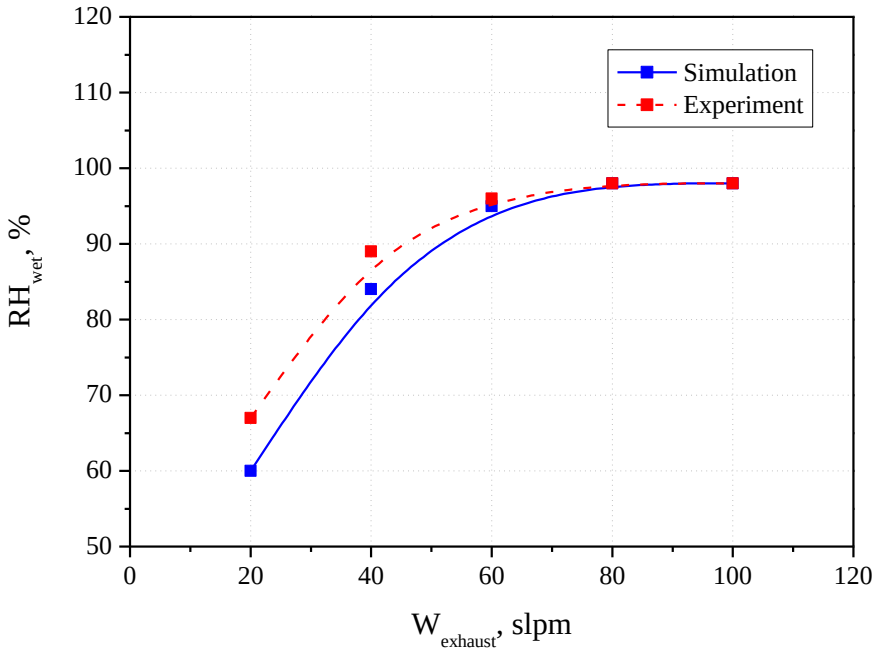

Figure 3-23. Humidity for variable exhaust flow rates (dry air flow rate = 140 slpm).

To validate the dynamic responses, the dry flow rate was maintained at approximately 140 slpm while the exhaust flow rate was stepped up and down between 15 and 30 slpm. The goal was to allow the system enough time to approach a steady-state value before changing the flow rate again. Thus, 15 min (except for the first 5) were allowed for each flow rate, and the total length of the run was one hr. Because the exhaust inlet temperature changed as the flow rate was changed, a record was kept of all of the data that could be recorded; therefore, when running the simulation, the record could be mapped into the inputs of the model and run.

Figure 3-24 shows the response of the wet outlet temperature with time corresponding to the simulation and experiment. The results appear to follow the same trend, although the experimental data appears to be slightly delayed after the flow rate increased or decreased, and is slightly lower (or higher) in amplitude depending on the time. In contrast, the simulation appears

to have reacted almost simultaneously to the step increase or decrease in flow rate, and reached higher amplitudes. The temperature for the simulation at 15 slpm is higher than that of experiment.

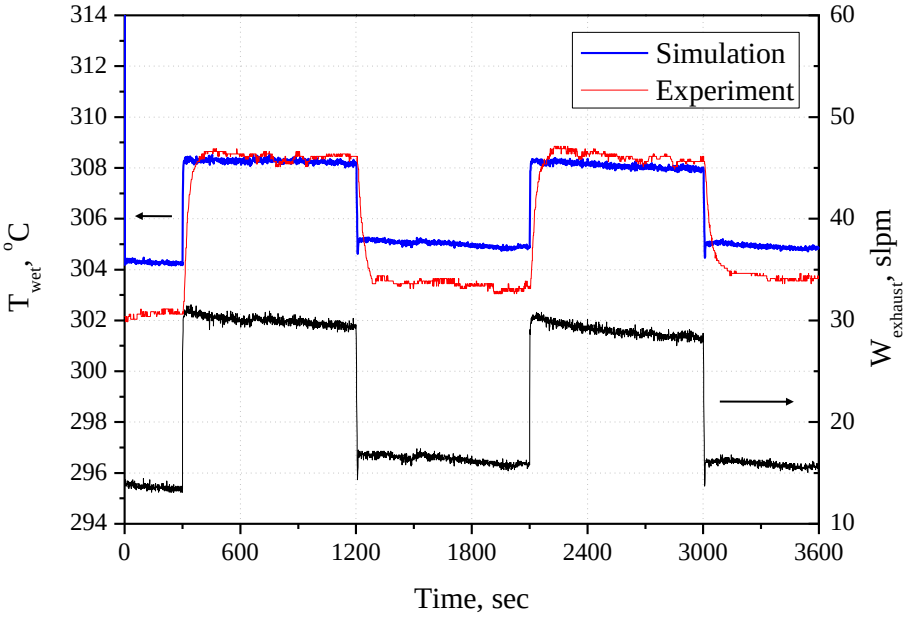

Figure 3-24. Temperatures for step exhaust flow rate.

Figure 3-25 shows humidity changes for the step exhaust flow rate. The relative humidity of the wet air flow from simulation was lower than that from experiment because of the temperature difference between simulation and experiment, as shown in Figure 3-24.

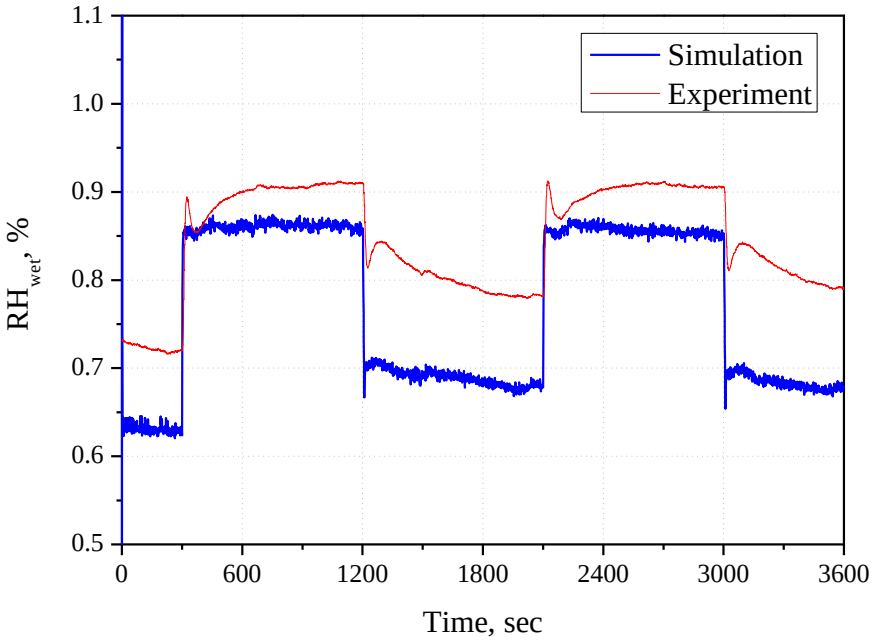

Figure 3-25. Humidity for step exhaust flow rate.

3.5.2. Experiments for controls of BOP

3.5.2.1. Experimental setup

The experimental setup consisted of a two-cell stack and the BOP, which includes an air supply and humidification system, a hydrogen delivery system, a thermal circuit, an electronic load, sensors, and processing units, as shown in Figure 3-26.

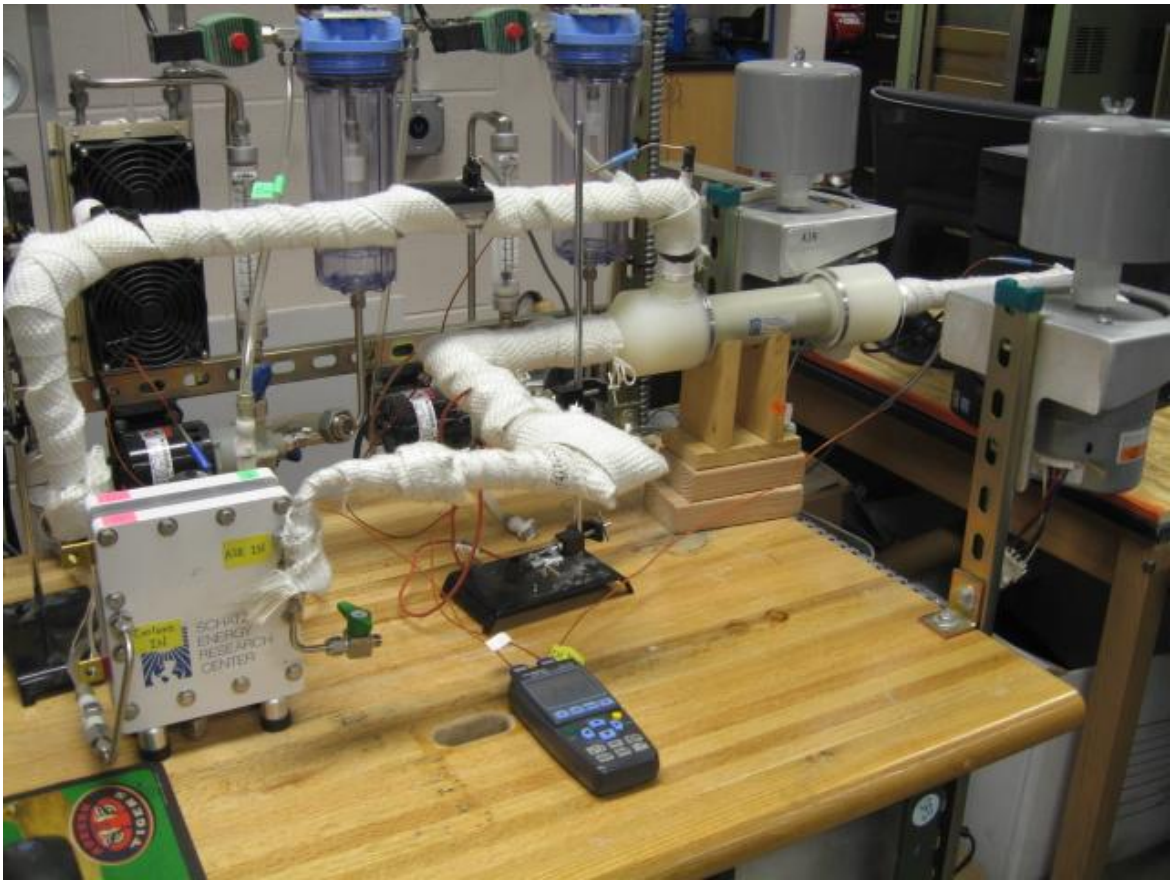

Figure 3-26. Fuel cell test station.

a. Fuel cell and stack

The cell has an active area of 140 cm^2. The membrane and the GDL have thicknesses of 0.035 mm and 0.4 mm, respectively. The plate for the gas flow channel is 1.5 mm thick and is made of graphite. The plates for the coolant channels and the separator are made of graphite with thicknesses of 3 mm and 1.5 mm, respectively. The thickness of the endplate and the bus plate are made of garolite with thicknesses of 28.5 mm and gold-plated stainless steel with thicknesses of 1.5 mm, respectively.

The stack was constructed with two cells separated by a thermal conductive plate in order to minimize the potential influence of the coolant on the working temperature. Except for the

separator, the other components of the stack are the same as those of a typical two-cell stack with the coolant channel between the cells, as shown in Figure 2-6 (a).

b. Design of BOP

Three subsystems were designed to validate the proposed control strategies for the BOP. These include an air and water management system, a hydrogen supply system, and a coolant system.

The air and water management system is shown in Figure 3-27. This management system was designed to supply humidified air to the fuel cell stack. The air flow was controlled by an 800 W Windjammer^{TM} 5.7 inch (145 mm) brushless DC blower (AMETEK, PA) capable of producing up to approximately 67 ft^3 min^{-1} (> 1800 slpm) of flow at a no-load condition. The blower was controlled either electronically or manually with a speed control of 0-10 DC V. A power supply with a range of 0-30 V was used for the manual speed control and the power for the blower came from an AC outlet.

The humidifier used in the experiment was a gas-to-gas humidifier (FC-200-780-10, Perma Pure LLC, NJ) with an operating range from 50 to 300 slpm and up to 80 ^oC. The humidifier contains 780 individual tubes though which the dry air travels, and around which the exhaust gas from the fuel cell stack travels.

The conditions of the air at the inlet and outlet of the stack were monitored using LABVIEW software. Two mass flow meters (TSI 4226-01-01, TSI Incorporated, MN) were used to monitor the flow rate of the dry air and exhaust gas flows entering the humidifier. The relative humidity and temperature of the air flow at the fuel cell stack inlet were measured by a humidity/temperature transmitter. The humidity of the supplied air was mainly determined by the

flow rate, the relative humidity, and the temperature of the exhaust gas flow entering the humidifier. Thus, the conditions of the exhaust gas flow were measured by a humidity sensor and thermocouple, and by a flow meter.

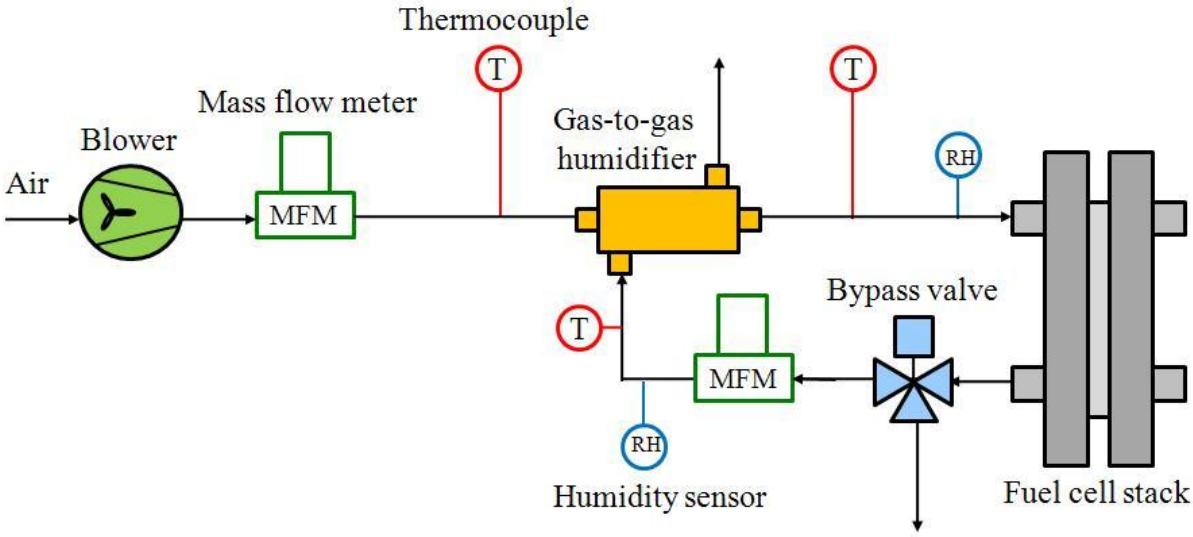

Figure 3-27. Structure of air supply and humidification system.

The hydrogen supply system is shown in Figure 3-28. The hydrogen system supplied pure hydrogen gas from a high pressure cylinder to the fuel cell, thereby reducing the hydrogen pressure to an appropriate level. From the manual valve, the hydrogen flowed through an in-line 15 micron filter to remove debris from the gas stream to protect downstream components and the fuel cell. The mass flow meter sensed flow over a 0-20 slpm range. The high pressure hydrogen was reduced to 2.7-5.5 psig by a low pressure regulator. After passing though the regulator, the flow into the fuel cell stack was controlled by a supply solenoid valve. A pressure gauge indicated the local hydrogen pressure at the inlet of the fuel cell stack. During the operation of the fuel cell stack, a purge solenoid valve located at the outlet of the fuel cell stack removed the water accumulated on the anode side.

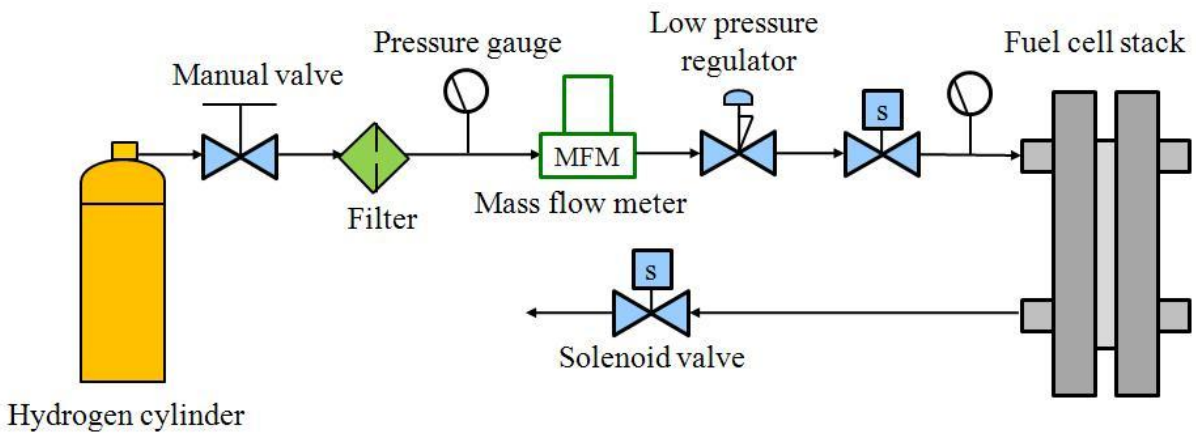

Figure 3-28. Structure of hydrogen supply system.

The thermal circuit shown in Figure 3-29 circulated deionized (DI) water to control the temperature of the water exiting the fuel cell stack during operation. When DI water leaked from the thermal circuit, DI water addition to the water reservoir was accomplished using an automatic solenoid valve triggered by a float switch. The water flow rate could be manually throttled with a valve located at the pump outlet. Flow indication was provided by a rotameter downstream of the throttle valve (HW-07187-04, Cole-Parmer, IL). If the water pump cannot supply enough water to cool the temperature of the water exiting the stack while the stack is running, the stack temperature will rise and the cooling fans contacting the radiator will run in order to reject the heat contained in the water.

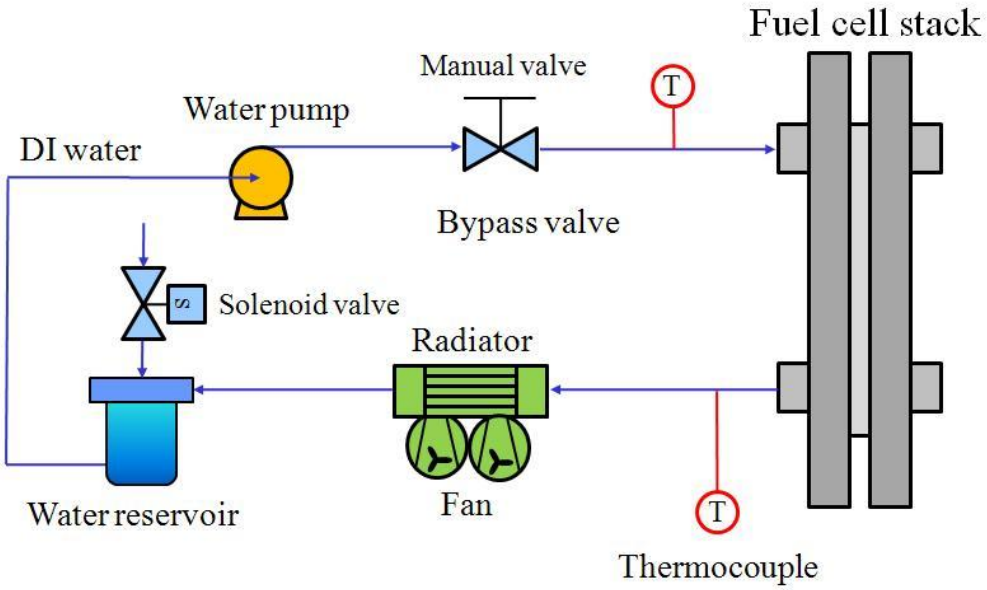

Figure 3-29. Structure of thermal circuit.

The fuel cell stack was connected to an electronic load module operating at a maximum of 1 kW. The operating modes of the E-load include constant current, an IV curve, and a load profile that can be input by the user.

Two T-type thermocouple probes (TMTSS-062U-6, Omega Engineering, INC., CT) with a working range of -200 to 350 ^{o}C and an accuracy of ± 5 ℃ were used to measure the temperatures of the dry air and the exhaust gas flows at the humidifier inlets. A humidity sensor and probe were used at the inlet of the shell side, and the humidity sensor and transmitter measured the humidity of the dry air at the inlet of the tube side. This sensor was located at the inlet of the tube-side because it had the lowest accuracy compared to other humidity sensors, and no software was installed to record data. However, the disadvantages of this sensor were not a

problem in the experiments because the humidity at the dry inlet rarely varied by more than 1% RH when the temperature and flow rate were set.

A handheld thermocouple reader used in the experiments (HH147, Omega Engineering, INC., CT) recorded the temperatures measured by four thermocouples. This device can monitor the temperatures at all four ports simultaneously, Furthermore, the device is capable of recording up to 10,000 data points via an RS-232 cable connected to its own recording software installed in a computer.

A computer equipped with National Instruments Data Acquisition (DAQ) hardware and LabVIEW software was used to monitor the data sets measured by the flow meters, thermocouples, and humidity sensors, and to control the test station. The data acquisition and signal conditioning system incorporated analog and digital inputs and outputs.

3.5.2.2. Uncertainty analysis

In this experiment, there are three measurements that are strongly related with the stack voltage as experimental result: the flow rate, temperature, and relative humidity at the humidifier outlet. Similar to the uncertainty analysis for the humidifier experiments, two flow meters have accuracies of ± 2 %, and ± 2 % from the data sheets. Thus the total uncertainty of two flow meters used in the experiments is given by:

$$F_{FM,total} = \sqrt{(2)^2 + (2)^2} = 2.8\% \qquad (3\text{-}21)$$

whereby the most accurate measurement of the humidifier outlet temperature can be known with confidence to be less than or equal to 2.8 % above or below the measurement.

Each thermocouple has an uncertainty of ± 0.5 ℃ for the temperature range used in the experiments. Thus the total uncertainty of all four thermocouples used in the experiments is given by:

$$F_{TC,total} = \sqrt{(0.5)^2 + (0.5)^2 + (0.5)^2} = 0.86\,^{o}\mathrm{C} \quad (3\text{- }22)$$

whereby the most accurate measurement of the humidifier outlet temperature can be known with confidence to be less than or equal to 0.86 ℃ above or below the measurement.

Similarly, two relative humidity sensors have accuracies of ± 3 %, and ± 2 % from the data sheets. Therefore, the total uncertainty of the relative humidity at humidifier outlet can be given by

$$F_{HS,total} = \sqrt{(3)^2 + (2)^2} = 3.6\% \quad (3\text{- }23)$$

whereby the best measurement of the relative humidity is less than or equal to approximately 3.6 % above or below the measured value.

3.5.2.3. Experimental procedure

Experiments on the static behavior of the fuel cell stack were conducted to evaluate the performance of the active control strategy using a three-way valve that adjusted the exhaust gas flow rate entering the shell side of the humidifier. The process included keeping the dry air flow rate constant while incrementally decreasing the exhaust flow rate from the stack at 10 and 60 A, and keeping the stoichiometric number at 2 while increasing the current density from 0 to 60 A. The theory is that as the three-way valve opening factor is increased at low current, the stack voltages would increase as well. As the three-way valve opening factor is decreased at high load current, the cell voltages increases.

Experiments on the dynamic behavior of the fuel cell stack were conducted to determine the response of the fuel cell stack to dynamic inputs of the three-way valve opening factor at 10 A.

3.5.2.4. Experimental results and analysis

The first experiment involved varying three-way valve opening factor by 25 % incrementally at 10 A where the flow rate, relative humidity and temperature of the dry air were maintained at 8 slpm, 46 % and 57 ^{o}C, respectively. The stack voltage was measured every 15 min at different opening factors. As the valve opening factor increases, the stack voltage increases because the membrane becomes humidified and proton conductivity is increased.

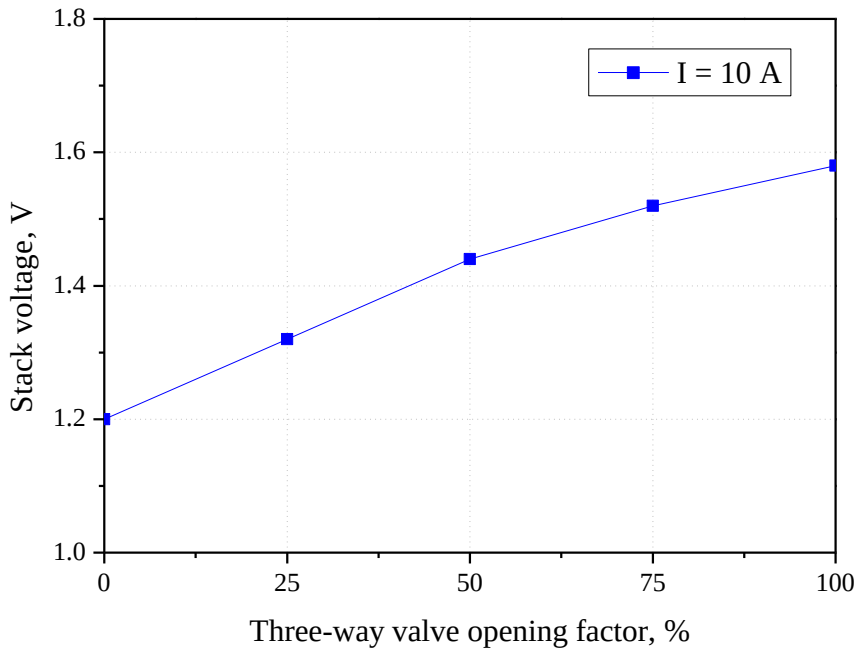

Figure 3-30. Stack voltages with different three-way valve opening factors at 10 A.

The second experiment was conducted by the same process as the first experiment, but at 60 A, where the fuel cell operation is safe. The flow rate, relative humidity and temperature of the

dry air were maintained at 25 slpm, 44 % and 56 ^{o}C, respectively. It has to be noted that the relative humidity of the exhaust gas at stack outlet was almost 1.0. The peak of the stack voltage was obtained at 25 % of the valve opening factor. When all the exhaust gas flows to the ambient, the stack voltage is a little lower than that of 25 %. On the other hand, the stack voltage decreased as the valve opening factor was increased. It indicates that the water flooding was occurred and results in degradation of the stack voltage.

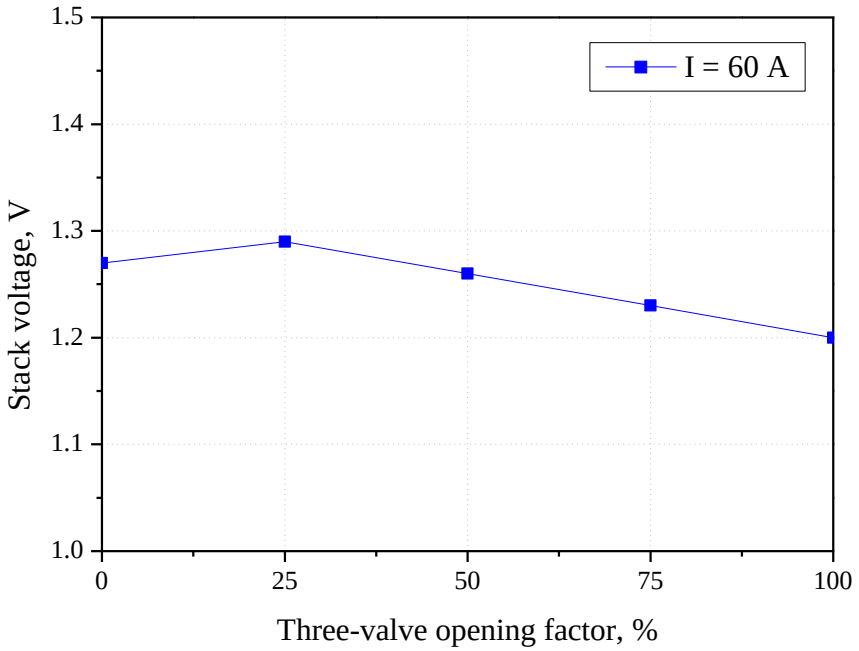

Figure 3-31. Stack voltages with different three-way valve opening factors at 60 A.

Experimental result is illustrated in Figure 3-32. Since the relative humidity of the exhaust gas at stack outlet is less than 100% at low current region, the three-way valves for both humidification systems were fully opened for all the exhaust gas to flow into the shell side of the humidifier. Therefore there was little difference of the stack voltages between controlled and uncontrolled systems at I = 10A and 20A. However, it was observed that the difference of the

stack voltages became greater as the current increased. It indicates that uncontrolled humidification supplied more amount of the exhaust flow than the required one, which resulted in occurrence of water flooding.

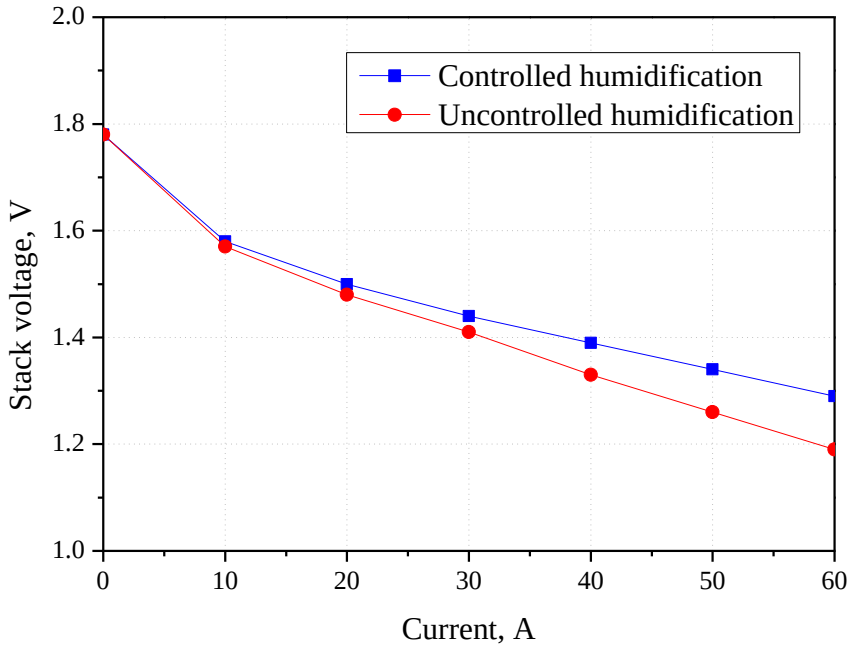

Figure 3-32. I-V characteristics of stack between different humidification.

For the experiments on the dynamic behavior of the stack depending upon the three-way valve opening factor, the flow rate of the dry air at 10 A was maintained at 8 slpm. The three-way valve didn't allow the exhaust gas to flow into the humidifier for 20 min. After then, the opening factor of the three-way valve became 100 % and all the exhaust gas flowed into the humidifier. Finally, the three-way valve opening factor came back to zero at 30 min. The experimental result showed that the stack voltage gradually changed even though the three-way valve was suddenly opened or closed as shown in Figure 3-33. In particular, when the valve was fully opened, the relative humidity of the stack inlet air slowly increased, which resulted in

increase of the stack voltage as well as the relative humidity of the exhaust gas at stack outlet. Consequently, more water was transferred from the exhaust gas to the dry air though the humidifier.

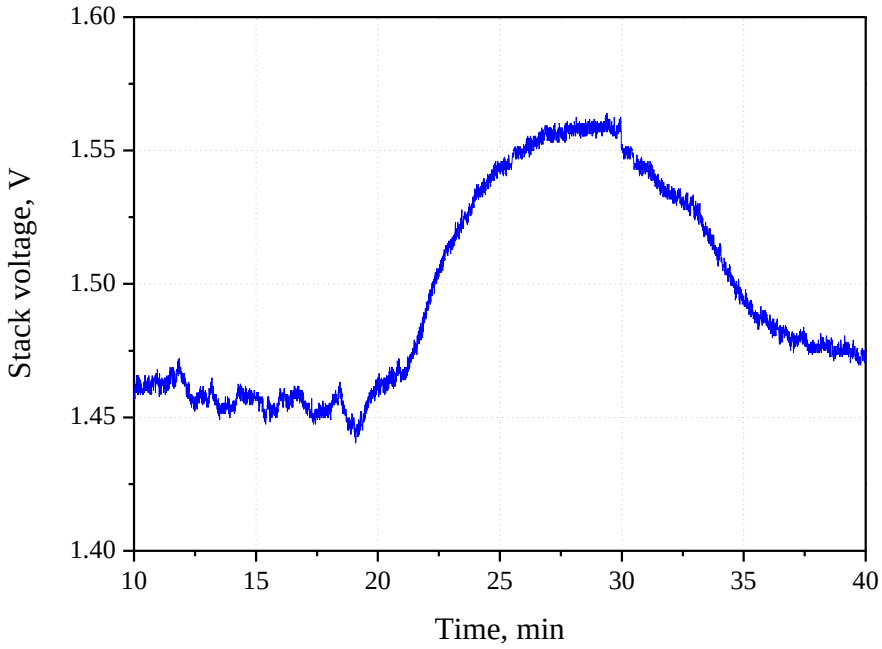

Figure 3-33. Dynamic behavior of the stack voltage for step valve opening factor at 10 A.

3.6. Summary

In this chapter, new configuration of AWM using a gas-to-gas humidifier and a bypass valve was proposed and the component models for the proposed configuration were developed. While the blower regulated the dry air flow rate supplying to the fuel cell, the bypass valve adjusted the exhaust gas flow rate entering he humidifier to maintain the membrane water content at desired level. The integrated model including an isothermal and two-phase stack model and BOP models were simulated. The developed feedback controllers for AWM were shown to have successfully maintained the oxygen excess ratio and membrane water content at the desired level. As a result,

the net power of the stack increased due to high chemical reaction rate and low ohmic over-potential.

Experiments were performed to characterize the static and dynamic behavior of the humidifier installed in the fuel cell station. The results showed that the relative humidity of the air flow exiting the tube side of the humidifier could be controlled by the wet air flow rate entering the shell side. Furthermore, the temperature of the air flow at the outlet of the tube side was increased though the humidifier. After the humidifier experiment, a fuel cell test station was modified to verify the performance of the proposed configuration, including the humidifier and the bypass valve. It was confirmed that the proposed control strategy was very effective in improving the degradation of stack power output caused by membrane dehydration and/or water flooding.

Chapter 4 Thermal Management

When a fuel cell generates electricity, heat is generated at the same time. The generated heat increases the temperature in the fuel cell. The elevated temperature can improve gas transportation, ease the removal of water in the catalyst, and increase the mobility of water vapor in the membrane. However, excessive heat could create local hotspots that damage thin layers and result in degradation of the components. Conversely, a low temperature decreases efficiency of the fuel cell because of low reaction rates and increased concentration over-potential due to increased condensation of water. Therefore, a thermal management system should be designed to optimally control the temperature. In this section, different configurations of thermal management system (TMS) and their associated control strategies are described.

4.1. System configurations

A typical thermal management system consists of a radiator, a fan, a reservoir, and a coolant pump, as shown in Figure 4-1. The system has only one path for coolant flow where heat exchange takes place. Thus, there is little freedom to manipulate the heat exchange rates. As a result, power consumption of the coolant circuit cannot be optimally controlled for a given heat rejection rate, which decreases the overall system efficiency.

A potential solution to resolve this limitation is to use an additional three-way valve as shown in Figure 4-1. The three-way valve allows coolant exiting from the stack outlet to bypass to the reservoir, or to flow into the radiator to exchange heat with the ambient air. In addition

the reaction time of the valve is faster than that of the coolant pump. Therefore, the coolant temperature entering the fuel cell stack can be manipulated more quickly than by using the coolant pump, and the coolant pump can supply less coolant than is needed to reject the same amount of heat from the stack compared to a typical system.

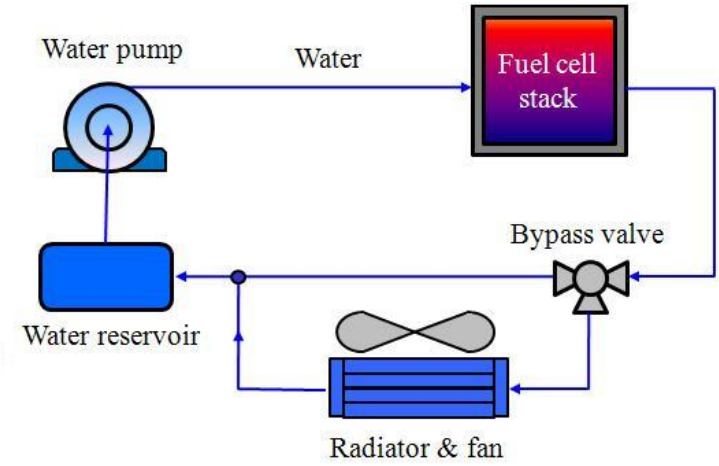

Figure 4-1. Configuration of thermal management using a bypass valve.

When the installed power increases, the physical size of thermal management system also increases. Because of strict spatial limitations in vehicle applications, a second thermal circuit can be added for better cooling and packaging effectiveness, as shown in Figure 4-2. The inner thermal circuit consists of a bypass valve, heat exchanger, water reservoir and water pump. The bypass valve allows the stack outlet water to a reservoir directly, or to flow into the heat exchanger. The heat exchanger transfers heat energy contained in water exiting the stack to the coolant. The water pump provides the cooled water from the water reservoir to the stack. The outlet thermal circuit consists of a heat exchanger, radiator, fan and coolant reservoir and coolant pump. The radiator exchanges the heat transferred from the hot water with the ambient and the

fan enhances the heat convection. The coolant pump supplies coolant from coolant reservoir to the heat exchanger.

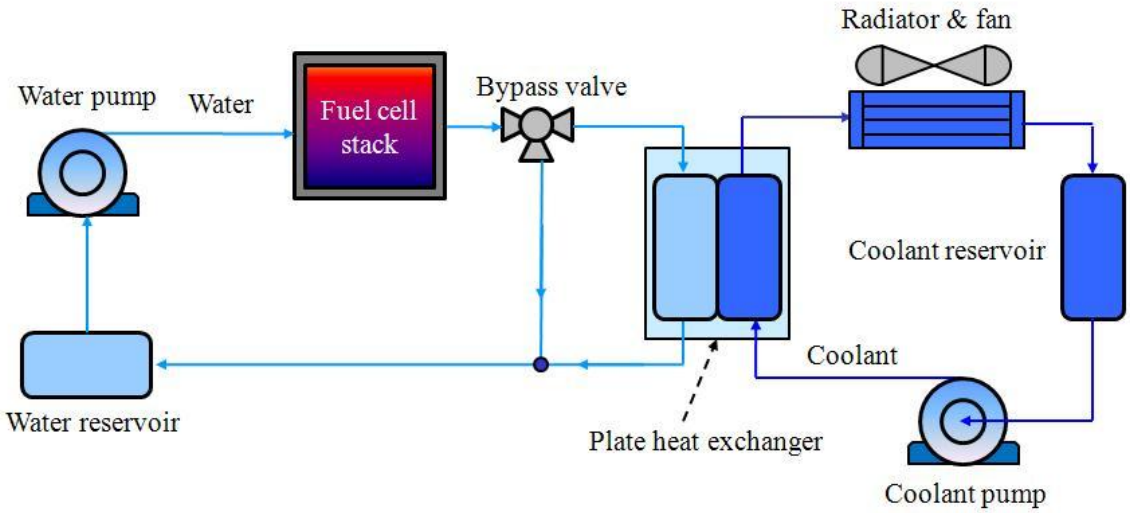

Figure 4-2. Configurations of thermal management with two thermal circuits.

4.2. Models for system components

4.2.1. Bypass valve

Similar to the bypass valve used for air and water management, the bypass valve in a thermal circuit allows the coolant flow at the stack outlet to bypass or to flow into a radiator. Coolant flow entering a radiator to reject heat contained in the coolant to the ambient is the product of coolant flow at the stack outlet $W_{st,c,out}$ (kg s^{-1}) and the opening factor of the bypass valve, k:

$$\begin{aligned} W_{st,c,out} &= W_{rad,c,in} + W_{c,bypass} \\ W_{rad,c,in} &= k \cdot W_{st,c,out} \\ W_{c,bypass} &= (1-k) \cdot W_{st,c,out} \end{aligned} \quad (4\text{-}1)$$

4.2.2. Radiator and fan

A radiator in the thermal circuit was used to maintain the temperature of the reservoir by rejecting the excess heat contained in stack outlet coolant to the ambient. Prediction of the heat transfer capability is the most challenging issue in modeling a radiator. Kroger [60] proposed empirical equations for the heat transfer coefficient h_{rad} (kW m^{-2} C^{-1}) and pressure drop p_r (kPa) as functions of the air flow rate though the radiator, W_{air} (kg s^{-1}):

$$h_{rad} = -1.4495 \cdot W_{air}^2 + 5.9045 \cdot W_{air} - 0.1157 \quad (4\text{-}2)$$

$$p_r = (32612 \cdot W_{air} - 75.396) + 101.325 \quad (4\text{-}3)$$

If the heat of the coolant is fully transferred to the radiator without loss, the heat capacity of the coolant is identical to that of the radiator. Thus, the radiator outlet coolant temperature can be expressed as a function of radiator geometry and heat convection caused by the temperature difference between the ambient and the radiator's outgoing air temperature [60]:

$$T_{rad,c,out} = T_{rad,c,in} - 0.5 \cdot Fr_{area} \cdot \frac{(T_{rad,c,in} - T_{amb}) \cdot h_{rad}}{W_c \cdot Cp_c} \quad (4\text{-}4)$$

where a constant (0.5) is the fitting factor (the author of [60] used a 0.5 m^2 radiator in the derivation of the heat transfer coefficient). Hence, Fr_{area} denotes the frontal area (m^2) of the radiator and $T_{rad,c,in}$ denotes the radiator inlet coolant temperature (K). Then, the electric power for the fan, P_{fan} (W), can be calculated using the thermal-dynamic relationship between pressure drop and air flow rate [48] as follows:

$$P_{fan} = \frac{1}{\eta_{elec} \cdot \eta_{fan}} \cdot \left(W_{air} \cdot Cp_{air} \cdot T_{amb} \cdot p_r^{\left(\frac{k-1}{k}-1\right)} \right) \quad (4\text{-}5)$$

4.2.3. Reservoir

The reservoir was assumed to be thermally insulated such that heat exchange takes place only at the heat exchanger or radiator by convection. Then, a variation of heat in the reservoir can be expressed as the sum of the heat that the water or coolant carries and the heat being exchanged with the ambient though plumbing. Thus, the variation of the reservoir coolant temperature $T_{res,c}$ (K) is given by [48]

$$mCp_{res,i} \cdot \frac{dT_{res,i}}{dt} = W_{res,i,in} \cdot Cp_i \cdot \left(T_{res,i} - T_{res,i,in}\right) + h_{pl} \cdot A_{pl} \cdot \left(T_{res,i,in} - T_{amb}\right) \quad (4\text{-}6)$$

where i denotes water or coolant, mCp_{res} is the heat capacity of the fluid contained in the reservoir (J), $W_{res,in}$ is the reservoir inlet flow rate (kg s^{-1}) that equals the flow rate at the stack outlet $W_{st,,out}$, h_{pl} is the heat transfer coefficient of plumbing (J m^{-2} K^{-1}) and A_{pl} is surface area of plumbing (m^2).

The water temperature at the reservoir inlet, $T_{res,w,in}$ (K), is expressed as a function of bypass valve opening factor k, the water temperature at stack outlet $T_{st,w,out}$, and the heat exchanger outlet $T_{he,w,out}$. Thus,

$$T_{res,w,in} = (1-k) \cdot T_{st,w,out} + k \cdot T_{he,w,out} \quad (4\text{-}7)$$

where the water flow rate at the reservoir outlet is equal to the water flow rate supplied to the fuel cell stack by the water pump.

4.2.4. Pump

A coolant pump circulates the coolant though the thermal circuit to remove heat from the fuel cell stack. Under the assumptions that no heat exchange occurs between the coolant and pump,

and no heat resistance exists between the heat generated in the stack and the coolant, the flow rate of the coolant is expressed by the following relationship with the heat source in the stack:

$$W_{st,c,in} = \frac{\dot{Q}_{sou,st}}{Cp_c \cdot \Delta T} \tag{4- 8}$$

The heat generation rate in the stack $\dot{Q}_{sou,st}$ is the product of the number of cells and the heat generated in a cell (Eq. 2-26):

$$\dot{Q}_{sou,st} = n \cdot \dot{Q}_{sou,cell} \tag{4- 9}$$

It is noted that the coolant pump power has the same trend as the coolant flow rate that is required to maintain a constant stack temperature during operation.

4.2.5. Heat exchanger

A heat exchanger is a device that enables heat energy from a gas or liquid to transfer to another gas or liquid, and has many applications in chemical plants, refrigerators, and air conditioners. Heat exchangers can be classified as a shell-and-tube type, and a plate-type. The shell-and-tube type is preferred for industrial applications because of high reliability and wide operating ranges, and where a large volume for gases at high temperature and pressure is needed. In contrast, the plate-type is preferred for a small heat exchange capacity where high heat transfer efficiency is required. A shell-and-tube type heat exchanger consists of a shell surrounding a bundle of tubes. Water runs through the tubes and coolant flows over the tubes (through the shell) to transfer heat between the two fluids. Conversely, the plate-type heat exchanger is uses metal plates to transfer heat between two fluids. Heat transfer in the plate-type takes place more effectively than in the shell-and-tube type because fluids spread out over the

plates and are exposed to large surface areas. This exchanger consists of a series of thin corrugated plates that are welded or brazed together, depending on applications of the heat exchanger. The plates are compressed together in a rigid frame to form an arrangement of parallel flow channels with alternating hot and cold fluids.

4.2.5.1. Model for a plate heat exchanger

To develop a model for the heat exchanger, the following assumptions were made:

1. The heat exchanger is regarded as a control volume.
2. No heat convection between the fluids and the ambient takes place.
3. The plate wall resistance is negligible.
4. The fluid flow rate is constant in the heat exchanger.
5. No phase change occurs in the coolant.

The Nusselt number, which represents a correlation for heat transfer coefficient, is a function of the thermal conductivity of fluid k and channel equivalent diameter D_e, and can be expressed by the heat transfer factor and the Prandtl number as follows:

$$Nu = \frac{h \cdot D_e}{k} = J_h \cdot \mathrm{Pr}^{1/3} \tag{4- 10}$$

where the heat transfer factor J_h is a function of C_h and y:

$$J_h = C_h \cdot \mathrm{Re}^{y} \tag{4- 11}$$

The effectiveness of the heat exchanger ε is defined as the actual heat transfer divided by the maximum possible heat transfer:

$$\varepsilon = \frac{\dot{Q}}{\dot{Q}_{\max}} \tag{4- 12}$$

The energy balance of the system is

$$\dot{Q} = mCp_w \cdot \left(T_{w,out} - T_{w,in}\right) = mCp_c \cdot \left(T_{c,in} - T_{c,out}\right) \tag{4- 13}$$

The maximum heat transfer rate is the product of the low heat capacity and the temperature difference between the water and coolant:

$$\dot{Q}_{\max} = mCp_c \cdot \left(T_{w,in} - T_{c,in}\right) \tag{4- 14}$$

The effectiveness is obtained using Eq. (4-13) and (4-14):

$$\varepsilon = \frac{mCp_c \cdot \left(T_{c,in} - T_{c,out}\right)}{mCp_c \cdot \left(T_{w,in} - T_{c,in}\right)} \tag{4- 15}$$

The temperature deviations of the water and coolant depend on the heat transfer between the water and coolant, and the enthalpy change between the inlet and outlet. Therefore, the temperature changes of the water and the coolant can be expressed by

$$mCp_w \cdot \frac{dT_w}{dt} = \dot{Q}_{he} + W_w \cdot Cp_w \cdot \left(T_{w,in} - T_{w,out}\right) \tag{4- 16}$$

$$mCp_c \cdot \frac{dT_c}{dt} = \dot{Q}_{he} + W_c \cdot Cp_c \cdot \left(T_{c,in} - T_{c,out}\right) \tag{4- 17}$$

The heat transfer rate is the product of the overall heat transfer coefficient $U_{overall}$, the surface area A, and the log mean temperature difference $LMTD$:

$$\dot{Q}_{he} = U_{overall} \cdot A \cdot LMTD \tag{4- 18}$$

where U is the overall heat transfer coefficient (W m^{-2} K^{-1}), A is the surface area (m^2), and $LMTD$ is the log mean temperature difference (K).

The overall heat transfer coefficient is calculated from

$$U_{overall} = \frac{1}{\frac{1}{h_w} + \frac{1}{h_c}} \tag{4- 19}$$

4.3. Control strategies

A control structure called bang-bang control is a well-known classical on-off control method used to keep the temperature of the coolant constant. However, bang-bang control does not consider optimization of the energy dissipated at the actuators, and thus the parasitic power in bang-bang control is greater than that for the state feedback control that is optimized in terms of the dynamic response.

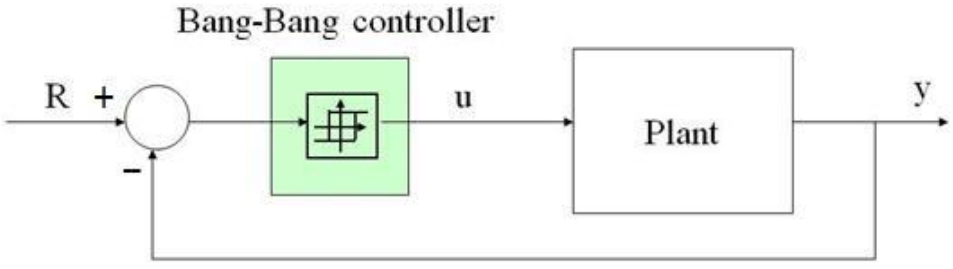

Figure 4-3. Block diagram of the coolant pump.

4.3.1. Temperature controls

As described in Section 4.1, new control strategies for non-isothermal fuel cell stack should be designed for the coolant circuit with a bypass valve shown in Figure 4-1. Variation of the

temperature of the stack can be obtained from the sum of a heat source and the heat exchanged with the water as follows:

$$m_{st} \cdot Cp_{st} \cdot \frac{dT_{st}}{dt} = \dot{Q}_{sou} + W_w \cdot Cp_w \cdot \left(T_{st} - T_{st,c,in}\right) \tag{4- 20}$$

where Cp_{st} is the specific heat of the stack (J kg^{-1} K^{-1}), W_w is the water flow rate (kg s^{-1}) as the control variable, and $\dot{Q}_{sou}$ is the internal energy source (J s^{-1}) and is a function of the load current.

Since Eq. (4-20) and the reservoir model (Eq. 4-6) are nonlinear, a Taylor expansion was used to linearize the equations at an operating point where the reservoir temperature and coolant flow rate were set at 64 ^{o}C and 0.93 kg/s, respectively, and the stack current and voltage are 140 A and 198 V, respectively. The state equations and variables are defined as follows:

$$\begin{aligned} \delta\dot{x} &= A \cdot \delta x + B_u \cdot \delta u + B_w \cdot \delta w \\ \delta y &= C \cdot \delta x \end{aligned} \tag{4- 21}$$

$x = \begin{bmatrix} T_{st} & T_{res} \end{bmatrix}$ (States)

$u = \begin{bmatrix} W_c & k \end{bmatrix}$ (Controlled input)

$w = I_{st}$ (Disturbance)

$y = \begin{bmatrix} T_{st} & T_{res} \end{bmatrix}$ (Output)

where the matrices of the linearized system (A, B_u, B_w , and C for a single cell and a two-cell stack) are listed in Appendix C.

Based on Eq. (4-21), state feedback control with an integral control was designed as shown in Figure 4-4.

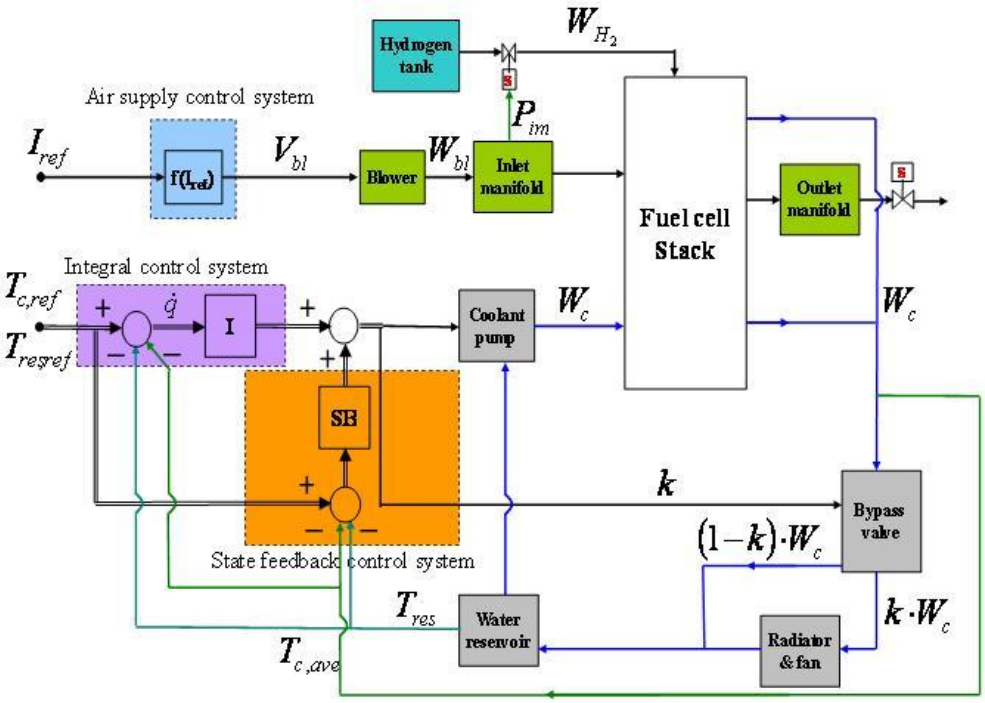

Figure 4-4. Block diagram of a state feedback controller with an integral controller.

The state feedback control handles the parasitic power dissipated in the coolant pump as one of its control objectives. Since the parasitic power of the coolant pump is directly proportional to the coolant flow rate, the coolant flow rate is included as a variable in the cost function as follows:

$$\dot{q} = \begin{bmatrix} T_{st}^{o} - T_{st} \\ T_{res}^{o} - T_{res} \end{bmatrix} \tag{4- 22}$$

$$J = \int_0^\infty \left(\delta x^T \cdot Q_z \cdot \delta x + q^T \cdot Q_I \cdot q + \delta u^T \cdot R \cdot \delta u \right) \cdot dt \tag{4- 23}$$

where the superscript ^{o} denotes the value at the operating point and Q_I is the weighting matrix for the integrator.

When the weighing matrix R is larger than the weighting matrix Q, the role of the coolant flow rate in the cost function is increased; subsequently, the gains of the controller are chosen such that the parasitic power is minimized. After several iterations with different values of weighting factor Q, the optimal control matrices K_p and K_I were obtained:

$$K_p = \begin{bmatrix} -1.2015 & 0.01 \\ -0.0521 & -3.1479 \end{bmatrix}, K_I = \begin{bmatrix} -0.1 & 0.0027 \\ -0.0027 & -0.1 \end{bmatrix} \quad (4\text{-}24)$$

4.3.2. Temperature controls based on a reduced-order observer

The aforementioned designed controller was based on the assumption that the stack is isothermal and that the temperature profile inside the stack is constant. The controller controls coolant flows based on the measured temperature of the coolant outlet. Under non-isothermal conditions, heat generation is location-dependent and the temperature gradient is formed through the stack that cannot be simply rejected from the proposed control. The heat source terms in the stack are expressed as a function of the current drawn, and are regarded as disturbances in the control loop. As a result, the heat rejected is less than the heat produced. A countermeasure is to estimate the temperature rise in layers that are directly related to the magnitude of the current load and compensate it as a feed-forward component to the temperature control loop.

The relationship between the current and the stack temperature was derived using Eqs. (4-20) and (2-26), which yield the following transfer functions in which v_{act} represents the activation over-potential:

$$\frac{T_{st}(s)}{I(s)} = \frac{-\frac{T \cdot \Delta s}{4 \cdot F} + v_{act}}{m_{st} \cdot Cp_{st} \cdot s + Cp_c \cdot W_c^o + h \cdot A}$$
$$\frac{T_{st}(s)}{I^2(s)} = \frac{R_{memb}}{m_{st} \cdot Cp_{st} \cdot s + Cp_c \cdot W_c^o + h \cdot A} \quad (4\text{-}25)$$

The source terms for the energy conservation equation yield the heat produced in the stack, and are dependent on the current. Since the load current as an input variable is known prior to determining the coolant flow rate, the resulting heat can be calculated based on the current. In [61], the feed-forward block is based on the relationship between the current and the stack temperature, and was introduced to suppress the surge in temperature. Due to the ignored source terms of layers and effect of coolant, the estimation in [61] was inaccurate. One of the drawbacks of their approach was insufficient rejection of heat by the coolant control. We propose a reduced-order observer that should continuously estimate the temperature in the catalyst. A block diagram for coolant control with a state feedback controller and a reduced-order observer is shown in Figure 4-5.

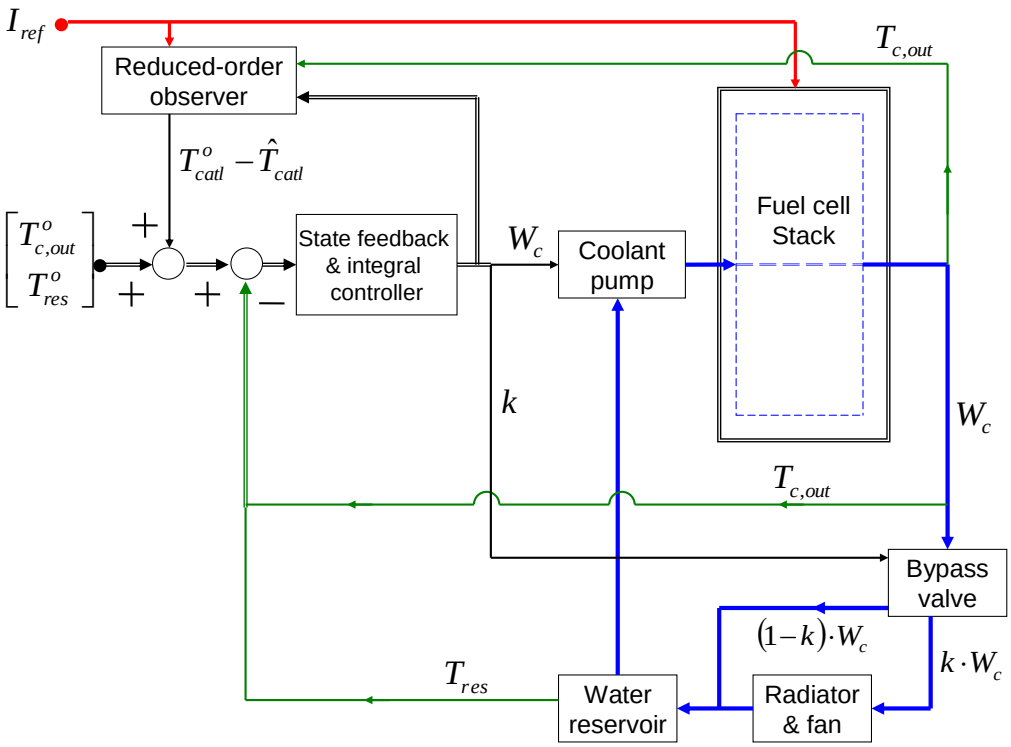

Figure 4-5. Block diagram for coolant control with a sFB and a reduced-order observer.

The estimated temperature obtained from the observer was used as an input variable for the coolant flow control loop. The coolant temperature was easily measured, whereas the temperature inside the cell was difficult to measure.

A two-cell stack model consists of 21 layers including 3 coolant channels, 4 bipolar plates, 4 gas flow channels, 4 GDL, 4 catalyst layers and 2 membranes as shown in Figure 2-6. Using thermal resistance and heat transfer equation, a bipolar plate, gas flow channel and GDL in the cathode or anode are combined to the cathode (ca) or the anode (can), and two catalyst layers and a membrane are combined to MEA as shown in Figure 4-6.

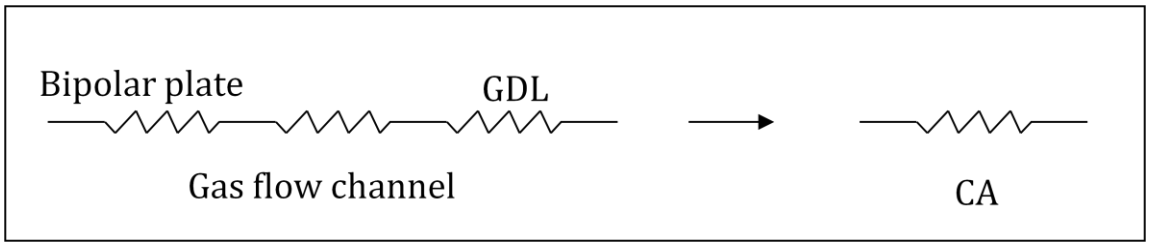

Figure 4-6. Example of the order reduction: cathode.

After a state space form for the temperature of individual layers was obtained using the energy conservation equation, the coolant temperature was defined as a measurable variable, and the temperatures inside cells were defined as an immeasurable state variable (for which an observer was designed). In addition, the load current was regarded as a disturbance, and the input variables were the coolant flow rate and the opening variable for the three-way bypass valve. The state equation was reformulated for a reduced-order observer, and the temperature of coolant channels and other layers including cathode (ca), anode (an) and MEA were defined as variable vectors x_b and x_a, respectively.

$$x_a = \begin{bmatrix} T_{ca,1} & T_{MEA,1} & T_{an,1} & T_{ca,2} & T_{MEA,2} & T_{an,2} \end{bmatrix}, \quad x_b = \begin{bmatrix} T_{c,1} & T_{c,2} & T_{c,3} \end{bmatrix} \tag{4- 26}$$

where *1* and *2* denotes cell number.

The state matrix was partitioned into two parts:

$$\begin{bmatrix} \delta\dot{x}_a \\ \delta\dot{x}_b \end{bmatrix} = \begin{bmatrix} A_{aa} & A_{ab} \\ A_{ba} & A_{bb} \end{bmatrix} \begin{bmatrix} \delta x_a \\ \delta x_b \end{bmatrix} + \begin{bmatrix} B_{u,a} \\ B_{u,b} \end{bmatrix} \delta u + \begin{bmatrix} B_{w,a} \\ B_{w,b} \end{bmatrix} \delta w$$
$$\delta y = \begin{bmatrix} 1 & 0 \end{bmatrix} \begin{bmatrix} \delta x_a \\ \delta x_b \end{bmatrix} \tag{4- 27}$$

The state variable, $\delta\dot{x}_b$, in Eq. (4-27) includes the measurable state δx_a, which was replaced by the following equation:

$$\delta\dot{x}_a = \delta\dot{y} = A_{aa} \cdot \delta y + A_{ab} \cdot \delta x_b + B_{u,a} \cdot \delta u + B_{w,a} \cdot \delta w \tag{4- 28}$$

The new equation includes a rule for the reduced-order observer:

$$\delta\dot{\hat{x}}_b = A_{bb} \cdot \delta x_b + A_{ba} \cdot \delta y + B_{u,b} \cdot \delta u + B_{w,b} \cdot \delta w + L \cdot \left(\delta\dot{y} - A_{aa} \cdot \delta y - B_{u,a} \cdot \delta u - B_{w,a} \cdot \delta w - A_{ab} \cdot \delta\hat{x}_b \right) \tag{4- 29}$$

The gain of the observer loop was optimized by applying the linear quadratic Gaussian method. However, the last term in Eq. (4-29) includes variable $\dot{y}$ that is very sensitive to high frequency noise. Therefore, a new state x_c was introduced, and (Eq. 4-27) was rewritten as

$$\delta x_c = \delta\hat{x}_b - L \cdot \delta y$$
$$\delta\dot{x}_c = \left(A_{bb} - L \cdot A_{ab} \right) \cdot \delta\dot{\hat{x}}_b + \left(A_{ba} - L \cdot A_{aa} \right) \cdot \delta y + \left(B_{u,b} - L \cdot B_{u,a} \right) \cdot \delta u + \left(B_{w,b} - L \cdot B_{w,a} \right) \cdot \delta w \tag{4- 30}$$

After several iterations with different weighting factors, the reduced-order observer gain *L* is given by

$$L^T = \begin{bmatrix} 21.174 & 19.322 & -2.018 & -11.79 & 3.383 & 19.748 \\ -0.425 & -0.0784 & 9.4086 & 14.297 & 7.773 & -4.81 \\ 0.033 & -0.19 & 17.764 & 20.749 & -3.312 & -9.379 \end{bmatrix} \tag{4- 31}$$

4.3.3. Temperature controls for two thermal circuits

Two coolants circuits are preferred for high power applications of more than 100 kW, where reduction of the physical size of the thermal management system and reduction of parasitic power are required. The objectives of the state feedback controls are to keep the temperature at a desired level, and to reduce the parasitic power dissipated in the water and coolant pumps.

A block diagram of TMS for inner and outer thermal circuits with a state feedback controller and an integral controller is shown in Figure 4-7.

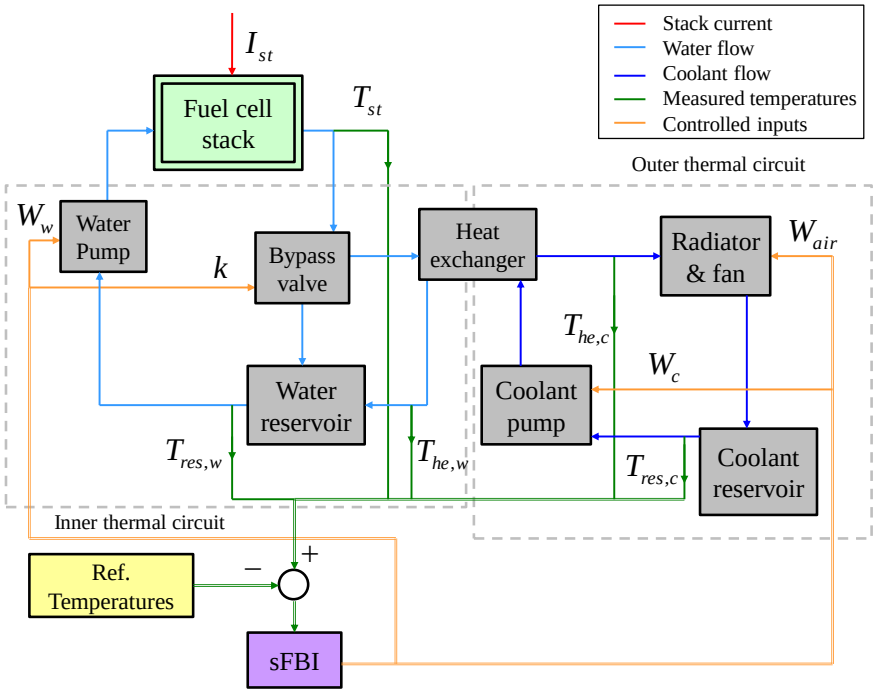

Figure 4-7. Block diagram for temperature control with a state feedback controller

Since the parasitic power of the pumps is proportional to the water or coolant flow rates, the water or coolant flow rates are included as variables in the cost function. The optimization of the gains was performed using the LQR method.

Integrator was used to suppress potential steady state errors. Thus, the errors of both closed loops were defined as a new state variable that was considered in the cost function as follows:

$$\dot{q} = \begin{bmatrix} T_{st}^{o} - T_{st} \\ T_{res,w}^{o} - T_{res,w} \\ T_{res,c}^{o} - T_{res,c} \\ T_{he,w}^{o} - T_{he,w} \\ T_{he,c}^{o} - T_{he,c} \end{bmatrix} \tag{4- 32}$$

where the superscript ^{o} denotes the value at the operating point.

Then, the rules for the optimal controlled inputs are obtained:

$$\delta u = -K \cdot \begin{bmatrix} \delta x & q \end{bmatrix}^{T} = -K_p \cdot \delta x - K_I \cdot q \tag{4- 33}$$

When weighting matrix R in the cost function J (Eq. 4-23) is larger than weighting matrix Q, the role of the coolant flow rate in the cost function increases. Subsequently, the gains of the controller were chosen to minimize the parasitic power of the pump. After several iterations with different weighting factors, the optimal control matrices K_p and K_I are given by

$$K_{p,w} = \begin{bmatrix} -1.729 & 0.372 & -2.92 & 0 & 0 \\ 0.5 & 0.921 & 1.192 & 0 & 0 \\ 0 & 0 & 0 & -0.875 & -0.031 \\ 0 & 0 & 0 & -0.027 & -3.164 \end{bmatrix},$$
$$K_I = \begin{bmatrix} -0.071 & 0.034 & -0.062 & 0 & 0 \\ 0.022 & 0.094 & 0.026 & 0 & 0 \\ 0 & 0 & 0 & -0.1 & 0.003 \\ 0 & 0 & 0 & -0.003 & -0.1 \end{bmatrix} \tag{4- 34}$$

4.4. Simulation and analysis

An integrated system with the fuel cell stack and thermal circuits is shown in Figure 4-8. The system has 5 state variables, 4 input variables connected to the controller: the water flow rate W_w, the bypass valve opening factor k_{bp}, the coolant flow rate W_c, and the air flow rate provided to the radiator by the fan W_{air}.

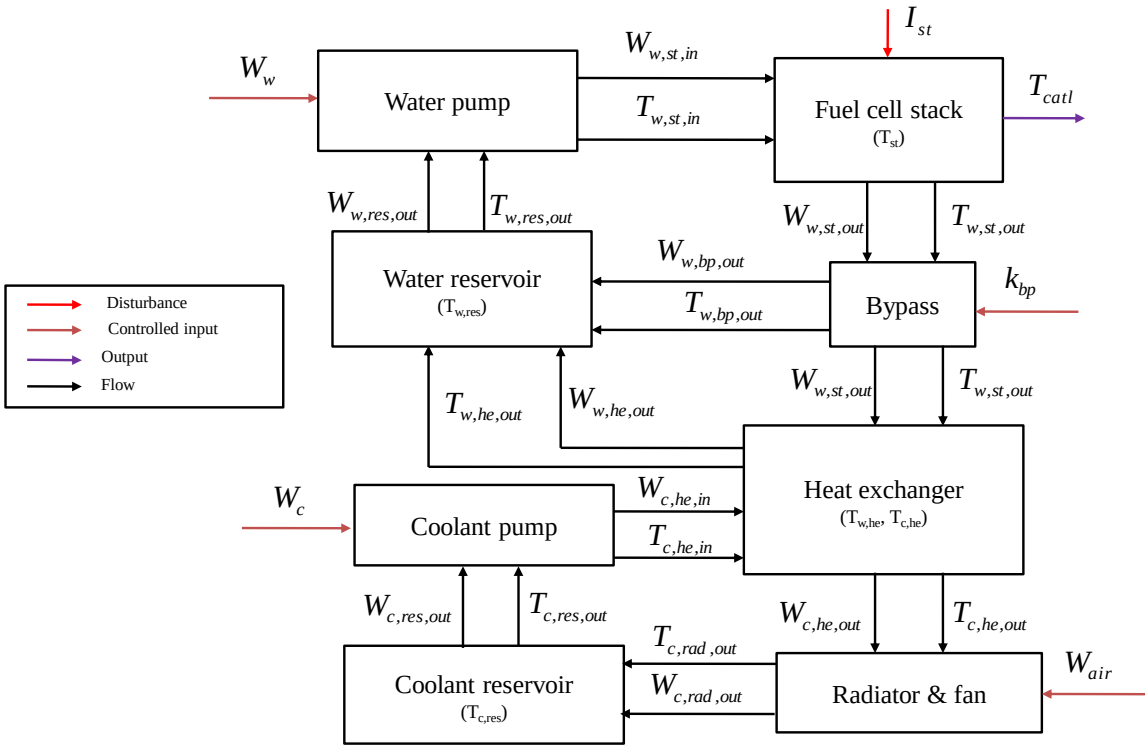

Figure 4-8. Block diagram of the proposed integrated system model for TMS.

Simulations were performed to analyze the dynamic behavior of the non-isothermal stack along with the thermal system and the associated control strategies. Analyses of temperature variations, the dynamics of water content in the membranes, and the oxygen excess ratio at the load currents are described in the following chapters. The parameters and reference data for the

models chosen are shown in Table 3-1. All models were coded using blocks provided in MATLAB® /Simulink® (R2010b, MathWorks, Natick, MA).

4.4.1. Temperature distribution in two cells

The temperature distribution through the plane of two cells with controllers is shown in Figure 4-9. As the current density increases stepwise from 0.5 to 0.7 A/cm^2, the temperatures of both cells decrease accordingly because more coolant is supplied to maintain the temperatures of the catalyst layers at the set value. In addition, the temperature difference between cells increased as the current density increased.

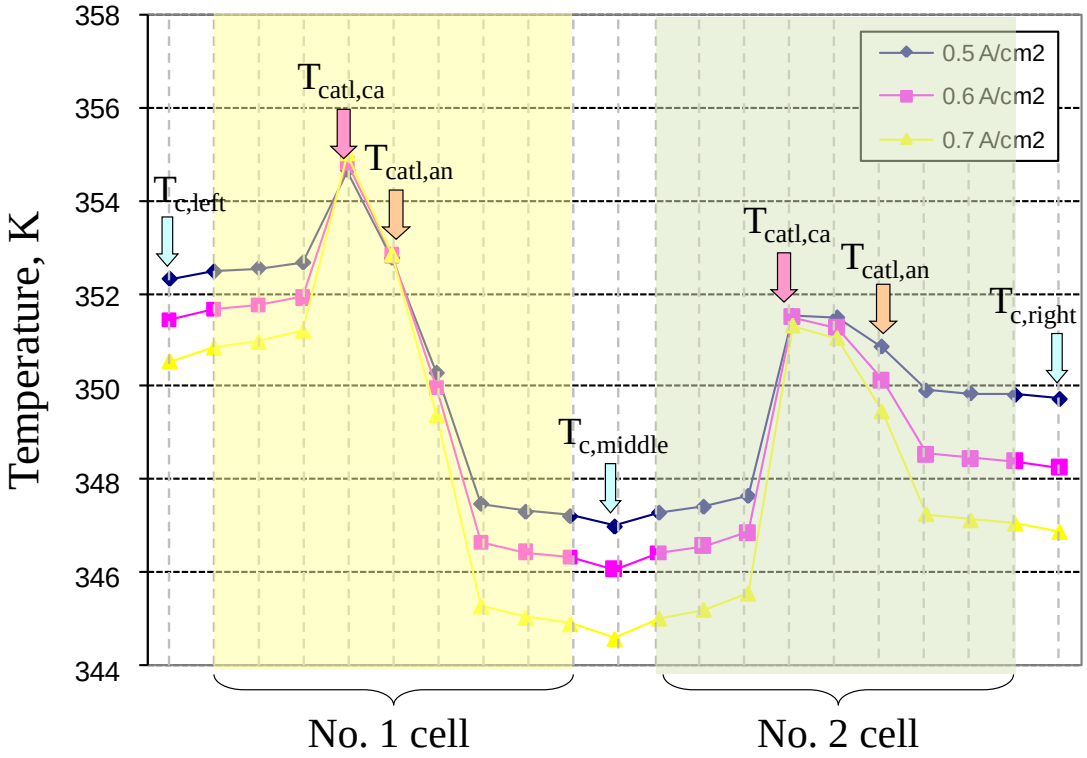

Figure 4-9. Temperature variation in the two cells depending on current density.

4.4.2. Effect of temperature on membrane water content

The membrane water contents between two cells at a step load current were compared, as shown in Figure 4-10. In general, the membrane water content is strongly influenced by the relative humidity, which is determined by the saturated vapor pressure depending on the temperature and vapor pressures of the cathode and anode sides. Even though the reactants on the anode and cathode sides are supplied with full humidification, the relative humidity in the gas channels on the anode side of the cells drops due to the effect of temperature on the gas flow channels. In addition, we note that the elevated temperature of the stack near a high load current leads to high saturated vapor pressure and low relative humidity on both sides of the cell. As a result, the membrane water content decreases.

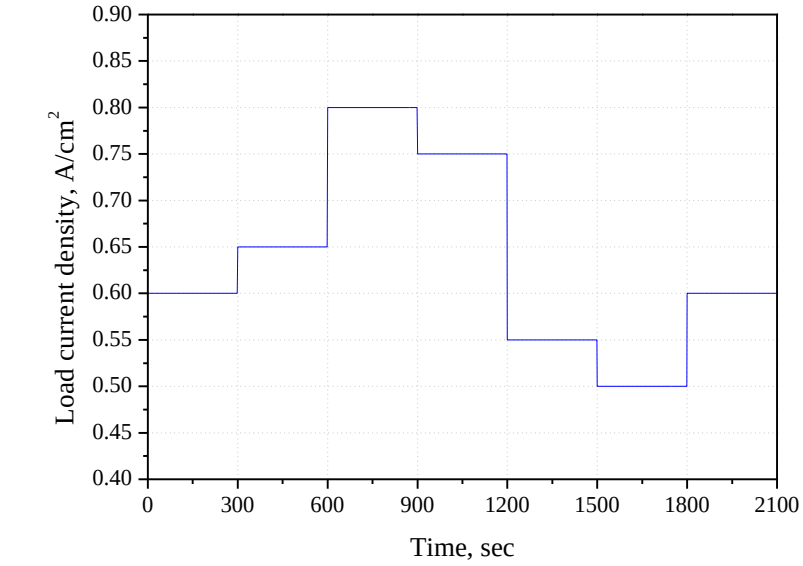

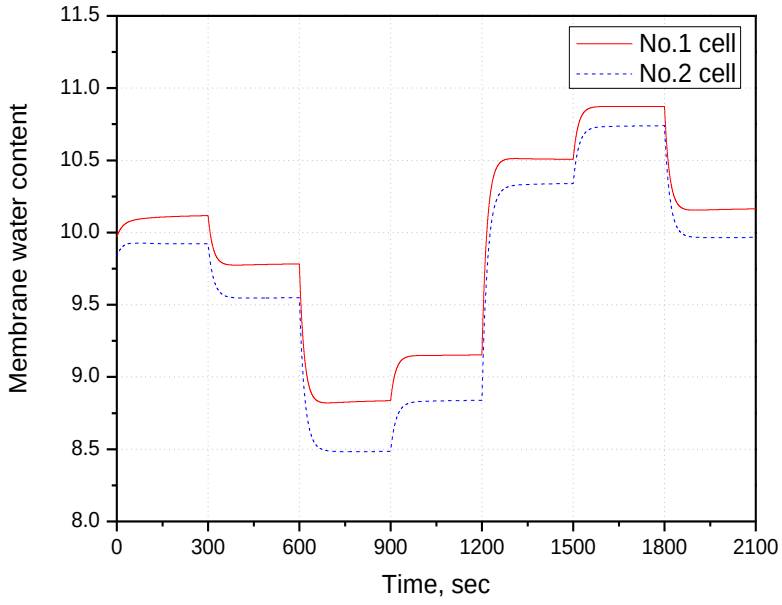

Figure 4-10. Water content in the membrane.

4.4.3. Effect of temperature on oxygen excess ratio

Figure 4-11 illustrates the oxygen excess ratio at a constant operating temperature with dynamically varying temperature and coolant control. At a constant operating temperature, the

oxygen excess ratio was maintained at 2.0. However, the oxygen excess ratio with variation of stack temperature was not kept at 2. The coolant supplied to the stack for reduction of heat generated in the stack decreased the temperature of the gas flow channel next to the coolant channel, which resulted in a lower cathode pressure than that at 80 ^{o}C. Since the air flow rate entering the stack depends on the difference in pressure between the cathode and inlet manifold, and the blower regulated by the controller developed for non-isothermal stack model supplied the same amount of air to the stack, the oxygen excess ratio was higher than 2.0.

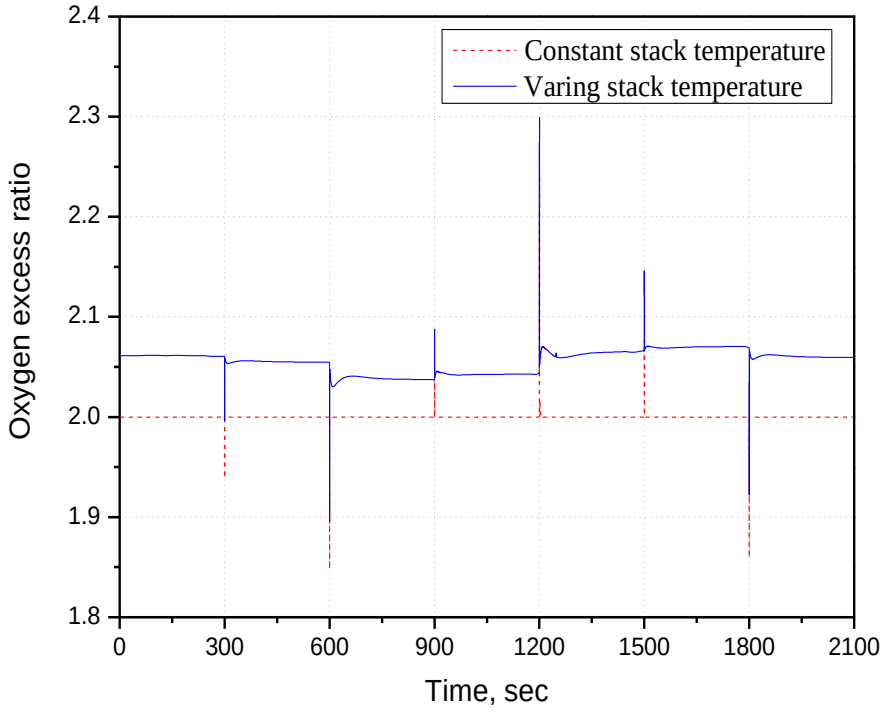

Figure 4-11. Comparison of oxygen excess ratio at constant and varying temperatures.

4.4.4. Response of temperatures with a step current profile

When a multi-step current was applied to the stack, the temperature in the stack rapidly increased, particularly in the catalyst on the cathode side. The catalyst temperature (the dotted red line in Figure 4-12) increased 3 to 7 K higher than the average temperature in the stack,

where the coolant temperature was fully controlled for the reference temperature of 349 K (see the dotted blue line in Figure 4-12). We note that the catalyst and membrane layers could be overheated and might be damaged. Therefore, a reduced-order observer was used to estimate the catalyst temperature, which was set as the reference for the control system. As a result, the control with the reduced-order observer maintained the catalyst temperature at 353 K, and was capable of quickly responding to a change in the current and rejecting the excess heat in the catalyst layer effectively.

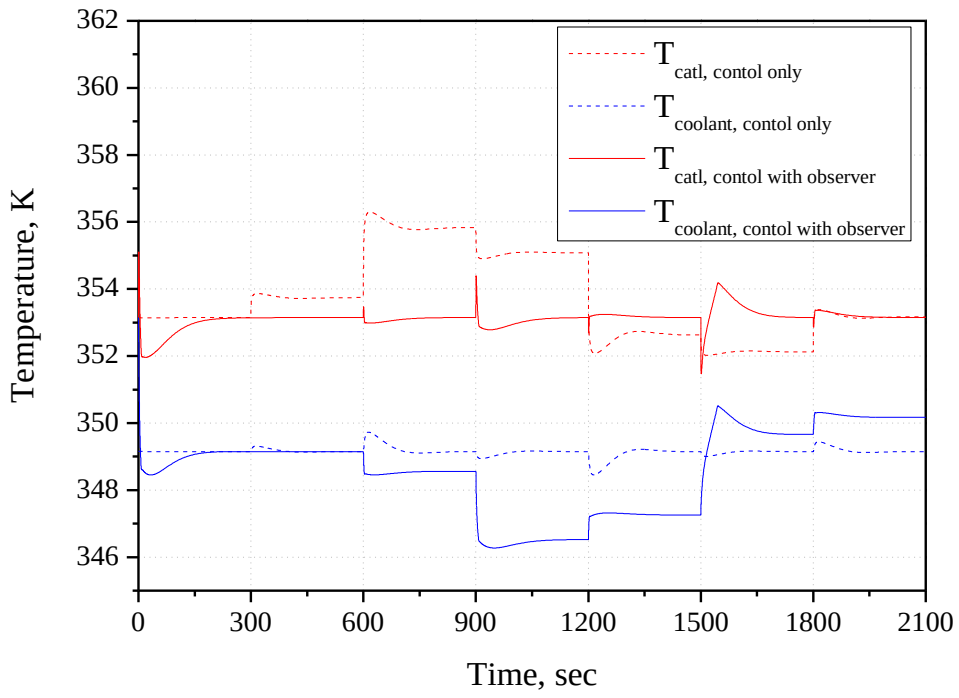

Figure 4-12. Comparison of temperatures of the catalyst layer and coolant channel.

4.4.5. Response of the accumulated total parasitic power with a step current profile

Figure 4-13 shows simulation results for the responses of accumulated total parasitic power for bang-bang and state feedback controls with a step current profile. In a thermal circuit, the blower and the fan consume the power to run. While the fan provides the constant air flow to the radiator, the blower supplies the varying coolant according to the load current. Therefore the difference of the accumulated total parasitic power between bang-bang and state feedback controls depends on the parasitic power of the blower. Since the blower controlled by the state feedback controller operates more accurately than bang-bang controller, the total parasitic power for the state feedback controls during 2100 sec is 8% less than that for the bang-bang control.

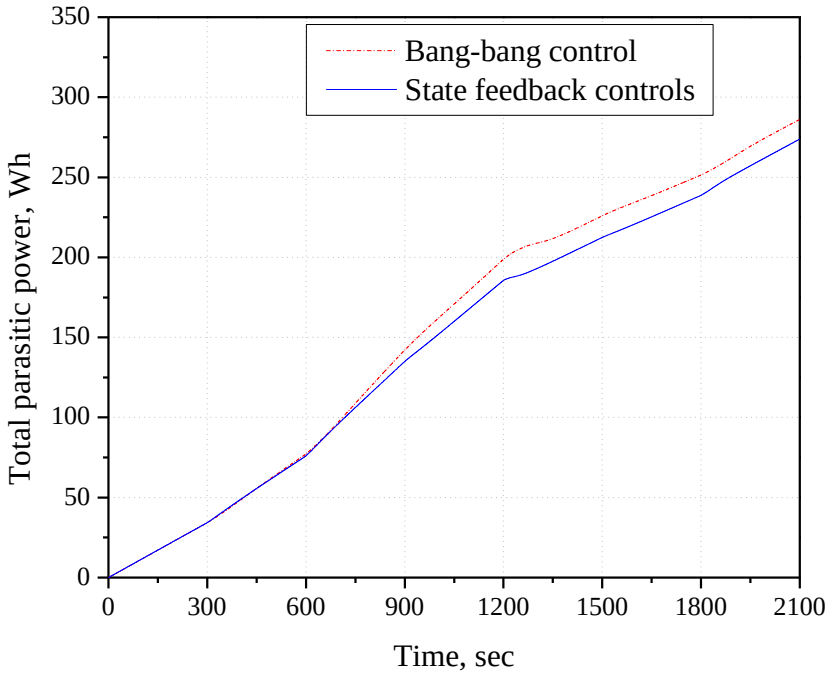

Figure 4-13. Comparison of accumulated total parasitic power between bang-bang and state feedback controller.

4.4.6. Responses of controllers and temperatures for the coolant leak

When a coolant leaks, the coolant pump cannot provide the sufficient coolant to the heat exchanger at the given load current. Thus, the bypass valve is gradually opened to decrease the temperature of the coolant supplied to the heat exchanger as shown in Figure 4-14 (b). The controller regulates the coolant temperature by 240 sec, and then it breaks down as shown in Figure 4-14 (c), which results in rapid increase of the temperature inside a cell and permanent damage of the cell.

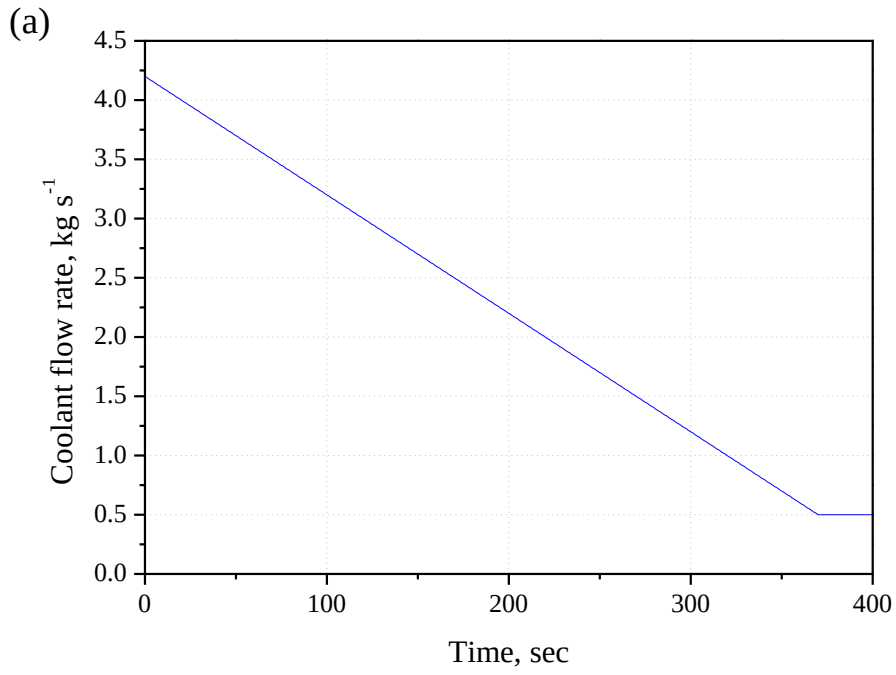

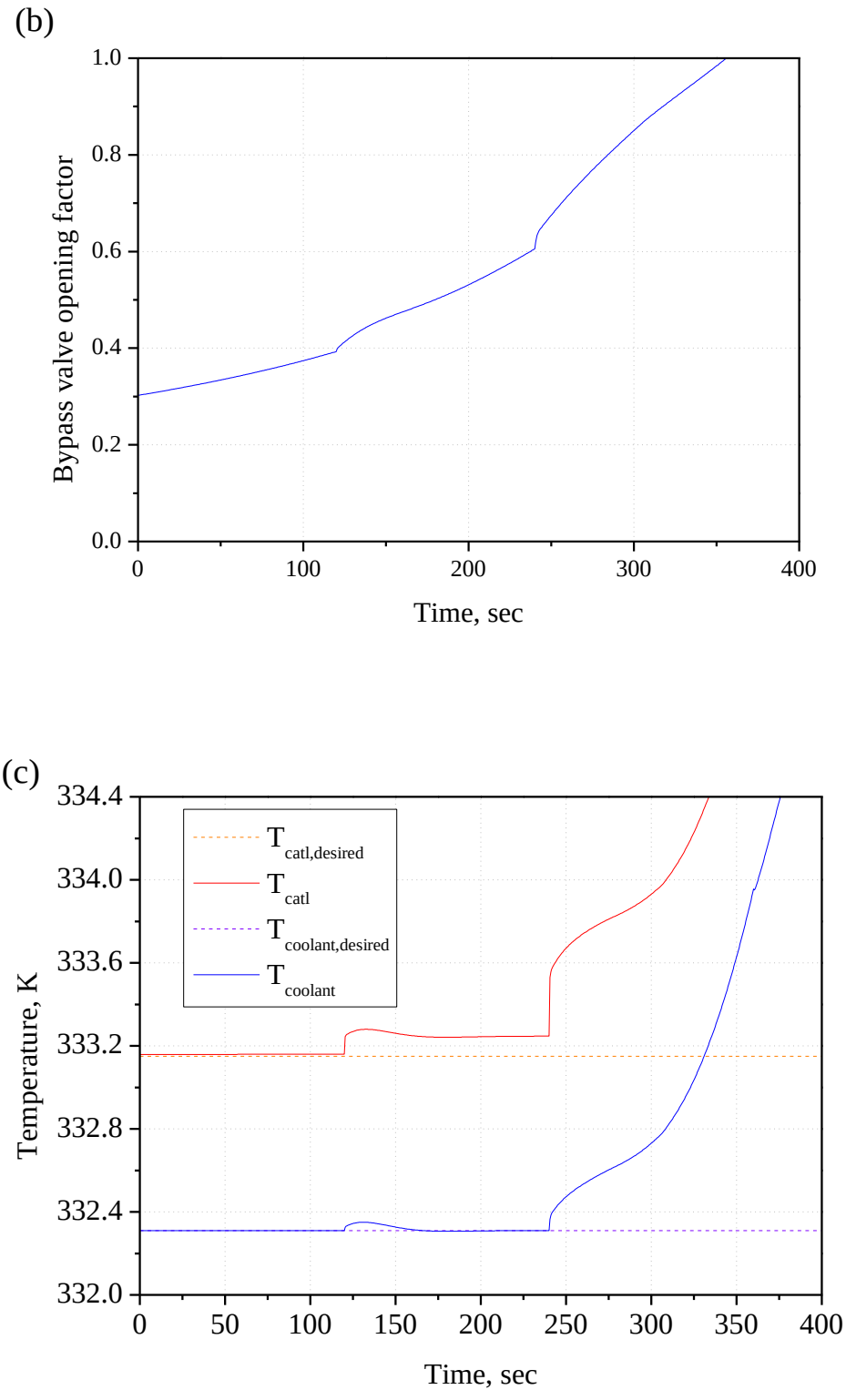

Figure 4-14. (a) Coolant flow rate, (b) bypass valve opening factor, and (c) temperatures of the catalyst layer and coolant channel for the coolant leak.

4.4.7. Responses of temperatures with FUDS

Figure 4-15 shows simulation results for the responses of state feedback control using the reduced-order observer and a current profile experimentally obtained from a vehicle tested at Federal Urban Driving Schedule (FUDS). The peak temperature in the catalyst layer was 6 K higher than the working temperature using the control system without the observer, even though the coolants were fairly well controlled around the set reference temperature as shown in Figure 4-15(b). Figure 4-15(c) shows the temperature of the catalyst and coolants with control using the observer. The peak temperature of the control system with the observer was similar to that of the control system without the observer for the first 200 sec, but was substantially suppressed in the following intervals compared to that of the control system without the observer as shown in Figure 4-15(b). The excursion duration of the catalyst temperature decreased, and finally the heat energy imposed to the thin layers could be reduced. This significantly reduced the heat stress on the layers. Correspondingly, the oxygen excess ratio becomes higher than the desired value of 2.0 shown in Figure 4-15(d).

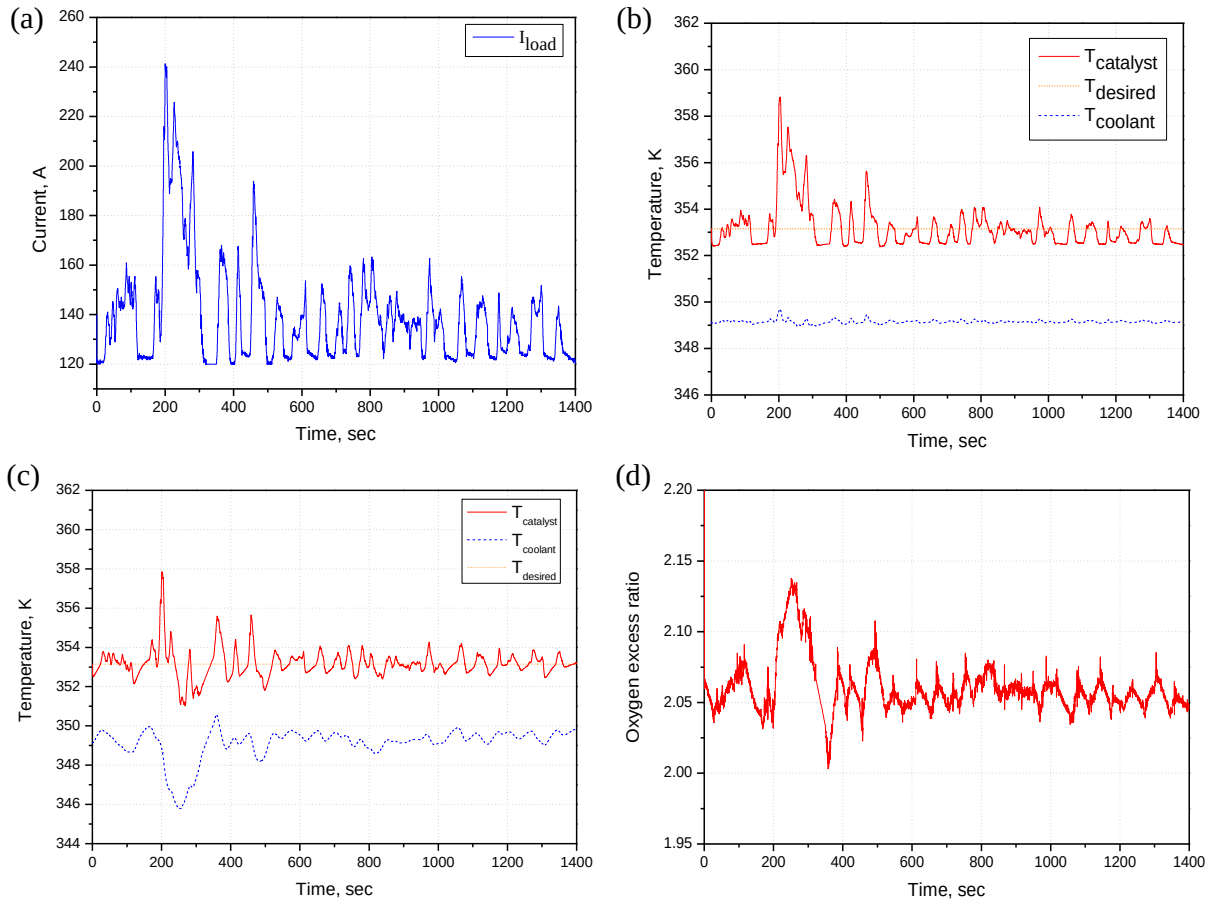

Figure 4-15. (a) FUDS and a current profile with a base load of 120 A, (b) temperature of the catalysts and coolants for control only, (c) temperature of the catalysts and coolants for control with the reduced-order observer, and (d) the oxygen excess ratio.

4.5. Summary

In this chapter, new configuration with two thermal circuits to increase the cooling effectiveness was proposed. For the proposed thermal system, a state feedback controller optimized using LQR method regulated the stack temperature at the desired level and reduced the parasitic power of the system. In fact, the temperature of the catalyst where the chemical reactions occur is 3-7 K higher than the stack temperature. To maintain the catalyst temperature at 80 ℃, the reduced-order observer was developed to estimate the catalyst temperature that was

used to feed-forward to reset the reference temperatures. The results calculated in the FUDS showed that the use of a state feedback controller based on a reduced-order observer improved the controllability of the stack temperature, and that the peak of the catalyst temperature could be dynamically suppressed during a varying load.

Chapter 5 Conclusion

In this study, dynamic models of PEM fuel cell components were developed and integrated with the fuel cell stack model. The integrated system model was used to help determine control strategies and to aid in the design of optimal controllers based on an observer that estimates inaccessible variables.

For air and water management, a bypass valve was added to control the membrane water content by adjusting the exhaust gas flow rate entering the humidifier. The developed feedback controllers for AWM were shown to have successfully maintained the oxygen excess ratio and membrane water content at the desired level. As a result, the net power of the stack increased due to high chemical reaction rate and low ohmic over-potential.

For thermal management, the proposed configuration reduced the size of the weight of the overall system. Moreover, cooling effectiveness was increased using the proposed thermal circuits with a state feedback controller based on input from a reduced-order observer. The designed reduced-order observer was able to follow the estimate state of the catalyst temperature that was used as input to the feed-forward block. The results calculated in the FUDS showed that the use of a reduced-order observer improved the controllability of the stack temperature, and that the peak of the catalyst temperature can be dynamically suppressed and the duration of the above desired catalyst temperature can be reduced during a varying load. Moreover, the efficiency of the total system was increased by reducing parasitic power.

Experiments were performed to characterize the static and dynamic behavior of the humidifier installed in the fuel cell station. The results show that the relative humidity of the air flow exiting the tube side of the humidifier could be controlled by the wet air flow rate entering the shell side. Furthermore, the temperature of the air flow at the outlet of the tube side was increased though the humidifier, which means that there is no need for an additional heater to heat the air flow entering the fuel cell stack. After the humidifier experiment, a fuel cell test station was modified to verify the performance of the proposed configuration, including the humidifier and the bypass valve. The experiments were performed for constant dry air and exhaust gas flow rates entering the humidifier. The stack voltages measured at different valve opening factor under the constant dry air flow were compared, and we confirmed that the proposed control strategy was very effective in improving the degradation of stack power output caused by membrane dehydration and/or water flooding.

In future work, the proposed fuel cell station will be optimized and, in particular, the thermal circuit will be modified to improve cooling effectiveness and reduce the parasitic power of the coolant pump. Additional work involving the AWM and the thermal management system will include development of an integrated control system that accounts for interaction between the reactant gas flow, water, and temperature, and the optimization of controllers using advanced control algorithms.

References

[1] U.S. Energy Information Administration, *Annual Energy Review 2009*, Tables 1.3, 2.1b-2.1f, 10.3, and 10.4, August 19, 2010.

[2] J. Larminie and A. Dicks, *Fuel Cell Systems Explained*, Second Ed., John Wiley & Sons Ltd., Chichester, 2003.

[3] R. Helmolt and U. Eberle, "Fuel cell vehicles: Status 2007," *J. Power Sources*, vol. 165, pp. 833-843, 2007.

[4] M. Granovskii, I. Dincer, and M. A. Roesn, 2006, "Economic and environmental comparison of conventional, hybrid, electric and hydrogen fuel cell vehicles," *J. Power Sources*, vol. 159, pp. 1186-1193, 2006.

[5] U.S. Department of Energy, *The Department of Energy Hydrogen and Fuel Cells Program Plan – Draft*, p. 27, 2010.

[6] A. Su, F.B. Weng, C.Y. Hsu, and Y.M. Chen, "Studies on flooding in PEM fuel cell cathode channels," *Int. J. Hydrogen Energy*, vol. 31, pp. 1031-1039, 2006.

[7] N. Yousfi-Steiner, Ph. Mocoteguy, D. Candusso, and D. Hissel, "A review on polymer electrolyte membrane fuel cell catalyst degradation and starvation issues: Causes, consequences and diagnostic for mitigation," *J. Power Sources*, vol. 194, pp. 130-145, 2009.

[8] A. Taniguchi, T. Akita, K. Yasuda, and T. Miyazaki, "Analysis of degradation in PEMFC caused by cell reversal during air starvation," *Int. J. Hydrogen Energy*, vol. 33, pp. 2323-2329, 2008.

[9] D. Liang, Q. Shen, M. Hou, Z. Shao, and B. Yi, "Study of the cell reversal process of large area proton exchange membrane fuel cells under fuel starvation," *J. Power Sources*, vol. 194, pp. 847-853, 2009.

[10] P. Rodatz, G. Paganelli, and L. Guzella, "Optimization Air supply Control of a PEM Fuel Cell System," *Proc. of IEEE 2003 Amemrican Control Conference*, Denver, CO, 2003.

[11] J.T. Pukrushpan, A.G. Stefanopoulou, and H. Peng, "Modeling and Control for PEM Fuel Cell Stack System," *Proc. of IEEE 2002 American Control Conference*, Anchorage, AK, 2002.

[12] A. Vahidi, A.G. Stefanopoulou, and H. Peng, "Model Predictive Control for Starvation Prevention in a Hybrid Fuel Cell System," *Proc. of IEEE 2004 American Control Conference*, Boston, MA, 2004

[13] J. Zhang, G. Liu, W. Yu, and M. Ouyang, "Adaptive control of the airflow of a PEM fuel cell system," *J. Power Sources*, vol. 179, pp. 649-659, 2008.

[14] J. Ihonen, M. Mikkola, and G. Lindbergh, "Flooding of gas diffusion backing in PEFCs," *J. Electrochem. Soc.*, vol. 151, pp. A1152-A1161, 2004.

[15] H. Li, Y. Tang, Z. Wang, Z. Shi, S. Wu, D. Song, J. Zhang, K. Faith, J. Zhang, H. Wang, Z. Liu, R. Abouatallah, and A. Mazza, "A review of water flooding issues in the proton exchange membrane fuel cell," *J. Power Sources*, vol. 178, pp. 103-117, 2008.

[16] J. St-Pierre, D.P. Wilkinson, S. Knights, and M. Bos, "Relationships between water management, contamination and lifetime degradation in PEFC," *J. New Mat. Electrochem. Systems*, vol. 3, pp. 99-106, 2000.

[17] M. Eikerling and A.A. Kornyshev, "Modeling the performance of the cathode catalyst layer of polymer electrolyte fuel cells," *J. Electroanal. Chem.*, vol. 453, pp. 89-106, 1998.

[18] A. Hakenjos, H. Muenter, U. Wittstadt, and C. Hebling, "A PEM fuel cell for combined measurement of current and temperature distribution, and flow field flooding," *J. Power Sources,* vol. 131, pp. 213-216, 2004.

[19] T.V. Nguyen, "A gas distributor design for proton-exchange-membrane fuel cells," *J. Electrochem. Soc.*, vol. 143, pp. L103-L105, 1996.

[20] T.V. Nguyen, "Water management by material design and engineering for PEM fuel cells," *ECS Trans.*, vol. 3, pp. 1165–1171, 2006.

[21] X. Li, I. Sabir, and J. Park, "A flow channel design procedure for PEM fuel cells with effective water removal," *J. Power Sources,* vol. 163, pp. 933-942, 2007.

[22] L. Wang, A. Husar, T. Zhou, and H. Liu, "A parametric study of PEM fuel cell performances," *Int. J. Hydrogen Energy,* vol. 28, pp. 1263-1272, 2003.

[23] S. Ge, X. Li, and I.M. Hsing "Internally humidified polymer electrolyte fuel cells using water absorbing sponge," *Electrochimica Acta,* vol. 50, pp. 1909-1916, 2005.

[24] D. Spernjak, A.K. Prasad, and S.G. Advani, "Experimental investigation of liquid water formation and transport in a transparent single-serpentine PEM fuel cell," *J. Power Sources,* vol. 170, pp. 334-344, 2007.

[25] Z. Qi and A. Kaufman, "Improvement of water management by a microporous sublayer for PEM fuel cells," *J. Power Sources,* vol. 109, pp. 38-46, 2002.

[26] T.J.P. Freire and E.R. Gonzalez, "Effect of membrane characteristics and humidification conditions on the impedance response of polymer electrolyte fuel cells," *J. Electroanal. Chem.*, vol. 503, pp. 57-68, 2001.

[27] F.N. Buchi and S. Srinivasan, "Operating proton exchange membrane fuel cells without external humidification of the reactant gases," *J. Electrochem. Soc.*, vol. 144, pp. 2767-2772, 1997.

[28] D.P. Wilkinson, H.H. Voss, and K. Prater, "Water management and stack design for solid polymer fuel cells," *J. Power Sources*, vol. 49, pp. 117-127, 1994.

[29] A. Mughal and X. Li, "Experimental diagnostics of PEM fuel cells," *Int. J. Environ. Stud.*, vol. 63, pp. 377-389, 2006.

[30] C.R. Buie, J.D. Posner, T. Fabian, S.W. Cha, D.J. Kim, F.B. Prinz, J.K. Eaton, and J.G. Santiago, "Water management in proton exchange membrane fuel cells using integrated electro-osmotic pumping," *J. Power Sources*, vol. 161, pp. 191-202, 2006.

[31] S.G. Goebel, "Evaporative Cooled Fuel Cell," U.S. Patent no. 6960404, 2005.

[32] C.Y. Wang, "Fundamental models for fuel cell engineering," *Chem. Rev.*, vol. 104, pp. 4727-4766, 2004.

[33] M. Lampinen and M. Fomino, "Analysis of free energy and entropy changes for half-cell reactions," *J. Electrochem. Soc.*, vol. 140, pp. 3537-3546, 1997.

[34] W. Bi and T.F. Fuller, "Temperature effects on PEM fuel cells Pt/C catalyst degradation," *J. Electrochem. Soc.*, vol. 155, pp. B215-B221, 2008.

[35] G. Maggio, V. Recupero, and C. Mantegazza, "Modeling of temperature distribution in a solid polymer electrolyte fuel cell stack," *J. Power Sources*, vol. 62, pp. 167-174, 1996.

[36] P. Hu, G.Y. Cao, X.J. Zhu, and M. Hu, "Coolant circuit modeling and temperature fuzzy control of proton exchange membrane fuel cells," *Int. J. Hydrogen Energy*, vol. 35, pp. 9110-9123, 2010.

[37] C.Y. Wen, Y.S. Lin, C.H. Lu, and T.W. Luo, "Thermal management of a proton exchange membrane fuel cell stack with pyrolytic graphite sheets and fans combined," *Int. J. Hydrogen Energy*, vol. 36, pp. 6082-6089, 2011.

[38] S. Yu and D. Jung, "Thermal management strategy for a proton exchange membrane fuel cell system with a large active cell area," *Renewable Energy*, vol. 33, pp. 2540-2548, 2008.

[39] J.C. Amphlett, R.M. Baumert, R.F. Mann, B.A. Peppley, and P.R. Roberge, "Performance modeling of the Ballard Mark IV solid polymer electrolyte fuel cell," *J. Electrochem. Soc.*, vol. 142, pp. 9-15, 1995.

[40] J.T. Pukrushpan, H. Peng, and A.G. Stefanopoulou, "Simulation and Analysis of Transient Fuel Cell System Performance based on a Dynamic Reactant Flow Model," *Proc. of IMEXE'01, 2002 ASME International Mechanical Engineering Congress & Exposition*, New Orleans, LA, 2002.

[41] M. Khandelwal, S.H. Lee, and M.M. Mench, "One-dimensional thermal model of cold-start in a polymer electrolyte fuel cell stack," *J. Power Sources*, vol. 172, pp. 816–830, 2007.

[42] Y. Shan and S.Y. Choe, "A high dynamic PEM fuel cell model w*ith the tempera*ture Effects," *J. Power Sources*, vol. 145, pp. 30-39, 2005.

[43] D.A. McKay, W.T. Ott, and A.G. Stefanopoulou, "Modeling, Parameter Identification, and Validation of Reactant and Water Dynamics for a Fuel Cell Stack," *Proc. of IMECE'05, 2005 ASME International Mechanical Engineering Congress & Exposition*, Orlando, FL, 2005.

[44] T.E. Springer, T.A. Zawodzinski, and S. Gottesfeld, "Polymer electrolyte fuel cell model," *J. Electrochem. Soc.*, vol. 138, pp. 2334-2342, 1991.

[45] T.V. Nguyen and R.E. White, "A water and heat management model for proton-exchange-membrane fuel cells," *J. Electrochem. Soc.*, vol. 140, pp. 2178-2186, 1993.

[46] L. Guzzella, "Control Oriented Modeling of Fuel-Cell Based Vehicles," *presented in NSF Workshop on the Integration of Modeling and Control for Automotive Systems*, 1999.

[47] S.K. Park and S.Y. Choe, "Dynamic modeling and analysis of a 20-cell PEM fuel cell stack considering temperature and two-phase effects," *J. Power Sources*, vol. 179, pp. 660-672, 2008.

[48] S. Gurski, "Cold Start Effects on Performance and Efficiency for Vehicle Fuel Cell System," *Master of Science Thesis*, Mechanical Engineering, Virginia Polytechnic Institute and State University, Dec. 19, 2002

[49] M. Wöhr, K. Bolvin, W. Schnurnberger, M. Fischer, W. Neubrand, and G. Eigenberger, "Dynamic modeling and simulation of a polymer membrane fuel cell including mass transport limitation," *Int. J. Hydrogen Energy*, vol. 23, pp. 213-218, 1998.

[50] J.H. Nam and M. Kaviany, "Effective diffusivity and water-saturation distribution in single- and two-layer PEMFC diffusion medium," *Int. Heat Mass Transfer*, vol. 46, pp. 3595-4611, 2003.

[51] D.A. McKay, A.G. Stefanopoulou, and J. Cook, "A Membrane-type Humidifier for Fuel Cell Application: Controller Design, Analysis and Implementation," *Proc. of FuelCell2008, Sixth International Fuel Cell Science, Engineering and Technology Conference*, Denver, CO, 2008.

[52] J.M. Cunningham, M.A. Hoffman, and D.J. Friedman, "A comparison of high-pressure and low-pressure operation of PEM fuel cell systems," SAE paper No. 2001–01–0538.

[53] Phoenix Design & Technologies, The PDAT Turbomix. http://www.padtinc.com/sales/fuelcell/turbomix/, March 2009.

[54] R.T. Meyer and B. Yao, "Modeling and Simulation of a Modern PEM Fuel Cell System," *Proc. of FuelCell2006, 4th International Conference on Fuel Cell Science, Engineering and Technology,* Irvine, CA, 2006.

[55] J.P. Evans, "Experimental Evaluation of the Effects of Inlet Gas Humidification on Fuel Cell Performance," *Master of Science Thesis*, Mechanical Engineering, Virginia Polytechnic and State University, Sep. 17, 2003.

[56] E.J. Carlson, J.S. Kopf, S. Sriramulu, and Y. Yang, "Cost Analysis of PEM Fuel Cell Systems for Transportation," Subcontract Report, NREL/SR-560-39104, Cambridge, MA, Sep. 30, 2005.

[57] D. Chen and H. Peng, "A thermodynamic model of membrane humidifiers for PEM fuel cell humidification control," *Transactions of the ASME*, vol. 127, pp. 424-432, 2005.

[58] A. Dunlavy, "Dynamic Modeling of Two-phase Heat and Vapor Transfer Characteristics in a Gas-to-gas Membrane Humidifier for Use in Automotive PEM Fuel Cells," *Master of Science Thesis*, Mechanical Engineering, Auburn University, Dec. 18, 2009.

[59] Perma Pure LLC. http://www.permapure.com/.

[60] D.G. Kroger, "Radiator characterization and optimization," SAE paper 840380.

[61] J.W. Ahn and S.Y. Choe, "Coolant controls of a PEM fuel cell system," *J. Power Sources*, vol. 179, pp. 252-264, 2008.

Appendix A Matrices for air supply system

$$A=\begin{bmatrix} -1262 & 0 & -1095 & 0 & 8374 & 0 & 0 & 2405 \\ 0 & -16.9 & 0 & 0 & 5164 & 0 & -1812 & 0 \\ -375.7 & 0 & -4631 & 0 & 275.7 & 0 & 0 & 153.3 \\ 0 & 0 & 0 & -17.35 & 20.32 & 0 & 0 & 0 \\ 2.598 & 0 & 2.968 & 0.3973 & -3.87 & 0.1066 & 0 & 0 \\ 332.8 & 0 & 380.3 & 5.06222 & -479.4 & 0 & 0 & 0 \\ 0 & -44.95 & 0 & 0 & 142.1 & 0 & -80.83 & 0 \\ 4.045 & 0 & 4.621 & 0 & 0 & 0 & 0 & -512.2 \end{bmatrix},$$

$$B_u^T=\begin{bmatrix} 0 & 0 & 0 & 3.947 & 0 & 0 & 0 & 0 \end{bmatrix},$$

$$B_w^T=\begin{bmatrix} -0.03159 & -0.00398 & 0 & 0 & 0 & 0 & -0.05244 & 0 \end{bmatrix},$$

$$C_z=\begin{bmatrix} 4.94 & 2.091 & -1.089 & 0.1966 & 0 & 0 & 0 & 0 \\ -1.280 & 0 & -1.462 & 0 & 13.96 & 0 & 0 & 0 \end{bmatrix},$$

$$D_{zu}=\begin{bmatrix} -0.169 \\ 0 \end{bmatrix},$$

$$D_{zw}=\begin{bmatrix} 0.1802 \\ -0.01055 \end{bmatrix}$$

Appendix B Linear Quadratic Regulator method

A linear quadratic regulator (LQR) is used for the optimization of control gains by summing the squares of the errors. The gains become optimal if the cost function of the LQR, *J*, obtains a minimum value. Thus,

$$J = \int_0^\infty (\delta z_2^T Q_z \delta z_2 + q^T Q_I q + \delta u^T R \delta u) dt \tag{B-1}$$

where Q_z and Q_I represent weighting matrices amplifying the errors of the control objects, and weighting matrix R is used to suppress the effect of the manipulating variable.

The variable δz_2 includes the disturbance δw (Eq. (3-11)), and consequently in the cost function. If the disturbance term in Eq. (3-11) is set to zero, the variable δz_2 yields a new variable with $\delta z_2^{'} = C_{z_2} \delta x$ that is reflected in cost function *J*:

$$J = \int_0^\infty (\delta x^T C_{z_2}^T Q_z C_{z_2} \delta x + q^T Q_I q + \delta u^T R \delta u) dt \tag{B-2}$$

Consequently, the cost function includes a control input as well as the objects. If the control input is substituted by the function of a controller, the cost function will include control objects that facilitate a determination of both weighting matrices that are only dependent on the control objects. Eq. (B-3) describes the control input as a function of the control objects:

$$\delta u = -K \begin{bmatrix} \delta \tilde{x} & q \end{bmatrix}^T = -K_p \delta \tilde{x} - K_I q \tag{B-3}$$

where $\delta \tilde{x} = \delta x_{desired} - \delta x$ and K represents the gain for the proportional and integral controller. $\delta x_{desired}$ is the reference value of the state variables and is obtained at $\delta z / \delta w = 0$.

According to optimal control theory, the variation of the cost function at a fixed end time is given as

$$\bar{J} = \int_0^\infty (\delta x^T C_{z_2}^T Q_z C_{z_2} \delta x + q^T Q_I q + \delta u^T R \delta u + \lambda^T (f(\delta x, \delta u, \delta w) - \delta \dot{x}))dt \quad \text{(B-4)}$$

where λ is defined as a co-state vector that can be an arbitrary value set because the variation of the cost function vanishes along an optimal trajectory. The last term in Eq. (B-4), $-\int_0^\infty \lambda^T \delta \dot{x} dt$, can be resolved into three parts. The first and the second terms are zeros because of the initial and terminal conditions that are assumed to be fixed:

$$-\int_0^\infty \lambda^T \delta \dot{x} dt = -\lambda^T \delta x(\infty) + \lambda^T \delta x(0) + \int_0^\infty \dot{\lambda}^T \delta x \delta t \quad \text{(B-5)}$$

Finally, Eq. (B-5) is resolved into three parts: the state, output, and control input variables. Thus,

$$\delta \bar{J} = \int_0^\infty (\delta x^T C_{z_2}^T Q_z C_{z_2} + \lambda^T f_x + \dot{\lambda}^T)\delta x + (q^T Q_I + \lambda^T f_w)q + (\delta u^T R + \lambda^T f_u)\delta u)dt \quad \text{(B-6)}$$

where $f_x = -\int_0^\infty \lambda^T \delta \dot{x} dt = -\lambda^T \delta x(\infty) + \lambda^T \delta x(0) + \int_0^\infty \dot{\lambda}^T \delta x \delta t = A$, $f_u = B_u$, and $f_w = B_w$.

If the cost function is minimized, each of the three terms in the variation of the cost function (Eq. B-6) should be zeros. Thus,

$$\dot{\lambda} = -C_{z_2} Q_z C_{z_2}^T \delta x - A^T \lambda \quad \text{(B-7)}$$

$$Q_I \delta w + B_w^T \lambda = 0 \quad \text{(B-8)}$$

$$R\delta u + B_u^T \lambda = 0 \quad \text{(B-9)}$$

If $\lambda = P\delta x$, then Eqs. B-7, B-8, and B-9 can be expanded using Eq. 3-11, which results in the following equations:

$$PA + A^T P + C_{z_2} Q_z C_{z_2} - PB_u R^{-1} B_u^T P - PB_w Q_I^{-1} B_w^T P = 0 \quad \text{(B-10)}$$

Finally, an algebraic Riccati equation (Eq. (B-10)) is obtained. Its solution P can be solved by the MATLAB function "lqr". As a result, the gain for the PI controller is obtained from Eqs. B-8 and B-9 with P:

$$\delta u = -R^{-1} B_u^T P \delta x - Q_I^{-1} B_w^T P q = -K_p \delta \tilde{x} - K_I q \quad \text{(B-11)}$$

Appendix C Matrices for thermal management

$$A = \begin{bmatrix} -0.0245 & 0.0245 \\ 0.0373 & -0.0477 \end{bmatrix},$$

$$B_u = \begin{bmatrix} -0.3179 & 0 \\ 0.0089 & -2.4756 \end{bmatrix},$$

$$B_w = \begin{bmatrix} 6.34 \times 10^{-6} \\ 0 \end{bmatrix},$$

$$C = \begin{bmatrix} 1 & 0 \\ 0 & 1 \end{bmatrix}$$